A CFD STUDY OF POLLUTION DISPERSION IN STREET CANYON AND EFFECTS OF LEAF HAIR ON PM2.5 DEPOSITION

Jedhathai Boontanom

Thesis submitted to the faculty of the Virginia Polytechnic Institute and
State University in partial fulfillment of the requirements for the degree of

Master of Science
In
Mechanical Engineering

Danesh K. Tafti, Chair
Mark R. Paul
Linsey C. Marr

May 14, 2019
Blacksburg, Virginia

Keywords: Computational Fluid Dynamics (CFD), Large-Eddy Simulation (LES),
Dry Deposition, Air Quality, Leaf Hair, Trichome

A CFD STUDY OF POLLUTION DISPERSION IN STREET CANYON AND EFFECTS OF LEAF HAIR ON PM2.5 DEPOSITION

Jedhathai Boontanom

ABSTRACT

According to the United Nations, 55% of the world's population currently lives in urban areas and which is projected to increase to 67% by 2050. Thus, it is imperative that effective strategies are developed to mitigate urban pollution. Complementing field experiments, computational fluid dynamics (CFD) analyses are becoming an effective strategy for identifying critical factors that influence urban pollution and its mitigation. This thesis focuses on two scales of the urban micro-climate environment: (i) evaluation of LES simulations with a simplified grid for modeling pollution dispersion in a street canyon and (ii) investigation of the effects of leaf surface micro-characteristics, wind speed, and particle sizes on the dry deposition of fine particulate matter (PM2.5).

The first of these studies focuses on reproducing the pollution dispersion in a street canyon measured in a wind tunnel at Karlsruhe Institute of Technology (KIT), Germany. A simplified grid with the Large Eddy Simulations (LES) approach for canyon ratio W/H = 1 is proposed with the goal to reduce the computational cost by eliminating the need to model the entire canyon while striving to preserve the mixing induced by individual jets used to model vehicle emission in the experiment. LES is also capable of providing transient flow field and pollution concentration data not available with widely-used steady approaches such as RANS. The time-dependent information is crucial for pollution mitigation since pedestrians are usually exposed to pollution on a short-time basis.

The predictions are in satisfactory agreement with the experiment for W/H = 1, yielding the Pearson correlation coefficient R = 0.81, with better performance near the leeward wall. Due to the small span modeled, three-dimensional instabilities fail to develop which could probably explain the overprediction of pollution concentration near ground level. However, other LES investigations where the full canyon was modeled also observed over-predictions. The use of a discrete emission source was not observed to provide benefits. The current model could be further improved by using a larger spanwise domain with a continuous line source to allow large wavelength instabilities to develop and increase turbulent diffusion.

The second part of this thesis investigates the impact of trichome morphology and wind speed on the deposition of 0.3 μm and 1.0 μm particles on leaves. Using the one-way coupling approach to predict the fluid-particle interactions with the assumption that all particles that impact the leaf or trichome surface deposit, trichomes of 5 μm and 20 μm in diameter are modeled as equally spaced and uniform cylinders on an infinitely large plane.

The results show that trichome diameter, density, and wind speed have a favorable impact on deposition velocity. Comparing to the smooth leaf, the presence of the thicker 20 μm hairs increases the deposition velocity by 1.5 – 4 times, whereas, the presence of short 5 μm trichomes reduces the deposition by 15 - 45%. Increasing trichome height from H/D = 20 to 30 shows benefits for the thinner trichomes but lowers the deposition for the densely packed thicker trichomes. Less aerosol deposition is also observed when the particle diameter increases from 0.3 μm to 1.0 μm.

Due to the non-uniform contributions of these various traits, a non-dimensional ratio $R_{hp} = \frac{D^*_{hair}}{D^*_p}\frac{(D^*_{hair})^2}{H^*_{hair}S^*_{hair}}$ is proposed to model the aerosol deposition on leaf surface at wind speed of 1 m/s which yields a satisfactory linear correlation coefficient of 0.89 for $0 < R_{hp} < 0.3$.

Comparing to other published field and wind tunnel experiments conducted on a much larger scale, the deposition velocities predicted are at the lower end (U^*_{dep} = 0.002 to 0.012 cm/s) because of the idealized conditions. Nonetheless, the results still offer valuable insight into the effects of trichome morphology on pollutant deposition in isolation from other macro-factors.

A CFD STUDY OF POLLUTION DISPERSION IN STREET CANYON AND EFFECTS OF LEAF HAIR ON PM2.5 DEPOSITION

Jedhathai Boontanom

GENERAL AUDIENCE ABSTRACT

According to the United Nations, 55% of the world's population currently lives in urban areas and which is projected to increase to 67% by 2050. Thus, it is imperative that effective strategies are developed to mitigate urban pollution. Complementing field experiments, computational fluid dynamics (CFD) analyses are becoming an effective strategy for identifying critical factors that influence urban pollution and its mitigation. This thesis focuses on two scales of the urban micro-climate environment: (i) evaluation of Large Eddy Simulation (LES) with a simplified method for modeling pollution dispersion in a street canyon and (ii) investigation of the effects of leaf surface micro-characteristics, wind speed, and particle sizes on the dry deposition of fine particulate matter (PM2.5).

The first of these studies focuses on reproducing the pollution dispersion in a street canyon measured in a wind tunnel at Karlsruhe Institute of Technology (KIT), Germany. A simplified grid with the LES approach for canyon ratio W/H = 1 is proposed. The goal of this study is to reduce the computational cost by modelling the canyon with a very thin span instead of the entire canyon while providing time-dependent information which is crucial for pollution mitigation since pedestrians are usually exposed to pollution on a short-time basis.

The predictions are in satisfactory agreement with the experiment for W/H = 1 with better performance near the leeward wall (i.e. the left wall) and overprediction of pollution concentration near ground level – as observed by other LES investigations. The current model

could be further improved by using a larger spanwise domain with a continuous line source to allow instabilities to develop, thus improve prediction accuracy.

The second part of this thesis investigates the impact of trichome (i.e. a hair or an outgrowth from leaf surface) morphology and wind speed on the deposition of 0.3 μm and 1.0 μm particles on leaves. The results show that trichome diameter, density, and wind speed have a favorable impact on deposition velocity. Less aerosol deposition is also observed when the particle diameter increases from 0.3 μm to 1.0 μm. No clear effects is observed by altering the trichome height.

Due to the non-uniform contributions of these various traits, a non-dimensional ratio $R_{hp} = \frac{D^*_{hair}}{D^*_p} \frac{(D^*_{hair})^2}{H^*_{hair} S^*_{hair}}$ is proposed to model the aerosol deposition on leaf surface at wind speed of 1 m/s which yields a satisfactory linear correlation coefficient of 0.89 for $0 < R_{hp} < 0.3$. This ratio includes trichome diameter (D^*_{hair}), height (H^*_{hair}), spacing (S^*_{hair}) as well as the ratio of trichome diameter to particle diameter (D^*_{hair}/D^*_p). The results offer valuable insight into the effects of trichome morphology on pollutant deposition in isolation from other macro-factors.

ACKNOWLEDGEMENT

I would like to express my sincere gratitude to my advisor, Dr. Danesh Tafti for his willingness to help and teach me with kindness and patience regardless of how busy he is. He always makes himself available to his students, gives us his full attention and makes his lab feel like a very comfortable place to be at by treating us great food and bringing us some baked goods.

I would also like to thank Dr. Mark Paul and Dr. Lindsey Marr for taking the time from their busy schedules to be my committee and reviewing my work.

I would like to thank all of my lab mates for helping and sharing life with me for the past two years (Susheel, Tae, Maryam, Peter, Aevelina, Vivek, Ze and Muhammed).

I would like to thank my church (Grace Covenant Presbyterian Church), for being a big family of Christ to me and for praying, loving, and caring for me. I also thank my family for giving me the opportunity to come study at Virginia Tech and for supporting me.

Finally, I give my thanksgiving to the Lord my God who has sustained me throughout graduate school and has been kind to me – an undeserving sinner. I boast not in my works but in Him who sent His Son Jesus to die for me. His grace is sufficient, and His power is made perfect in weakness (2 Cor 12:9).

Praised be the Name of the Lord!

TABLE OF CONTENTS

LIST OF FIGURES

LIST OF TABLES

ABBREVIATIONS

CFD	Computational Fluid Dynamics
CODASC	Concentration Data of Street Canyons
GenIDLEST	Generalized Incompressible Direct and Large Eddy Simulation of Turbulence
KIT	Karlsruhe Institute of Technology
LES	Large-eddy Simulation
PM	Particulate Matter
RANS	Reynolds Averaged Navier-Stokes
SF_6	Sulfur Hexafluoride
URANS	Unsteady Reynolds Averaged Navier-Stokes

CHAPTER 1: INTRODUCTION

Hazardous air pollutants are found to pose higher risks in urban areas due to larger populations and higher concentrations of emission sources [1]. This relationship is alarming because 82% of America's population is now living in urban areas in 2018, and 68% of the world's population is predicted to live in urban areas by 2050, indicating the rapid rise of urbanization [2]. Since the passage of the Clean Air Act in 1990, the overall air quality in the United States has improved by 70%. However, pollutants continue to be released into the air [1]. To combat the issue of pollution which rises with urbanization, research on sustainable living has been gaining more attention in recent years [3], and much emphasis has been paid to street vegetation such as trees, green facades and urban parks which are commonly thought of as air filters [4]. In the review on the CFD analysis of urban microclimate by Toparlar, et al. [5], where microclimate studies from 1998 to 2015 were investigated, the growing popularity of this field is indicated by the number of publications in the 2013-2015 period constituting more than half of all the studies (57% of 183 studies).

In order to mitigate the issue, one must understand the nature and behavior of urban air pollution. There are two main categories employed for urban microclimate[1] studies: observational and simulation approaches. Numerical simulations allow researchers to assess different variables and scenarios. As advanced computational resources have become increasingly available, numerical simulation approaches, especially Computational Fluid

---

[1]American Meteorological Society (AMS) (http://glossary.ametsoc.org/) defines the term "microclimate" as "the fine climatic structure of the air space that extends from the very surface of the earth to a height where the effects of the immediate character of the underlying surface no longer can be distinguished from the general local climate."

Dynamics (CFD), have gained popularity in the field of urban microclimate research due to its ability to resolve finer scale flow fields and applications to various spatial scales in climate modeling [5].

Outdoor pollution originates from both natural and anthropogenic sources and comes in form of gas and aerosols, with the most harmful pollutants to public health being particulate matter (PM), ground-level ozone (O_3), Nitrogen Dioxide (NO_2), and Sulfur Dioxide (SO_2) [6]. Thus, through the lens of computational simulations, air pollutants can be generally categorized as gas and particles.

An aerosol is any solid or liquid particle dispersed in the atmosphere. The particulate portion of an aerosol is called particulate matter (PM). In this report, the terms aerosol and particulate matter will be used interchangeably and specifically for solid particles. Anthropogenically generated particulate matters are primarily from fuel combustion, industrial processes, power generation, and transportation sources mainly through direct emissions and gas-to-particle conversion of vapor precursors [7]. Aerosols are categorized into two main groups based on diameter:

(1) Coarse Particles (PM_{10}): particles with diameters of 10 μm or less.

(2) Fine Particles ($PM_{2.5}$): particles with diameters of 2.5 μm or less.

Aerosols of both classes are inhalable. PM_{10} can penetrate inside the lungs, but $PM_{2.5}$ can pose more health-damaging effects since they can penetrate the lung barrier and enter into the blood system, increasing the risk of developing chronic and acute cardiovascular and respiratory diseases such as asthma and lung cancer [8].

In urban areas, the primary sources of particulate emissions are industries and transportation as well as natural sources. The typical size distribution of urban aerosols is shown in Figure 1. The mass, which is proportional to the volume, distribution is dominated by particles with diameters of 0.3 μm and 6 μm, while the number distribution mostly consists of ultrafine particles (<0.1 μm in diameter), typically found close to sources [7]. Particles smaller than 1 μm in diameter are usually found at atmospheric concentrations ranging from ten to several thousand per cm^3. Larger particles normally have concentrations of less than 1 per cm^3 [7]. Due to the higher health risk, the author chose to pay specific attention to fine particles with a diameter ranging from 0.1 to 1 μm.

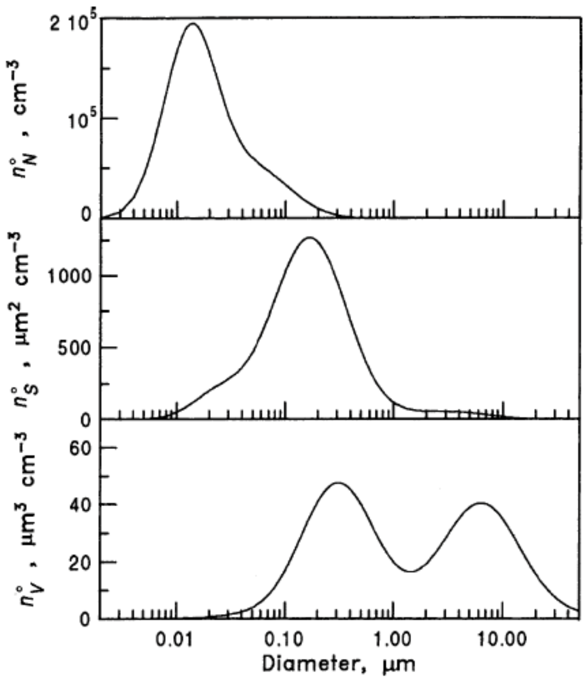

Figure 1 Typical size distributions of urban aerosols based on number, surface area, and volume. [7]

This thesis emphasizes on two scales of microclimate studies:

(1) Evaluation of LES simulations with a simplified grid for microscale climate modeling of pollution dispersion in a street canyon; and

(2) Effects of leaf hair traits, wind speed, and particle sizes on fine aerosol deposition on a leaf surface.

Chapter 1 discusses the motivation and objectives of the research. The general mathematical method used for both focuses is given in Chapter 2. Chapter 3 discusses the state-of-the-art of pollution dispersion modeling in a street canyon and the development and performance evaluation of a simplified street canyon model. Chapter 4 gives a brief overview of leaf hair structure and investigates the effects of hair characteristics as well as particle sizes and wind speed on deposition velocity.

CHAPTER 2: MATHEMATICAL FORMULATION

Calculations are performed using the in-house source code GenIDLEST (Generalized Incompressible Direct and Large Eddy Simulation of Turbulence) [9]. For simulating the street canyon, a Large-eddy Simulation (LES) is performed. To simulate the particle deposition on leaf hairs, a fully-developed laminar flow is used. This chapter discusses the governing equations for the single- and two-phase flows encountered in this study.

2.1 Governing Equations

2.1.1 Mass and Momentum Conservation

The filtered mass and momentum conservation equations are solved in the domain, and the dimensionless form of continuity and momentum equations are expressed as

$$\frac{\partial \rho}{\partial t} + \frac{\partial \rho u_i}{\partial x_i} = 0 \tag{1}$$

$$\begin{aligned} &\frac{\partial}{\partial t}(\rho u_i) + \frac{\partial}{\partial x_j}\left(\rho u_i u_j\right) \\ &\qquad = -\frac{\partial P}{\partial x_i} + \frac{1}{Re_{ref}}\frac{\partial}{\partial x_j}\left[(\mu + \mu_t)\left\{\frac{\partial u_i}{\partial x_j} + \frac{\partial u_j}{\partial x_i}\right\} - \frac{2}{3}\delta_{ij}\frac{\partial u_k}{\partial x_k}\right] + \rho g_i \end{aligned} \tag{2}$$

, where ρ, u_i, P are non-dimensional grid-filtered mixture density, velocity and pressure, and μ and g_i, are the dynamic viscosity and gravity, respectively. The subgrid stress is calculated by using the turbulent viscosity, μ_t, which is obtained from the dynamic Smagorinsky subgrid stress (SGS) model [10], [11], using a local procedure to find the value of the Smagorinsky constant at each grid point. The reference Reynolds number is defined by:

$$\mathrm{Re}_{\mathrm{ref}} = \frac{\rho^*_{\mathrm{ref}} U^*_{\mathrm{ref}} L^*_{\mathrm{ref}}}{\mu^*_{\mathrm{ref}}} \tag{3}$$

where the subscript "ref" indicates reference values input by the user. The dimensional variables, denoted with * are non-dimensionalized with a set of reference values (μ^*_{ref}, ρ^*_{ref}, P^*_{ref}, L^*_{ref}, and U^*_{ref}) as follows

$$\begin{aligned} u_i &= \frac{u_i^*}{U^*_{\mathrm{ref}}} \qquad \mu = \frac{\mu^*}{\mu^*_{\mathrm{ref}}} \qquad P = \frac{P^* - P^*_{\mathrm{ref}}}{\rho^*_{\mathrm{ref}} U^*_{\mathrm{ref}}} \qquad \rho = \frac{\rho^*}{\rho^*_{\mathrm{ref}}} \\ t &= \frac{t^* U^*_{\mathrm{ref}}}{L^*_{\mathrm{ref}}} \qquad x_i = \frac{x_i^*}{L^*_{\mathrm{ref}}} \qquad T = \frac{T^* - T^*_{\mathrm{ref}}}{T^*_{\mathrm{ref}}} \end{aligned} \tag{4}$$

The dimensional dynamic viscosity μ^*_{ref}, density ρ^*_{ref}, and mass diffusion coefficient D^*_{ref} are calculated based on the temperature and species concentration. Isothermal condition is assumed in this study, thus the properties are computed at the reference temperature, $T^*_{\mathrm{ref}} = 300$ K.

For single species or in the case where pollution is modeled as a dispersed phase, μ^*_{ref} is calculated using the Sutherland law at T^*_{ref} [12], while ρ^*_{ref} is calculated using the ideal gas law at T^*_{ref} and P^*_{ref}. For binary mixture where emission is modeled as gas, the reference values are the same as those of the carrier phase which is air in this study (i.e. $\mu^*_{\mathrm{ref}} = \mu^*_{\mathrm{air}}$ and at $\rho^*_{\mathrm{ref}} = \rho^*_{\mathrm{air}}(P^*_{\mathrm{ref}}, T^*_{\mathrm{ref}})$.

2.1.3 Fully Developed Calculations

To study the effects of different leaf hair traits on the aerosol deposition, the leaf surface is modeled as an infinitely large surface using the periodic assumption to reduce computational effort. More detail on the computational model is covered in Chapter 4. With the assumption of one-way coupling between fluid and particles (the flow is unaffected by the presence of particles), fully developed calculations can be used to establish the carrier phase independently, allowing a significant reduction in computational resources. The fully developed calculations are performed by applying periodic boundary conditions in the streamwise direction. Under such conditions, the reference velocity is chosen to be an effective friction velocity u_τ^* defined by:

$$U_{ref}^* = u_\tau^* = \sqrt{\frac{\tau_{w,eq}^*}{\rho_{ref}^*}} \tag{5}$$

, where $\tau_{w,eq}^*$ is an equivalent wall shear stress. Therefore, the reference Reynolds number takes the following form:

$$Re_{ref} = Re_\tau = \frac{\rho_{ref}^* u_\tau^* L_{ref}^*}{\mu_{ref}^*} \tag{6}$$

A brief description of the fully developed calculations is included in this paper; a more detailed description of the procedure can be found in Zhang et al.[13]. The total pressure, P^* is expressed in terms of a linear component and a modified fluctuating pressure, p^* as follows:

$$P^*(x_i, t) = P_{ref}^* - \beta^* x_i^* + p^*(x_i, t) \tag{7}$$

, where $\beta^* = \Delta P_x^* / L_x^*$ is the linear component of the mean streamwise pressure gradient. Non-dimensionalizing Eqn. (7) gives:

$$P(x, t) = -\beta x + p(x, t) \tag{8}$$

Fixing β at unity, the linear pressure variation accounts for the mean pressure drop across the streamwise periodic boundaries.

Substituting (8) into the conservation Eqn. (2) gives:

$$\frac{\partial}{\partial t}(\rho u_i) + \frac{\partial}{\partial x_j}(\rho u_i u_j) = -\frac{\partial p}{\partial x_i} + \frac{1}{Re_{ref}}\frac{\partial}{\partial x_j}\left[(\mu + \mu_t)\left\{\frac{\partial u_i}{\partial x_j} + \frac{\partial u_j}{\partial x_i}\right\} - \frac{2}{3}\delta_{ij}\frac{\partial u_k}{\partial x_k}\right] + \rho g_i + \beta e_x \tag{9}$$

, which results in the following periodic boundary conditions:

$$u_i(x + L_x, y + L_y, z) = u_i(x, y, z) \tag{10}$$

$$p(x + L_x, y + L_y, z) = p(x, y, z) \tag{11}$$

On the leaf surface, no-slip and no penetration boundary conditions are applied for the velocity, and the Neumann boundary condition is applied for the modified pressure:

$$\nabla p \cdot \vec{n} = 0 \tag{12}$$

, where $\vec{n}$ is the unit outward pointing vector normal to the surface.

Before simulating a case with particles, a steady flow field has to be first established to achieve a desirable bulk Reynolds number, $\overline{Re}$. Since the reference Reynolds number is based on the friction velocity, u_τ^*, and the pressure gradient is imposed in the x-direction, the calculated non-dimensional flowrate, $\dot{Q}_x$, and the streamwise area, A_{front} can be used to estimate the dimensionless mean velocity, $\overline{V}$ and compute $\overline{Re}$ as follows:

$$\overline{V} = \frac{\overline{V}^*}{u_\tau^*} \approx \frac{\dot{Q}_x}{A_{front}} \tag{13}$$

$$\overline{Re} = Re_\tau\left(\frac{\dot{Q}_x}{A_{front}}\right) \tag{14}$$

2.2 Species Transport

The dispersion of gaseous pollution can be modeled by the species transport model. In the flow where N species are present, the governing equation for species n in turbulent flow is expressed as

$$\frac{\partial}{\partial t}(\rho y_n) + \frac{\partial}{\partial x_i}(\rho u_i y_n) = \frac{1}{Re_{ref}Sc_{ref}}\frac{\partial}{\partial x_i}\left[\left(\rho D_n + \frac{\mu_t}{Sc_t}\right)\frac{\partial y_n}{\partial x_i}\right] + S_n \tag{15}$$

, where: y_n = mass fraction of species n

S_n = source term for species n

D_n = mass diffusion coefficient of species n; $D_n = D_n^*/D_{ref}^*$

Sc_{ref} = reference Schmidt number; $Sc_{ref} = \mu_{ref}^*/\rho_{ref}^* D_{ref}^*$

Sc_t = turbulent Schmidt number specified as 0.5 in this study

The dimensionless density ρ and dynamic viscosity μ in the mass, momentum, and species transport equations (Eqn. (1), (2), and (15)) are mixture properties. The non-dimensional mixture density for N species is defined by

$$\rho = \rho_{mix} = \frac{1}{\rho_{ref}^*}\frac{P_{ref}^*}{R_u^* T^*}\left(\sum_{n=1}^{N}\frac{y_n}{M_n^*}\right) \tag{16}$$

, where R_u^* is the universal gas constant (8314 J/kmol K), and M_n^* is the molecular mass of species n in kg/kmol.

The mixture viscosity μ can be computed as suggested by Wilke [14]:

$$\mu = \mu_{mix} = \frac{1}{\mu_{ref}^*}\left(\sum_{n=1}^{N}\frac{x_n\mu_n^*}{\sum_{m=1}^{N}x_m\phi_{nm}}\right) \tag{17}$$

, where μ_n^* is the absolute viscosity of species n in kg/m·s, x_n is the mole fraction, and ϕ_{nm} is defined as

$$\phi_{nm} = \frac{\left[1 + (\mu_n^*/\mu_m^*)^{\frac{1}{2}}(M_m^*/M_n^*)^{\frac{1}{4}}\right]^2}{(8 + 8M_n^*/M_m^*)^{1/2}} \tag{18}$$

For dilute gases, the binary-diffusion D_{12}^* between species 1 and 2 in Eqn. (15) can be computed using the following expression [15]:

$$D_{12}^* = \frac{0.001858(T^*)^{3/2}}{p_{ref}^*\sigma_{12}^*\Omega_D}\sqrt{\frac{M_1^* + M_2^*}{M_1^* M_2^*}} \tag{19}$$

, where: D_{12}^* = binary-diffusion coefficient, cm^2/s

Ω_D = diffusion collision integral

σ_{12}^* = effective collision dimeter, Å (10^{-10} m); $\sigma_{12}^* = (\sigma_1^* + \sigma_2^*)/2$

P_{ref}^* = reference pressure, atm

The diffusion collision integral Ω_D can be calculated using the following equations:

$$\Omega_D \approx 1.0(T')^{-0.145} + (T' + 0.5)^{-2.0} \tag{20}$$

$$T' = T_{ref}^*/T_{\varepsilon_{12}}^* \tag{21}$$

$$T_{\varepsilon_{12}}^* = \sqrt{T_{\varepsilon_1}^* T_{\varepsilon_2}^*} \tag{22}$$

, where $T_{\varepsilon_1}^*$ and $T_{\varepsilon_2}^*$ are effective temperatures of species 1 and 2 in K. In this paper, the subscript of D_{12}^* will be dropped out for simplicity since there are only two species: air and Sulfur Hexafluoride (SF_6), and the coefficient will be referred to as D^* and is the same as D_{ref}^* since the flow is assumed to be isothermal.

2.3 Dispersed Phase

In near-leaf-scale air quality assessment, it is reasonable to assume that the pollution concentration is very dilute, thus inter-particle collisions and the effects of particles on the fluid are negligible. In the multiphase regimes where particle motion is affected by the continuous-phase and not vice versa, the one-way coupling model can be used to describe such particle-fluid interactions with very small particle volume and mass concentration.

2.3.1 Particle Governing Equations

In such conditions, the force for a single particle is generally represented as a linear combination of different contributing forces. Neglecting thermophoresis force (since the energy equation is not taken into account in this study) and collisions between particles, the equations of particle motions per unit mass can be written as:

$$\frac{d\vec{x}_p}{dt} = \vec{u}_p \tag{23}$$

$$\frac{d\vec{u}_p}{dt} = \vec{f}_{drag} + \vec{f}_{lift} + \vec{f}_{brown} + \vec{f}_{buoy} + \vec{f}_{add} + \vec{f}_{hist} + \vec{f}_{press} \tag{24}$$

The forces are dimensionalized by $\vec{f} = \vec{f}^* L_{ref}^* / (U_{ref}^*)^2$. An order of magnitude analysis was conducted to determine which forces are significant for the computation, and it was found that drag and Brownian forces are the only forces that significantly affect the particle motions in the study (this will be confirmed later in the Results and Analysis section). Thus, Eqn. 2.16 becomes

$$\frac{d\vec{u}_p}{dt} = \vec{f}_{drag} + \vec{f}_{brown} \tag{25}$$

The flow and the particle Reynolds numbers are given as

$$\mathrm{Re} = \frac{\rho_f^* U_{ref}^* L_{ref}^*}{\mu^*} \quad (26)$$

$$\mathrm{Re_p} = \frac{\rho_f^* \|\vec{w}^*\| D_p^*}{\mu^*} \quad (27)$$

, where $\|\vec{w}^*\|$ is the magnitude of the relative velocity defined as $\vec{w}^* = \vec{u}_f^* - \vec{u}_p^*$. The subscripts f and p indicate values of fluid and particle, respectively.

2.3.1.1 Drag Force

Drag calculation assumes a quasi-steady incompressible uniform flow and can be described in terms of the Stokes number and the relative velocity:

$$\vec{f}_{drag} = C_{m,1} C_{m,2} \frac{\vec{w}}{\mathrm{Stk}} \quad (28)$$

The Stokes number is the ratio of the particle time scale to the fluid time scale as follows:

$$\mathrm{Stk} = \frac{\rho_p^* {D_p^*}^2}{18\mu_{ref}^*} \frac{U_{ref}^*}{L_{ref}^*} \quad (29)$$

The force is modified for high particle Reynolds number with $C_{m,1}$ which is defined by:

$$C_{m,1} = 1.0 + 0.15\mathrm{Re_p^{0.687}} \quad (30)$$

To allow slip at particle surface, Millikan's modification to Stokes' law is made using:

$$C_{m,2} = \frac{1}{1 + \mathrm{Kn_p}\left(1.2 + 0.41 \exp\left(\frac{-0.88}{\mathrm{Kn_p}}\right)\right)} \quad (31)$$

, where the particle Knudsen number is the ratio if the mean free path of the carrier fluid, λ^* to particle radius:

$$\mathrm{Kn_p} = \frac{\lambda^*}{D_p^*/2} \tag{32}$$

$$\lambda^* = \frac{2\mu^*}{\rho_f^* \bar{c}^*} \tag{33}$$

$$\bar{c}^* = \sqrt{\frac{8R^*T^*}{\pi}} \tag{34}$$

, where $\bar{c}^*$ is the mean molecular velocity, and R^* is the molar-weight-specific gas constant of the carrier fluid.

2.3.1.2 Brownian Force

Brownian force arises from discrete interactions with the surrounding molecules and can be expressed as:

$$\vec{f}_{\mathrm{brown}} = \vec{Z}\sqrt{\frac{\pi S_0}{\tau_{\mathrm{Brown}}}} \tag{35}$$

, where $\vec{Z}$ is the directional Gaussian white noise with zero mean and unit variance, τ_{Brown} is the Brownian time scale, and S_0 is a non-dimensional constant defined as:

$$S_0 = \frac{216C_{m,2}}{\pi^2 D_p^* \left(\frac{\rho_p^*}{\rho_f^*}\right)^2} \frac{1}{\mathrm{Re}} \frac{\kappa T_f^*}{\rho_f^* {L_{\mathrm{ref}}^*}^3 {U_{\mathrm{ref}}^*}^2} \tag{36}$$

, where κ is the Boltzmann constant (1.381×10^{-23} J/K). The Brownian time scale is taken to be 100 times larger than the non-dimensional molecular time scale. If the Brownian time scale is smaller than the computational time step, then it is set to the same value as the computational timestep.

$$\tau_{\mathrm{Brown}} = \begin{Bmatrix} 100\left(\dfrac{\lambda^*/L_{\mathrm{ref}}^*}{\bar{c}^*/U_{\mathrm{ref}}^*}\right) & \text{if} \;\; \tau_{\mathrm{Brown}} > \Delta t \\ \Delta t & \text{if} \;\; \tau_{\mathrm{Brown}} \le \Delta t \end{Bmatrix} \tag{37}$$

2.4 Solution Procedure

GENIDLEST solves the problem using a pressure-based framework. In this framework, the solution algorithm computes the intermediate Cartesian velocity field by neglecting the effect of the pressure gradient. After obtaining the intermediate velocity field, the continuity equation is used to derive the pressure question, and the calculated pressure field is used to correct the intermediate velocity field to satisfy discrete continuity. The governing conservation equations are solved in a finite-volume framework. The Cartesian quantities are calculated and stored at the cell center, while the fluxes are calculated and stored at the cell faces. The convection and viscous terms in the Navier-Stokes equations and the species transport equation are treated implicitly by the Crank-Nicolson method. Nominally the convection and diffusion terms are discretized using the second-order central difference scheme (SOC). For simulating the street canyon, the SOC approximation of the convection terms is limited by a first-order upwind (FOU) scheme. Each fluid time step is iterated until the residuals converge to 10^{-6} for the momentum equations and the species transport and 10^{-9} for the pressure solver. A preconditioned BiCGSTAB method is used to solve the linear systems [16].

All simulations were run on the Advanced Research Computing (ARC) Cascades clusters. More information on this computing system can be found at https://www.arc.vt.edu.

CHAPTER 3: POLLUTION DISPERSION IN STREET CANYON

This chapter introduces the review of existing literature which validate their simulations with the data available on the online database CODASC (COncentration DAta of Street Canyons)[2] [17], methodology, followed by results, and discussion. Flows over street canyons with the width-to-height (W/H) ratio of 1 and 2 have been investigated. However, only the W/H = 1 results are included in this chapter, and the W/H = 2 results can be found in Appendix A.

3.1 Introduction and Literature Review

In spite of advances in computational hardware and numerical methods, complicated geometries and turbulence resolved simulations often result in an expensive computational cost. A generic urban configuration such as a street canyon with near-ground emission poses such challenges to researchers. There are many turbulence models derived from different approximations such as Reynolds Averaged Navier-Stokes (RANS), Unsteady RANS (URANS), Large-Eddy Simulation (LES) and hybrid URANS/LES. Among these different models, RANS is the most widely used approach in the field of urban physics mostly due to its lower computational cost relative to other turbulence models [18], [19].

Despite RANS' ability to produce satisfactory results, RANS is widely known and observed by different studies [18]–[28] to be inferior to LES simulations because of its lower accuracy when compared to experimental measurements and its inability to produce time-varying fluctuations. For microscale climate modeling at pedestrian-level, instantaneous

[2] The measurements available on the database are from the experiments conducted in a wind tunnel at Karlsruhe Institute of Technology (KIT), Germany

information is critical since pedestrians are more likely to be exposed to pollution on a short-time basis. Moreover, vortices predicted by steady RANS are generally weaker than wind tunnel observation and LES [29]–[31]. This under-prediction could be caused by smaller turbulent kinetic energy along the canyon roof thus inducing smaller shear [32].

Although RANS comes with limitations in modeling important characteristics of turbulent flow around bluff bodies in urban physics, the approach remains popular in the field of urban physics. Over 96% of the studies between 1998-2015 documented by Toparlar, et al. [5] are reported to use RANS to model pollutant dispersion in the urban environment.

On the other hand, LES' ability to produce time-dependent unsteady flow and capture transient mixing, which is common in a street canyon setting, makes it beneficial in the field of micro-climate research. However, only 2% of the street canyon studies published in the period of 1998-2015 were reported to have utilized LES [5]. This is likely due to the higher computational complexity of LES, as well as the lack of best practice guidelines for urban physics studies, whereas RANS constitutes an acceptable compromise [19], [32], [33].

Regardless, LES seems to be gaining more popularity in the field. Among the 11 micro-climate studies for the street canyon of width to height ratio, W/H = 1 from the period of 2008 to 2019, which validate simulations using an online database [17], there is an equal share of studies using RANS and using LES, indicating a larger acceptance in this field, especially in the recent years [29], [31]–[40]. A summary of these studies along with those which investigate the W/H = 2 canyon can be found in Table 1. The generic street canyon studies which do not reference CODASC data are also tabulated in Table 2.

Table 1 Studies with validation using the CODASC data; Line source refers to a continuous source, and "point source" refers to a series of discrete points

Year	Title	W/H	CFD Solver	CFD model	Turb Model	Sct	Re	Inlet V, m/s	Scale H [m]	Mesh type	Δx [m]	Δz [m]	Δy [m]	dt min [s]	Number of cells in millions (Domain size)	Sim. time [s]	Source model
2008	C. Gromke, R. Buccolieri, S. Di Sabatino, B. Ruck [29]	1	Fluent	RANS	k−ε, RSM	0.3, 0.6, 0.7			1:1	hexa	H/20	H/20	H/2		0.3 (41H×8H×??H)		
2009	M. Balczó, C. Gromke, B. Ruck [35]	1	MISKAM	RANS	k−ε				1:1	hexa	H/180	H/180	H/90		5.8		source cell
2015	S. Vranckx, P. Vos, B. Maiheu, S. Janssen [31]	1,2	Simple FOAM	RANS	k−ε				1:1	hexa + unst	H/20	H/35	H/20		5 (24/25H×20H×6H)		mass flux
2015	Jeanjean A Hinchliffe G McMullan W Monks P Leigh R [36]	1	OpenFOAM	RANS	k−ε		3.6E+4	4.7	1:150	hexa	H/16	H/20	H/16		0.64 (63H×8H×70H)		line source
2017	G. Kang, J.J. Kim, D.J. Kim, W. Choi, S.-J. Park [41]	1	–	URANS	RNG k−ε				1:1	hexa	H/12	H/12	H/4		6 (41H×8H×30H)	7.2E+03	source cell
2018	Yuan C Shan R Adelia A Tablada A Lau S et al. [38]	1	Fluent	RANS (then LES)	k−ε; RSM				1:1	hexa	H/40			5.00E-02	8 (44H×8H×30H)	5 FT	
2011	S.M. Salim, S.C. Cheah, A. Chan [39]	1	Fluent	RANS	k−ε, RSM				1:150	cubic	H/13				1.20 (30H×8H×24H)		source cell
				LES	dyn SGS									1.25E-01		20 s averagin g	
2011	Salim S Buccolieri R Chan A Di Sabatino S Cheah S [42]	1	Fluent	LES	dyn SGS				1:150	cubic	H/13			1.25E-01	1.10 (30H×8H×24H)	170 s averagin g	line sources
2013	P. Moonen, C. Gromke, V. Dorer [40]	1	Fluent	LES	dyn SGS				1:150	cubic	H/24			1.25E-03	1.20 (25H×8H×24H)	10 s averagin g	point source
2018	Merlier et al.[32]	1	ProLB	LES	Hybrid LBM-LES	0.7			1:1		H/96			1.44E-05	41 (25H×7H×8H)	25	line source
2019	J. Gallagher, C. Lago [34]	1	Fluent	LES			1.0E+6	0.8	1:1	tri-tetra	H/100	H/10	H/20	(2H×1.5H×10H)			surface source
							1.0E+7	8.0									
2009	R. Buccolieri, C. Gromke, S. Di Sabatino, B. Ruck [43]	2	Fluent	RANS	RSM				1:1		H/25	H/25	H/5		0.4 (40H×8H×??H)		line source
2011	R. Buccolieri, S.M. Salim, L.S. Le o, S.Di Sabatino, A. Chan, P. Ielpo, G. de Gennaro, C. Gromke [42]																
2015	K. Abhijith, S. Gokhale [44]	2	Fluent	RANS	k−ε				1:150	hexa	H/24				(30H×8H×24H)		line source
2017	F. Xue, X. Li [45]	2	PHEONICS	RANS	k-ε MMK	1			1:1	hexa	H/22	H/30	H/36		4.70 (29H×8H×28H)		line source
	This study	1, 2	GenIDLEST	LES	dyn SGS	0.5	3.5E+4	4.62	1:150	hexa	H/588	H/763	H/500	5E-4 H/U	1.59 (41/42H×8H×H/190)		point source

Table 2 Generic street canyon studies with no reference to CODASC measurements.

Year	Authors	W/H	CFD Solver	CFD model	Turb Model	Re	Inlet V, m/s	H [m]	Scale H [m]	Mesh type	Δx [m]	Δz [m]	Δy [m]	dt min [s]	Number of cells in millions	Sim. time [s]	Source model
2007	Xie X, Liu C, Leung D, 2007 [46]	0.1, 0.5, 1, 2	Fluent	RANS	k−ε RNG	3.8E+03				uns					3.2 – 4.4		Single line source
2010	X. Li, R. Britter, T Koh, L. Norford, C. Liu, D. Entekhabi, D. Leung [47]	1		LES	one-equation SGS	4.0E+03					H/188		H/32	0.005 H/U			Single line source
2010	Kyung-Hwan Kwak · Jong-Jin Baik · Sang-Hyun Lee · Young-Hee Ryu, 2010 [48]			RANS	k−ε RNG	2.5E+06 – 7.6E+06	2.00 - 6.00	20	1:5		H/40		H/20	1.0E-01		24 h	No source
2014	de Lieto Vollaro A De Simone G Romagnoli R Vallati A Botillo S et al., 2014 [49]	0.5, 1, 2	Fluent	RANS		2.5E+06	2.00	20		hexa	H/20	H/40	H/20				No source
2014	S. Bottillo, A. Vollaro, L. de, G. Galli, A. Vallati, 2014 [50], [51]	1	Fluent	RANS	k−ε	2.5E+06 5.1E+06	2.00 4.00	20		hexa	H/20	H/40	H/20				No source
	This study	1, 2	GenIDLEST	LES	dynamic SGS	3.5E+04	4.62	0.12	1:150	hexa	H/588	H/763	H/500	0.0005 H/U	1.59		Point source

Comparing the performance of LES and RANS simulations for this particular geometry in reproducing the results as observed in the wind tunnel, Salim et al. [39] observed LES to predict the dispersion and resolve unsteady fluctuations more accurately than RANS and suggested that the model is more suitable where more detailed predictions are desired.

Due to LES's increasing popularity, the present study aims to replicate CODASC's experimental and numerical investigations on pollution dispersion in a street canyon with W/H = 1 and 2 using a geometrically simpler model with LES while maintaining as much detail as possible. Again, only the W/H = 1 results will be discussed in this chapter, and the W/H = results can be found in Appendix A. The model's performance assessment in reproducing the experimental data is conducted and compared to other LES studies where the full domain is used [32], [40], [41]. For W/H = 1, the study compares the predictions to the LES simulation results from Moonen et al. [40] as well. The study focuses on the wind flowing perpendicularly to the street canyon since this wind direction, which is the most critical for street canyon pollution accumulation [33].

The primary attention is given to the central region of the street canyon where the pollutant concentration is the highest as shown in Figure 2 [52]. Based on RANS and LES simulations, discrepancies between experimental and simulation results are also observed to be the largest in this region of the 1H×1H×10H canyon by Balczó et al. [53] and Moonen et al. [40], respectively. Moreover, since the middle region is dominated by the primary canyon vortex, and the flow field is no longer penetrated by the corner eddies from either ends of the canyon [52], the flow can be assumed to be statistically two-dimensional in the mean. To allow the three-dimensional geometry of the discrete jets to be included in this framework, a periodic domain of one discrete jet pitch is simulated along the length of the canyon (y-direction in Figure

2 below). This serves the purpose of simulating a repeating array of discrete jets *ad infinitum* replicating the conditions in the middle region of the canyon, and at the same time keeping the computational costs minimal by limiting the length of the canyon to one jet pitch. One consequence of this approach is that because of the small extent of the domain along the length of the canyon, three-dimensional instabilities will not be admitted in the solution and the flow will essentially exhibit two-dimensional characteristics.

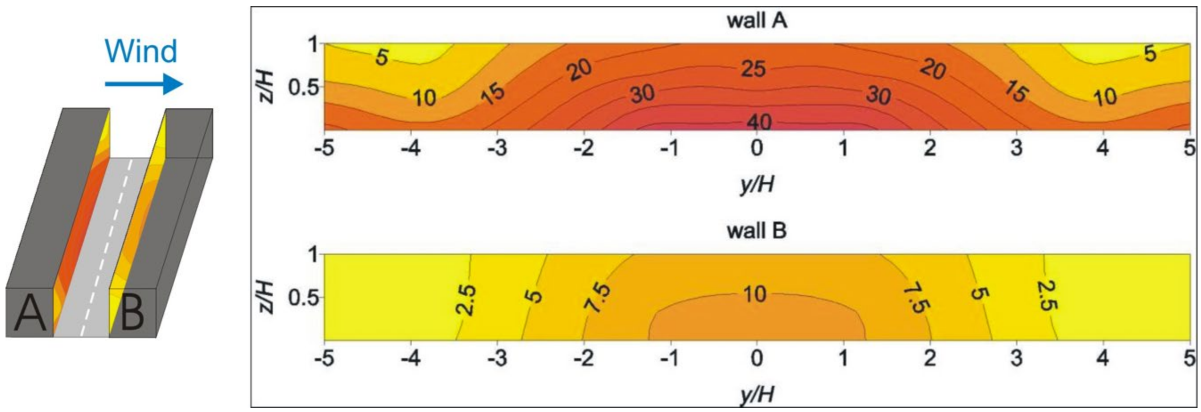

Figure 2 Normalized pollution concentration from the experiment conducted at Karlsruhe Institute of Technology (KIT) showing higher concentration in the middle region (y/H = 0) of both walls. There is also higher concentration on the leeward wall (Wall A) than the windward wall (Wall B) [17].

3.2 Geometry

To replicate the 1:150 scaled street canyon measurement conducted in an atmospheric boundary layer wind tunnel at Karlsruhe Institute of Technology (KIT) [17], a geometry depicted in Figure 3 was generated for W/H = 1, where the buildings are H in height. The computational domain is 41H×8H×H/190. The upstream and downstream distances are 8H and 30H (Note: the experiment assigns z-axis to the vertical direction and y-axis to the spanwise direction). The best practice guidelines, COST 732 [40], [54], require the vertical extension to be at least 5H above the building roofs and the upstream and downstream distances to be at least 5H and 15H, respectively. These criteria are satisfied in this study.

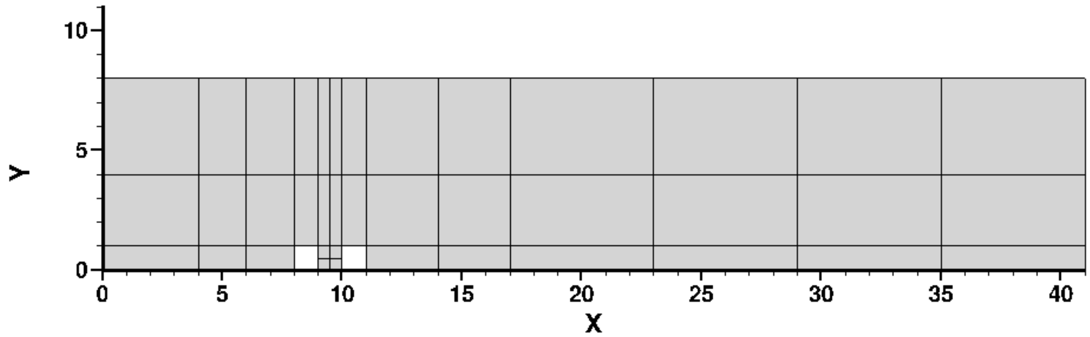

(a)

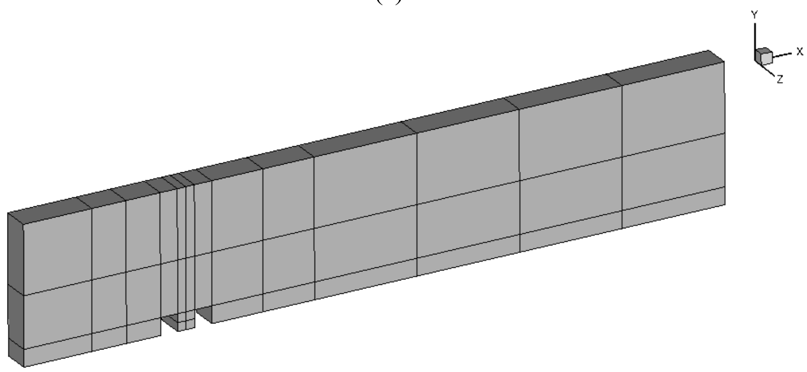

(b)

Figure 3 Street canyon with the dimensions of 41H x 8H x H/190 and W/H = 1. Figure (a) shows x-y view, and Figure (b) shows the three-dimensional view (the depth is not to scale since it is very small relative to other dimensions). Lines delineate computational blocks.

The building height of H = 0.12 m is used as a reference length in the simulation, L^*_{ref}. Cell size distribution along the x- and y-axes are plotted in Figure 4. The height of the cells inside the street canyons is made finer than the outside to capture emission dispersion inside the canyon. Δx is uniformly H/588 across the canyon width, and Δy is finest at the floor with the value of H/500. In order to resolve each discrete emission source, the cells along the z-direction are also uniformly H/763 across the entire domain (more information can be found in Section 3.3.3).

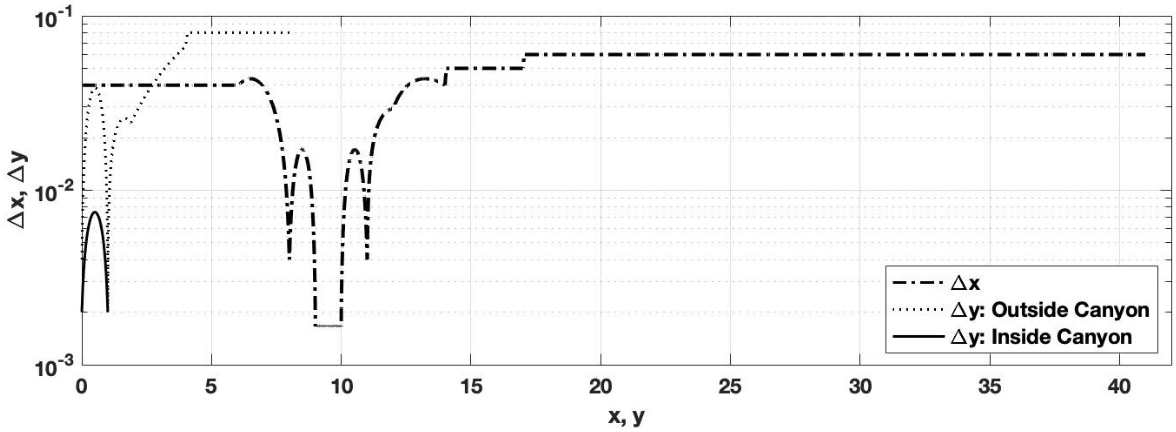

Figure 4 Street canyon grid cell size distribution along the x- and y- directions ranging from H/588 to H/16 for Δx, and H/500 to H/12.5 for Δy. The cell size along the z-direction is equally H/763 = 1.57 x 10^{-4}, thus not plotted.

Outside the canyon, the cells are finest near the building walls and become coarser as they are further away from the building walls. The grid consists of 1,592,000 computational cells.

Using RANS, Balczo et al. performed grid sensitivity study and found that a grid with resolution finer than Δx = H/180 (the smallest element size used) showed no further improvement. Comparing the LES results using the grid resolutions of Δ = H/48 and Δ = H/96, Merlier et al. [32] found that the finer grid yielded better agreement with the measurements but also showed higher concentration than the coarser grid, especially on the leeward side.

In the wind tunnel experiment [40], two series of flush-mounted and equidistantly-spaced hypodermic 0.4 mm diameter tubes, illustrated in Figure 5, are used as line sources to represent traffic exhaust.

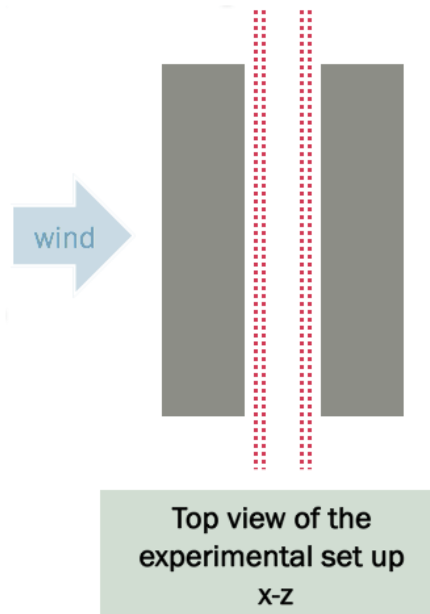

Figure 5 Top view (x-z) of the street canyon in the experiment. Note that in the computational simulation conducted in this study, the canyon is infinitely long, and the domain contains only one row of four hypodermic tubes.

For simplicity of grid generation, the grid is orthogonal and structured, and the 0.4 mm diameter tubes in the model are approximated by rectangular jets. Each jet consists of four equally sized grid cells (i.e. each jet is H/300 x H/382, see Figure 6a). The area of these jets is within 1% of the actual jets used in the experiment. As illustrated in Figure 6b, the grid contains four jets which represent the four-line sources across the cavity width. There is one jet in the z-direction for each series to reduce grid generation time and computational cost of the simulation. A series of discrete sources, termed "point sources", are used instead of a continuous line source to preserve the mixing process, if any, induced by the jets. It is noteworthy that the studies which used more simplified methods for modeling the emissions, such as a continuous line, area, or volume-averaged source, also reported a qualitatively good agreement with the experimental results [31]–[34], [36], [53].

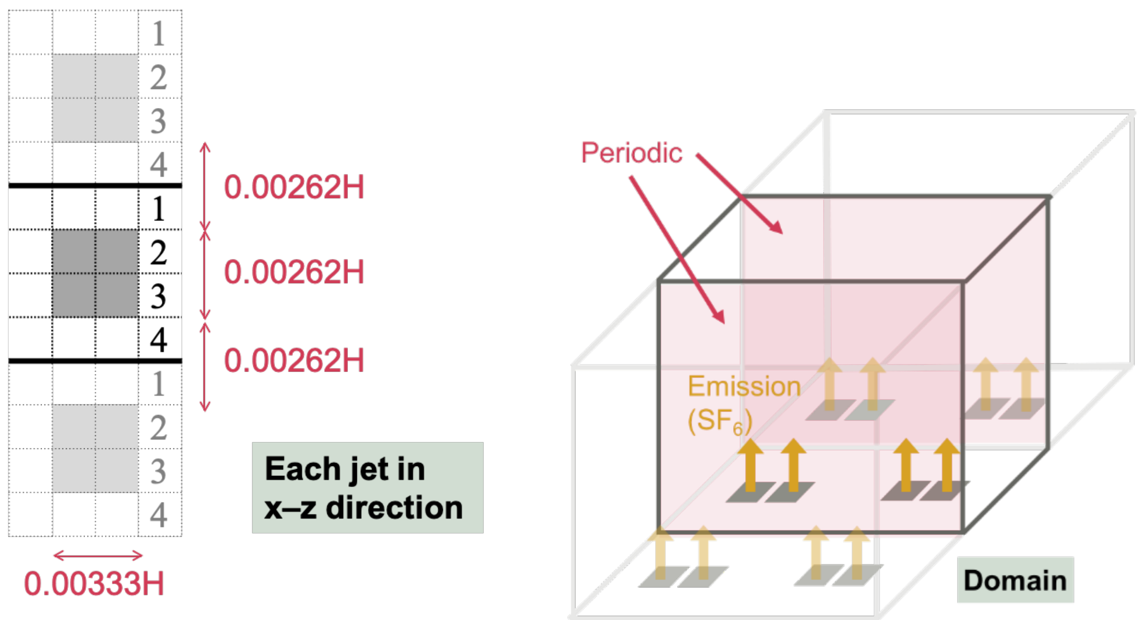

(a) (b)

Figure 6 (a) x-z view (top view) of a single jet used in the computational domain. The grey shaded area is to demonstrate the periodic condition of the z-walls and equidistant jets; (b) x-y-z view of the domain showing all four point-sources with v-velocity. The blocks before and behind the domain are for demonstrating the periodic condition.

A summary of ranges of cell sizes, number of grid elements, time step used in different studies including the ones referencing CODASC data ([29], [31]–[34], [36]–[40], [42]–[45], [53]) and the ones which examine generic street canyons ([46]–[51]) is shown in Table 3. While the grid density used in this study is much finer than other studies, the total amount of cells is in the lower range because of the much smaller domain size in the z-direction.

Table 3 Summary of grids used for different studies on W/H = 1 and W/H = 2 canyons. The asterisk represents studies which didn't validate their results with CODASC data

Model	W/H	Method	Δx	Δy	Δz	Domain Size x	Domain Size y	Domain Size z	Cell numbers ($\times 10^6$)	Time step, s
RANS	1	k-ε, RSM, k-ε MMK	H/16 - H/180	H/13 - H/180	H/2 - H/90	24H – 63H	8H – 20H	6H – 70H	0.3 - 8	N/A
	2	k-ε, RSM, k-ε MMK	H/25 - H/20	H/30 - H/24	H/36 - H/5	24H – 40H	8H – 20H	6H – 28H	0.4 - 4.7	
URANS	1	RNG k-ε	H/12	H/12	H/4	41H	8H	30H	6	
LES	1	Dynamic SGS; Hybrid LBM-LES	H/100 - H/13	H/96 - H/13	H/96 - H/13	2H - 30H	1.5H – 8H	8H – 24H	1.1 - 41	10^{-5} - 10^{-1}
RANS*	0.5-2	RANS: k-ε, RNG k-ε	H/40 - H/20	H/40	H/32 - H/20				0.3 - 6	N/A
LES*	1	One-equation SGS	H/188	H/188	H/32				N/A	10^{-4}
This study: LES	1-2	Dynamic SGS	H/588	H/763	H/500	41H – 42H	8H	H/190	1.6 -2.4	10^{-5}

The reference properties and species properties used for the computation are tabulated in Table 4 and Table 5. The binary mass diffusivity coefficient shown in Table 4 is found using Equation (19) and the effective temperatures of 78.6 K and 222.1 K for air and SF6, respectively. This results in the mass diffusion coefficient of 0.099 cm^2/s at 300 K and 1 atm. This value is within 2% difference from the binary mass diffusion coefficients of SF_6 in N_2 and O_2 at 298 K given by Worth et al. [55].

Table 4 Reference values

Velocity, U^*_{ref} (m/s)	4.65
Length, L^*_{ref} (m/s)	0.12
Pressure, p^*_{ref} (Pa)	101,000
Temperature, T^*_{ref} (K)	300
Density, ρ^*_{ref} (kg/m^3)	1.1731
Absolute viscosity, μ^*_{ref} (kg/ms)	1.8459×10^{-5}
Molecular weight, M^*_{ref} (kg/kmol)	28.97

Table 5 Summary of species properties

	SF_6	**Air**
Density, ρ^*_{n} (kg/m^3)	5.9143	1.1731
Absolute viscosity, μ^*_{n} (kg/ms)	1.42×10^{-4}	1.8459×10^{-5}
Effective temperature, T_ε (K)	222.1	78.6
Mass diffusivity, D^*_{n} (m^2/s)	9.9×10^{-6}	
Turbulent Schmidt number for species, Sc_{t} (-)	0.5	
Molecular weight, M^*_{n} (kg/kmol)	146.055	28.97

3.3 Boundary Conditions

To create an infinitely long street canyon, the periodic boundary condition is used on the lateral boundaries of the domain (i.e. along the z-direction). The boundary conditions are summarized in Figure 7 and described in detail in the following sections.

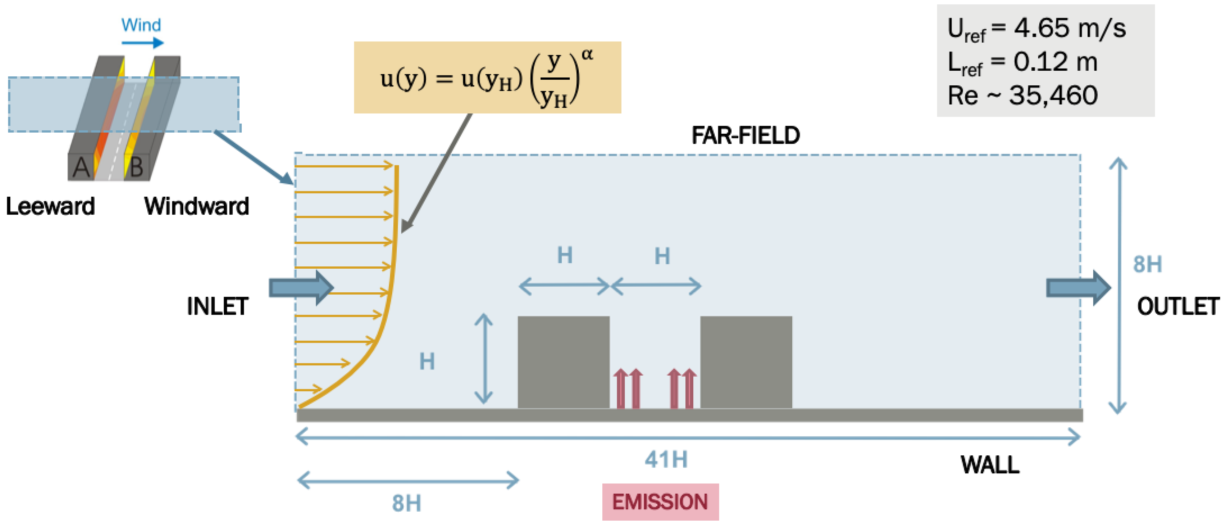

Figure 7 Computational domain and boundary conditions for W/H = 1 (x-y directions). The street canyon figure on the top left is taken from Moonen [40].

3.3.1 Inlet and Outlet

To simulate a typical urban environment, the wind profile power law with mean velocity, $u_H^* = 4.39$ m/s at the building height, $y_H^* = 0.1$ m and the exponent α of 0.30 is specified for the inflow condition when the mean streamwise flow velocity at height y, u(y) is lower than 1.5 [17]. The wind profile is as follows

$$u(y) = \frac{u_H^*}{U_{ref}^*}\left(\frac{y}{y_H/L_{ref}^*}\right)^{\alpha} \quad \text{if } u(y) < 1.5 \tag{38}$$

The generated profile plotted against the experimental data is shown in Figure 8. The mass fraction of SF_6 is set to zero at the inlet. The outflow plane is placed far downstream (30H) of the second building. The gradients of velocity and species are set to zero. Unlike some previous studies, time-dependent inlet turbulence is not used in this study – this decision is justified by the observation that large turbulent fluctuations are produced in the separated shear layer from the first building which will dominate momentum and species transport in the canyon and the effect of any freestream turbulence in the canyon will be minimal.

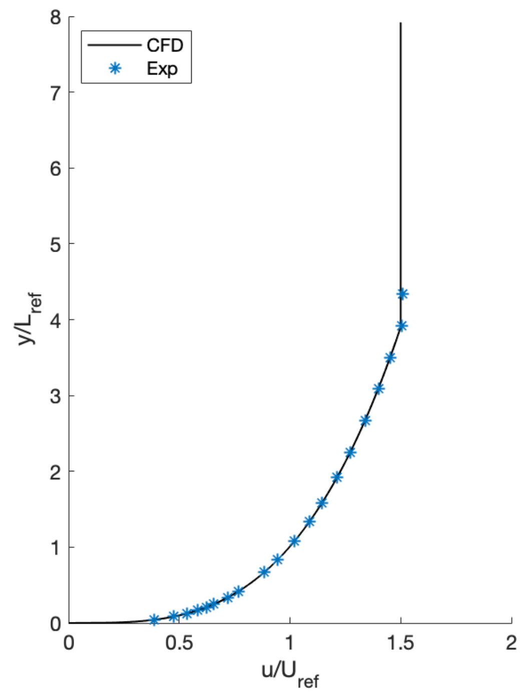

Figure 8 Inlet velocity profile measured in the experiment (blue stars) and generated by GENIDLEST (black solid line).

3.3.2 Top and Bottom Boundaries

With the domain height of 8H, the flow along the top boundary is assumed to be no longer affected by the boundary layers on the ground. The cross-stream v-velocity normal to the boundary is set to zero with zero gradient conditions imposed on the boundary parallel components (u, w) and the species mass fraction. The street canyon surfaces are considered as no-slip impermeable surfaces to both air and SF_6. The boundary condition used for the SF_6 jets is described in the next section.

3.3.3 Emission

The emission is modeled with an infinite series (in the z-direction) of four jets or point sources by assuming periodicity. Physically this represents conditions deep inside the canyon where end-effects of the finite sized canyon in the z-direction are not felt. The flowrate is approximated using a 0.40 x 0.31 mm^2 area with the v-velocity component of 0.130780 m/s, resulting in the jet Reynolds number of about 3. The air and SF_6 mass fraction of 0.9953 kg air and 0.0047 kg SF6 per kg mixture are assigned respectively to replicate the pollution emission from vehicles (calculation procedure will be discussed later in this section). Each pair of point sources is 0.23H and 0.35H away from the walls of the building. The experimental and computational set-ups are shown earlier in Figure 5 and Figure 6, respectively.

In determining the jet velocity, the mixture mass flowrates, $\dot{m}^*_{mix}$ and mass fractions for each species n, y^*_n are calculated from the given volumetric flowrates $Q^*_{exp,n}$ of 6.5 cm^3/min and 7000 cm^3/min for SF_6 and air, respectively, and using the following relationships [40]:

$$\dot{m}^* = \rho^* Q^* \tag{39}$$

$$\dot{m}^*_{mix} = \dot{m}^*_{SF_6} + \dot{m}^*_{air} \tag{40}$$

$$y_{air} = \frac{\dot{m}^*_{air}}{\dot{m}^*_{mix}} \tag{41}$$

$$y_{SF_6} = 1 - y_{air} \tag{42}$$

To obtain the mixture flowrate, the mixture density is first calculated using Eqn. (16). For a 1.42 m long series of 0.4 mm diameter jets used in the experiment, it is assumed that there are 1,775 jets on each line source. The mixture flowrate and the total area of the jets were used to estimate the jet velocity, resulting in the dimensionless jet velocity of 2.8125×10^{-2}. Computed properties and values used in the calculations are summarized in Table 6.

Table 6 Summary of species properties

	SF6	Air	Mixture
Density, ρ_n^* (kg/m3)	5.9143	1.1731	1.177
Experiment flowrate, Q_{exp}^* (cm3/min)	6.5	7000	N/A
Molecular weight, M_n^* (kg/kmol)	146.055	28.97	N/A
Mass fraction, y_n^* (kg/kg of mixture)	0.0047	0.9953	1

3.4 Initialization and Simulation criterion

The simulation is run until the time-dependent flow field exhibits stationary conditions and becomes independent of the initial conditions. To achieve this state, the simulation is run for 10 flow-through times (t = 10.6 s, 1 flow-through is the time taken for the flow to traverse the domain at the mean flow velocity). Then, the Cartesian velocity vector, pressure, and species mass concentration are statistically averaged, and the turbulence quantities are calculated starting from the 11th flow-through (t = 11.6 s). The simulation ends after the mean and turbulence quantities have been computed for 4 and 5 flow-throughs (4.23 s and 5.29 s), respectively. One flow-through in the canyon takes 41 non-dimensional time units (which is about 1.06 s and costs up to 3,000 CPU hours). Table 7 summarizes this information. Figure 9 shows time-dependent concentration information from 6 locations inside the street canyon (three from each wall). As shown in Figure 9, a period of two flow-throughs (82 non-dimensional time) would have been sufficient to obtain statistically averaged data.

Table 7 Summary of simulation time for W/H = 1 canyon.

Canyon	CPU hours for one flow-through	Time	Flow establishment period	Mean flow averaging period	Mean turbulence averaging period
W/H = 1	3,000	Flow-throughs	10.0	5.0	4.0
		Simulated time, s	10.6	5.29	4.23

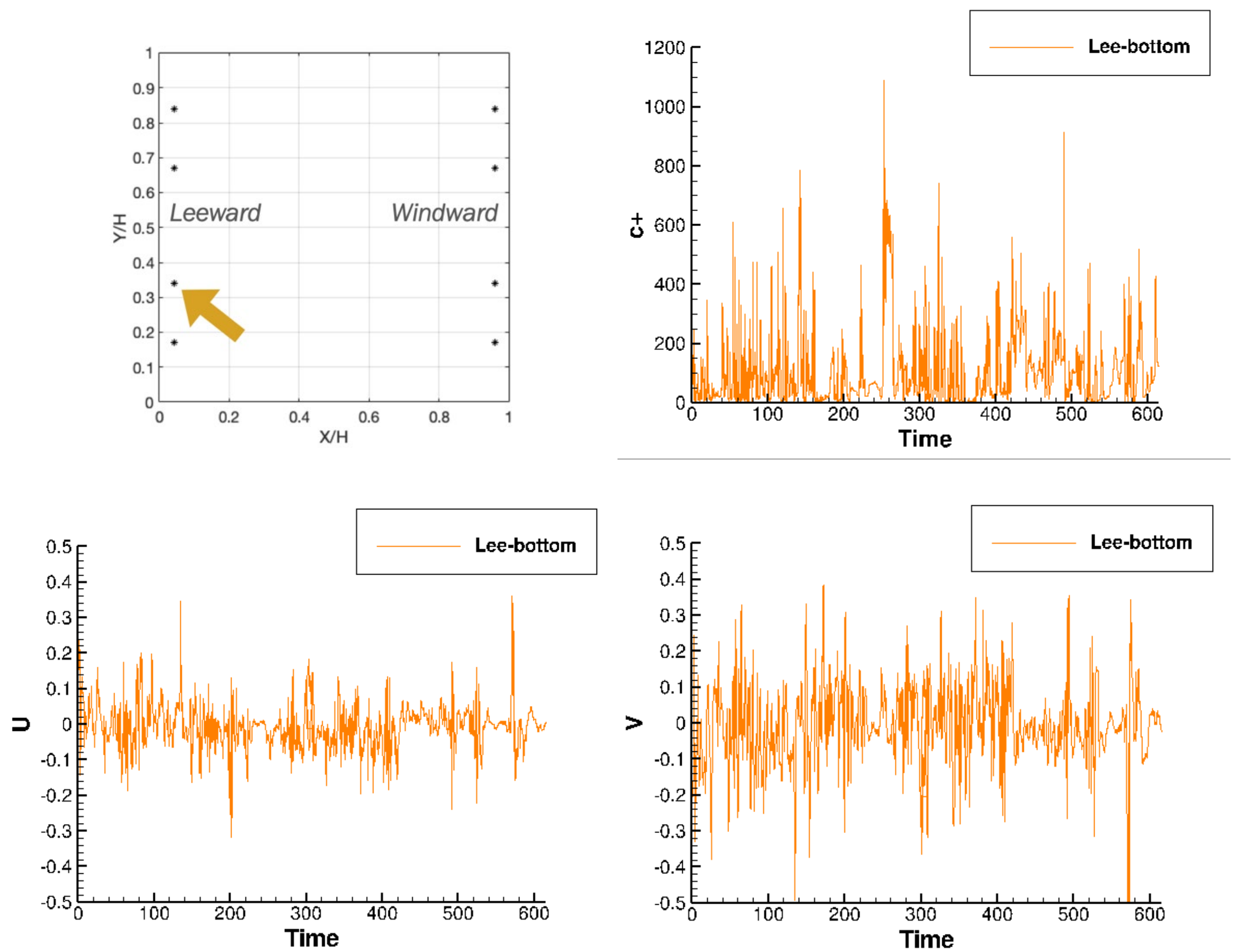

Figure 9 Normalized concentration, u- and v-velocities as a function of non-dimensional time for W/H = 1 canyon. The probe is located near the leeward wall in the lower region (0.04H, 0.34H)

3.5 Method for Data Analysis

The mean quantities are used to calculate normalized concentration profiles of SF_6 on each side of the street canyon walls and compared with two sets of 7 measurement points taken at the vertical plane of symmetry and along a plane 5 mm away from the walls [40]. The measured mole fraction, x_{SF_6} is normalized as follows:

$$c^{+} = \frac{x_{SF_6} L^{*}_{ref} U^{*}_{ref}}{Q^{*}_{SF_6}/\ell^{*}} \tag{43}$$

, where c^{+} is normalized concentration, and $Q^{*}_{SF_6}/\ell^{*}$ is the emission flowrate per unit length; ℓ^{*} is equivalent to the domain depth in this study. The measured mole fraction, x_{SF_6} is obtained from the SF_6 mass fraction, y_{SF_6} obtained from the simulation, using the following expression:

$$x_{SF_6} = y_{SF_6} \frac{\overline{M}^{*}}{M^{*}_{SF_6}} \tag{44}$$

, where $\overline{M}^{*}$ is the average molar mass of the air-SF_6 mixture; $\overline{M}^{*} = \left(\sum_{n=1}^{N} y_n / M^{*}_n\right)^{-1}$. Solving the simultaneous equation, the conversion equation is obtained:

$$x_{SF_6} = \frac{M^{*}_{air} y_{SF6}}{M^{*}_{air} y_{SF6} + M^{*}_{SF6}(1 - y_{SF6})} = \frac{0.24743 y_{SF6}}{1.24743 - y_{SF6}} \tag{45}$$

One important advantage LES simulations have over Reynolds Averaged Navier Stokes (RANS) simulations is the record of instantaneous information. This information is vital in the analysis of the impacts of pollution on pedestrians since most pedestrians are more likely to be exposed to instantaneous concentration. After normalizing the concentrations, the turbulence quantities are taken into account to estimate the fluctuations. The root-mean-square fluctuation of SF_6 mass concentration $\left(y'_{SF_6}\right)_{rms}$ from t_0 to $t_0 + T$ is given as an output:

$$\left(y'_{SF_6}\right)_{rms} = \left(\overline{{y'_{SF_6}}^2}\right)^{1/2} = \left(\frac{1}{T}\int_{t_0}^{t_0+T} {y'_{SF_6}}^2 \, dt\right)^{1/2} \tag{46}$$

This value could be crucial where the mean field is weak and fluctuations are more dominant, allowing for the prediction of instantaneous maximum and minimum concentration in the street canyon.

3.6 Results and Analysis

For street canyons of identical building heights, flow regimes and vortex characteristic can be characterized as illustrated in Figure 10 according to different W/H ratios. The flow field inside a street canyon is similar to a classic moving lid-cavity problem but with the presence of externally induced fluctuations. According to Sini et al. [56], the flow inside the canyon of W/H = 1 is classified to be in the skimming flow regime. Therefore, one primary circulation is expected in this study. Results and discussion for the W/H = 2 can be found in Appendix A.

Flow regimes	Fully independent wake flow	Isolated roughness flow	Wake interference flow	Skimming flow
W/H	50 — 8~10 — 5 — 1.5 — 0.6			
Vortex characteristic	Two co-rotative vortices		One primary	Contra-rotative vortices

Figure 10 Flow regimes in symmetric street canyons as a function of W/H ratios. (Adapted from Xie et al. 2007 [46]; Source: Sini et al. [56])

3.6.1 Mean flow

To understand the emission dispersion process, the flow fields need to be first examined. Figure 11 shows the contour of the mean streamwise velocity with stream tracers at the Z/H = 0 plane. The velocities are non-dimensionalized by U^*_{ref}. The typical features of the flow over a canyon in a skimming flow regime are observed: corner junction vortices in front of the upstream building and a large circulation region behind the canyon.

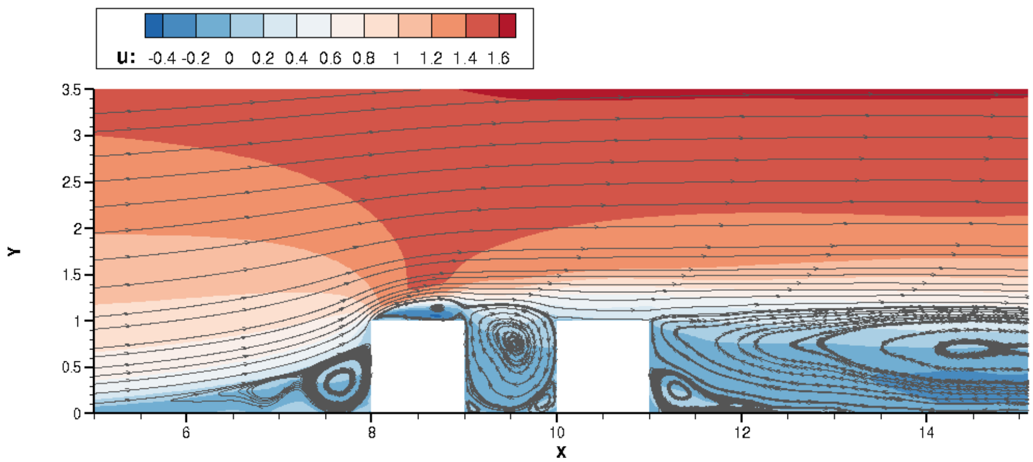

Figure 11 Interpolated values at Z/H = 0 of mean dimensionless streamwise velocity contour with stream tracers of the W/H = 1 canyons (entire domain not shown)

Shown in Figure 12 are the streamlines from the experimental data [35] and from the simulations. The size of the vortices in front of the upstream building is comparable to that of the experiment. The predicted separation bubble at the roof extends longer towards the canyon. This separation bubble at the roof of the windward building allows the canyon vortex to extend higher above the canyon height, thus enabling transporting fluid from inside the canyon. Inside the canyon (Figure 11 and Figure 12), there is one primary clockwise circulation with two counter-clockwise eddies in the bottom corners, as predicted.

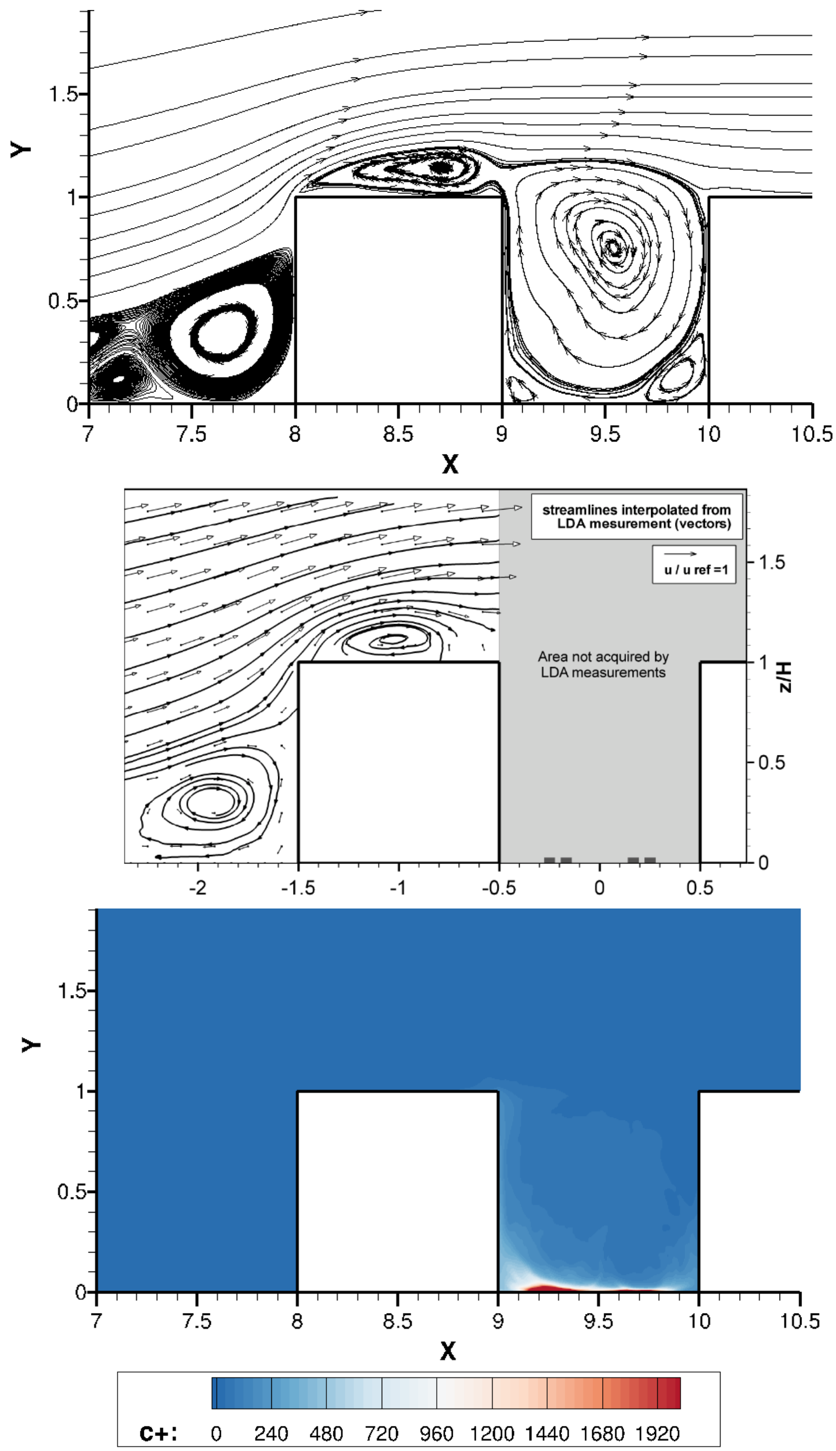

(a)

(b)

(c)

Figure 12 Comparison of mean streamlines (a) from wind tunnel data near midplane [35] and (b) current simulation. (c) Mean concentration of SF_6 in canyon .

These primary and corner vortices play significant roles in dispersing the pollution inside the canyon. As illustrated in Figure 12, the primary circulation carries the pollution clockwise towards the leeward wall. The counter-rotating corner eddy near the leeward side can act as a pollutant trap if the pollutant gets entrained in the weak recirculation of the corner eddy, or on the other hand, a sufficiently strong primary eddy can facilitate the transport of pollutant upward and out of the canyon.

Figure 13 plots the u- and v-velocity at different y- and x-locations, respectively, together with the concentration (c^+) of SF_6 at different y-locations near the bottom leeward side of the canyon. The u-velocity in the bottom quarter of the canyon is indicative of the transport of the pollutant (SF_6) from the injection location on either side of the center of the canyon to the leeward side, whereas the magnitude and direction of v-velocity are indicative of the vertical transport of the pollutant of the canyon. Thus, the higher the v-velocity near the bottom wall is, the larger the capacity to disperse the pollutant out of the canyon. Figure 13 shows that the v-velocity at $y = 0.1H$ is close to zero across the full extent of the canyon floor particularly in regions in which the low momentum pollution in injected. Therefore, the pollutant does not have a direct path out of the canyon but is convected towards the leeward side of the canyon by the u-velocity induced by the primary vortex. As can be observed in Figure 13, u-velocity is highest at $x = 0.5H$ and decreases gradually as the flow approaches the leeward side of the canyon and decays to very small values at $x = 0.1H$ over the full height of the canyon. As the pollutant is transported to the leeward side, the induced v-velocity of the primary vortex (increases with distance from the floor of the canyon) transports the pollutant upward. However, as can be surmised from Figure 12c, some of the pollution gets entrained into the corner eddy increasing the residence time and mean concentration in that region. To a much lesser extent, some of the SF_6 also gets trapped in the windward eddy near the canyon floor (Figure 13c)

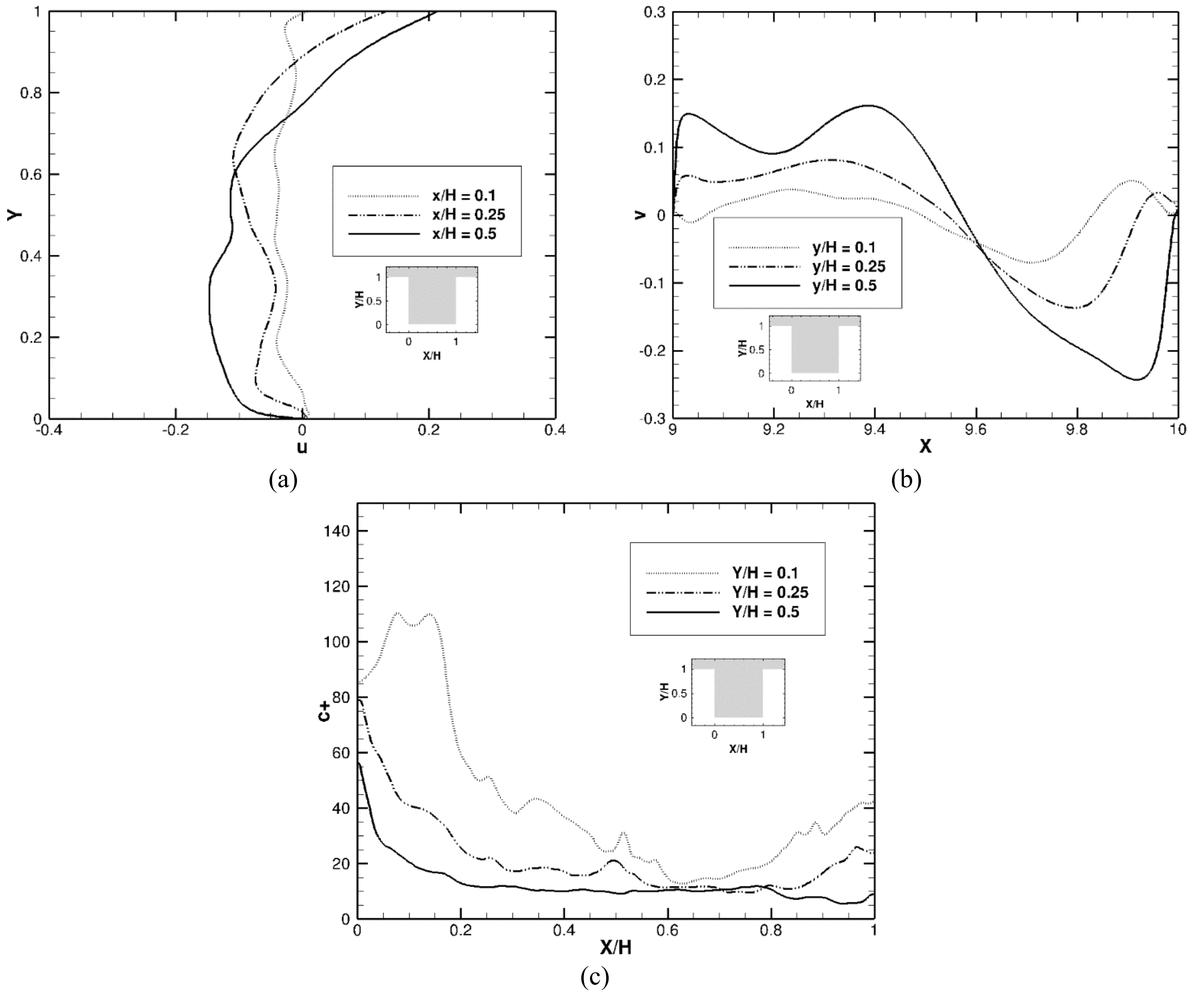

Figure 13 Velocity and concentration profiles inside the W/H = 1 canyon. (a) u(y) plotted at different x-locations in canyon; (b) v(x) plotted at different y-locations; (c) c^+ (x) plotted at different y-locations.

<u>3.6.2 Turbulent Stresses</u>

Turbulence also plays a significant role in diffusing the pollutant. What makes a street canyon problem different from the traditional lid-driven cavity flow is the presence of the externally induced turbulent fluctuations. These fluctuations are caused by the shear layer on the top of the upstream building. This phenomenon is shown as the high intensity region in the contour plot of the turbulence strength or the root-mean-square u-velocity, U_{rms} in Figure 14. The maximum Reynolds shear stress and turbulent kinetic energy are observed in the separated shear layer near its reattachment location on the top face of the building and at the location where the flow impinges on the windward side of the canyon. Inside the canyon, U_{rms} exhibits values between 0.25 to 0.4 in the center of the canyon and turbulent kinetic energy between 0.09 and 0.14, whereas turbulent shear stress magnitudes range from -0.05 to +0.04 inside the canyon.

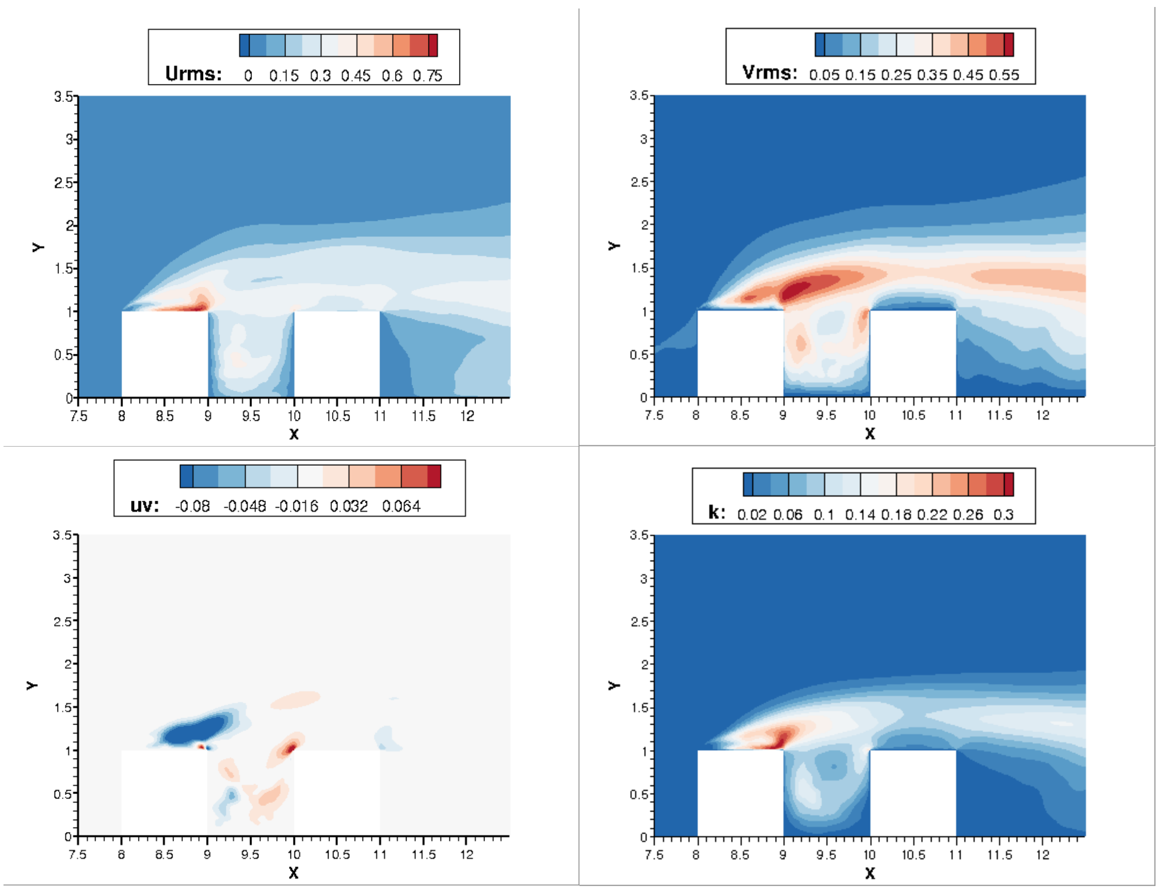

Figure 14 Contour of mean U_{rms}, V_{rms}, mean $U'V$, and turbulent kinetic energy k inside the W/H = 1 canyon.

3.6.3 Pollution Concentration

After analyzing the mean quantities, SF_6 concentration profiles at Z/H = 0 are then normalized according to the procedure discussed in Section 3.5. The contour taken at the mid-span plane (Z/H = 0) is shown previously in Figure 12c.

Figure 15 shows mean concentration profiles near the windward and leeward sides of the canyon. The horizontal bars show the root-mean-squared fluctuations of concentration ($c^+ \pm c^+_{rms}$). Overall, there is a relatively satisfactory agreement between the simulations and measurements in terms of mean values for both canyon ratios, especially in the upper region of the canyon. The same trends are obtained in the LES results of Moonen et al. [40], which over predict the mean concentration in the canyon for both walls (the insets in Figure 15) and show higher concentration near the ground for the leeward wall. A similar observation was made by Balczó et al. (2009) [35] based on a RANS simulation of the same configuration. They attributed that to the larger residence time of the pollutant in the canyon in the simulation. One major difference between the current LES and that of Moonen et al. [40] is the predicted magnitude of c^+_{rms}. In the current study, c^+_{rms} is much larger indicating large positive intermittent fluctuations in SF_6 concentration. The intermittency is representative of the large-scale unsteadiness in the canyon. The much larger magnitude in the present simulation could be a result of the two-dimensional nature of the unsteady flow structures which in the absence of three-dimensional instabilities tend to be more coherent and stronger.

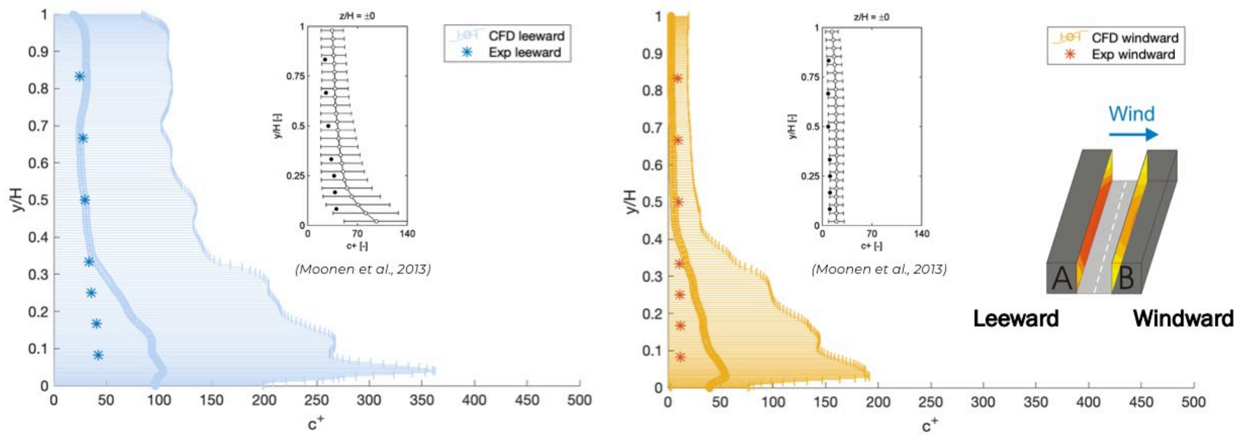

Figure 15 Profiles of computed normalized mass concentration of SF_6, c^+ at Z/H = 0 and X/H = 0.042 away from (right) the windward wall and (left) the leeward wall in comparison to the experimental data from CODASC [17]. The inset plot for W/H = 1 contains LES results of Moonen [40] (open circles) compared to experimental results obtained from CODASC (closed circles) [17]. Horizontal lines indicate root-mean-squared concentration fluctuations in the plot and the inset.

Since the impact of air quality to the public health is of interest, it is important to look at concentration relative to the pedestrians' heights. The average height of an American adult population is under 176 cm for males and 162 cm for females [57]. In this 1:150 model, the corresponding dimensionless pedestrian height would be under y = 0.1. This is a highly polluted region. The concentration peaks at y = 0.04 and 0.03 on the windward and leeward sides.

In terms of pollution fluctuation, the concentration in the near ground region could rise as high as 20 times the mean values on the windward side and 8 times on the leeward side. This high degree of fluctuation in the pollution concentration shows the importance of reproducing intermittent turbulent fluctuations, giving more insight into short term pollution exposure mitigation.

3.6.4 Overall Model Performance Evaluation and Validation

In assessing the dispersion model performance, the study utilizes the model performance evaluation method suggested by Chang and Hanna [58] and the acceptance criteria proposed for urban applications through the evaluations of the US Department's Joint Effects Model (JEM) [59]. The generic equations for performance evaluation are listed below, where C represents concentration, an overbar represents an average, and the subscripts o and p represent observed results from the experiment data and predicted results from the simulations, respectively.

FAC2, a fraction of data points that satisfy:

$$0.5 < \frac{\mathrm{C_p}}{\mathrm{C_o}} < 2 \tag{47}$$

Fractional bias:

$$\mathrm{FB} = \frac{2\left(\overline{\mathrm{C_o} - \mathrm{C_p}}\right)}{\overline{\mathrm{C_o}} + \overline{\mathrm{C_p}}} \tag{48}$$

Normalized root-mean-square error:

$$\mathrm{RNMSE} = \sqrt{\frac{\overline{\left(\mathrm{C_o} - \mathrm{C_p}\right)^2}}{\overline{\mathrm{C_o}}\,\overline{\mathrm{C_p}}}} \tag{49}$$

Geometric mean bias:

$$\mathrm{MG} = \exp\left(\overline{\ln\left(\frac{\mathrm{C_o}}{\mathrm{C_p}}\right)}\right) \tag{50}$$

Geometric variance:

$$\mathrm{VG} = \exp\left(\overline{\left(\ln\left(\frac{\mathrm{C_o}}{\mathrm{C_p}}\right)\right)^2}\right) \tag{51}$$

Pearson correlation coefficient:

$$\mathrm{R} = \frac{\overline{(\mathrm{C_o} - \overline{\mathrm{C_o}})(\mathrm{C_p} - \overline{\mathrm{C_p}})}}{\sigma_o \sigma_p} \tag{52}$$

The proposed acceptance criteria for urban applications are as follows [59]:

- $|\mathrm{FB}| \lesssim 0.67$, requiring the relative mean bias to be less than a factor of 2
- RNMSE $\lesssim 2.4$, requiring the random scatter to be $\lesssim 2.4$ times the mean
- FAC2 $\gtrsim 0.30$, requiring the fraction of $\mathrm{C_p}$ within a factor of two of $\mathrm{C_o}$ to be higher than 0.30

Since no recommended ranges for MG, VG, and R are specifically given for urban applications, the more stringent rural criteria are used:

- $0.7 \lesssim \mathrm{MG} \lesssim 1.30$
- $\mathrm{VG} \lesssim 4$
- $\mathrm{R} > 0.8$

These ranges are not meant to be exhaustive but to serve as a guideline for quality assessment [59]. In this study, the predicted data is interpolated to be comparable with the experimental data which is coarser in spatial resolution. The statistical measures of the model for both street canyon ratios are within the acceptable ranges for satisfactory model performance, as shown in Table 8. For the W/H = 1 canyon, the FAC2 value for windward concentration data is marginally within the range, suggesting high deviation on the windward side. Using unsteady RANS, Kang et al. [41] also overestimated concentrations near the windward wall.

Table 8 Statistic measures for model performance evaluation

W/H	Wall	FAC2	FB	RNMSE	MG	VG	R
1	Windward	0.29	-0.56	1.41	0.85	2.34	0.81
1	Leeward	0.86	-0.42	0.64	0.72	1.24	0.81
Recommended by Hanna & Chang [59]		≳ 0.30	[-0.67, 0.67]	≲ 2.4	[0.7,1.3]	≲ 4	≲ 0.8
Aim		1	0	0	1	1	1

According to Chang and Hanna [58], MG and VG may provide a more balanced measure of data with extreme values than FB and RNMSE. Nevertheless, both FB and MG values for W/H = 1 shows underpredictions outside of accepted range for both walls, although performing better at the leeward wall. The Pearson correlation factors, R = 0.81 also implies a strong linear relationship between the experimental and simulation results near both walls.

Similar to this study, Salim et al. [33], Moonen et al. [40], Kang et al. [41], and Merlier et al. [32] also found more deviations on the windward wall than the leeward wall. Figure 16 summarizes the evaluation statistics in comparison to those available from the previous LES studies [32], [40], [41]. These common features among predictions from different studies point to the possibility that there might be some systemic errors in the experimental measurements.

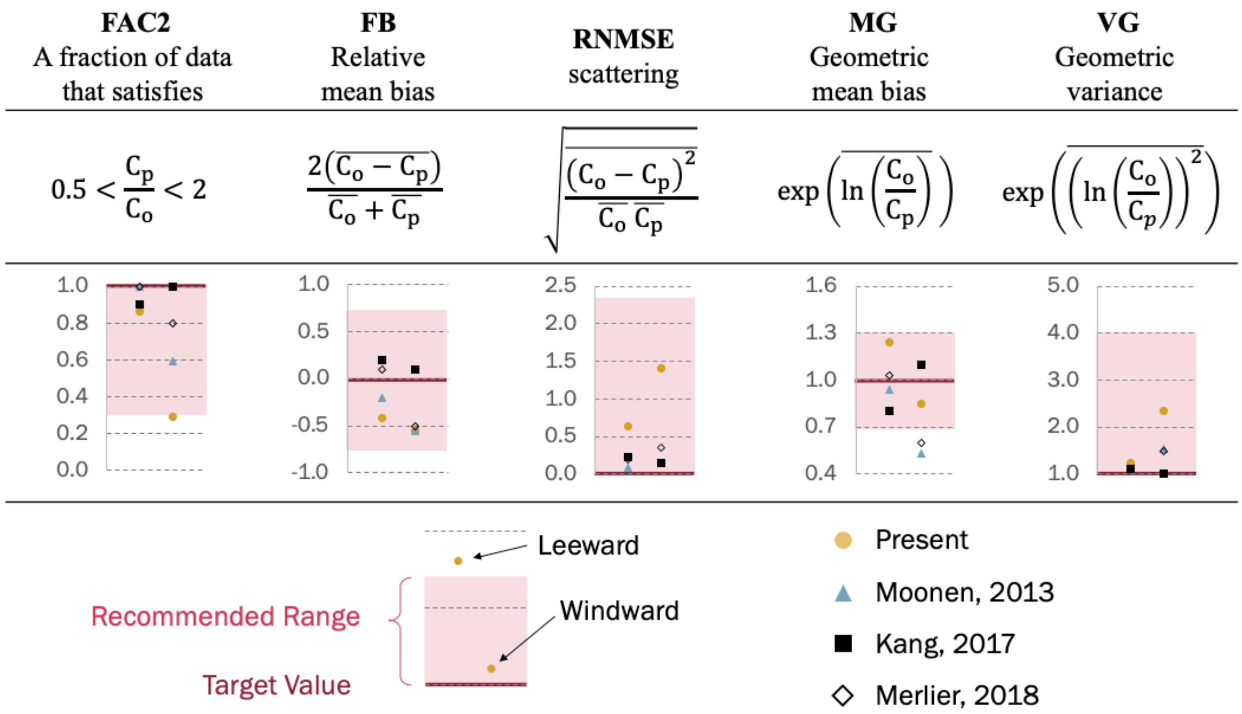

Figure 16 Comparison of performance measures from the present study, Moonen et al. [40], Kang et al. [41], and Merlier et al. [32] for W/H = 1 canyon with the leeward profile on the left and windward profile on the right.

3.7 Conclusion and Future Work

LES method is known for its ability to provide transient flow field information which could be very useful in air quality analysis in the urban environment since pedestrians are more likely to be exposed to pollution on a transient short-term basis. This method, compared to a steady method such as RANS, which has already been widely used among researchers in this field, comes at the expense of high computational cost. This study aims to reproduce the pollution dispersion measured in the wind tunnel at KIT [17] for street canyon ratios of W/H = 1 and 2 using the LES approach and reduce computational cost by simplifying the geometry while striving to preserve the mixing induced by individual jets used to model vehicle emission in the experiment.

The results are in satisfactory agreement with the experimental results without having to model the entire length of the canyon while providing a time-varying concentration of pollutant. A greater deviation in concentration prediction is found closer to the ground level, implying insufficient dispersion of the pollutant. The over-prediction has also been observed in other LES investigations. The prediction accuracy could possibly be improved by allowing three-dimensional instabilities to develop to increase turbulent diffusion. This can be accomplished by using a larger spanwise domain with a pollutant line source for large wavelength instabilities to develop, yet not modeling the full length of the canyon.

In terms of computational expense, modeling the canyon with a thin 3D model allows LES to be used without requiring a large number of cells (1-2 million compared to other studies which use up to 6.4 million cells for RANS and 70 million cells for LES [32], [36]) to model the full length of the canyon.

As stated earlier, mixing could be improved by increasing the spanwise extent of the domain which at most would increase the resolution to approximately 5 million cells. Since the discrete source model did not seem to offer much advantage, the emissions can be modeled as continuous line sources, thus grid size and computational cost could be further reduced. Once a better model has been established, future work may consider modeling vegetation and investigate different canyon ratios and more complex building configurations.

CHAPTER 4: EFFECTS OF LEAF HAIR GEOMETRY ON AEROSOL DEPOSITION

4.1 Introduction and Literature Review

Due to the rising concern regarding urban air pollution as mentioned in Chapter 1, different methods of mitigations have been considered. Since urban green space, especially parks, is often thought of as "lungs of the city", a metaphor used by the famous landscape architecture, Frederick Law Olmsted, who oversaw the construction of Central Park [60], many cities are including street vegetation, such as trees, green facades and urban parks, as part of strategies to reduce the impact of urban air pollution. Generally, emissions can be removed from the air by plants through chemical reactions and surface deposition. The deposition of particulate matter on the leaf surface is of interest in this thesis.

4.1.1 Deposition

Aerosols are removed from the atmosphere by two mechanisms: dry deposition and wet deposition. Dry deposition occurs at the surface through sedimentation for coarse particles (2.5 μm < D_p^* < 10 μm) and through turbulent transport impaction for fine particles (D_p^* < 2.5 μm), whereas wet deposition involves incorporation into cloud or rain droplets in the process of precipitation. The coarse particles are also referred to as PM10 and fine particles as PM2.5.

Close to pollution sources, dry particulate deposition is also considered more important than wet deposition [61], [62]. Therefore, this study puts an emphasis on the dry deposition on the leaf surface. Governing factors of dry deposition include the atmospheric turbulence level, properties and physical characteristics of depositing particles, and the nature of the surface where the particles interact with [7].

Fine aerosol deposition onto vegetation is affected both by environmental factors including wind speed and aerosol concentration and by the biophysical characteristics of the plant such as plant density and leaf surface area index. Due to the importance of urban vegetation as an approach to reduce pollution risk, the effects of leaf characteristics such as shape, porosity, leaf hair (or trichome), wax content as well as wind speed and air concentrations have been studied either in the field or through wind tunnel measurements [63]–[67]. Over a range of 1 to 10 m/s, different studies measured higher deposition at greater velocity [67], [68]. Regarding the effect of particle sizes, Ottelé et al. [69] found lower deposition for coarse particles than the finer ones. Investigating particles of $D_p^* = 3 - 180$ μm, Weber et al. [70] also observed a similar trend where the 3–10 μm particles deposited more frequently than the larger ones.

Furthermore, Kardel et al. [71], Saebo et al. [63], and Speak et al. [66] observed a positive correlation between particle deposition and hairiness. The correlation is also confirmed by Weber et al. [70] and Mitchell et al. [72] for coarse particles (3–180 μm and >10 μm, respectively). Contrarily, Perini et al.[73] found less accumulation when stellate-like hairs are present.

Due to the complex dependence of deposition rate on different variables such as particle size and vegetation characteristics, parameterization with experiment or field data poses many challenges in this field of study [74], [75]. Leaf samples used in the experiments often have mixed traits, and studies are often limited to certain species. Therefore, computational methods, which allow different factors to be studied independently, would contribute significantly to parameterizing the effects and give more clarity to the results.

This study focuses specifically on the impacts of leaf hair traits (i.e. diameter, diameter to height ratio, and density), particle size, and wind speed on deposition on the leaf surface. Emissions from vegetation and chemical reactions between plants and pollutions are excluded from this study. A brief overview of aerosol deposition and trichomes is included in the following section. Since the density of aerosols typically ranges from 1~2 g/cm^3, the density of 1.5 g/cm^3 (1500 kg/m^3) is used as a representative value.

4.1.1.1 Dry Deposition and Deposition Velocity

The process of dry deposition for particles can be represented by three primary phenomena [76]: (1) aerodynamic transport of particles in the surface layer; (2) diffusion across the quasi-laminar sublayer to the surface, dominantly through Brownian transport; and (3) transfer to the surface.

Particles could be removed from the quasi-laminar sublayer due to changes in the direction of the mean air flow by inception, which occurs when particles collide with obstacle while passing sufficiently close to it; and by impaction which occurs when particles leave the streamline and the inertia derived from the mean flow carries them to the surface [7].

Deposition can be quantified and normalized using the deposition velocity, U^*_{dep} which is a proportionality constant between the vertical dry deposition flux (or the amount of particle removal per unit area per unit time), F^* and the pollutant concentration per unit volume, C^* at a certain height, z^* above the ground. This relationship assumes height dependency and a direct correlation between particle concentration and deposition. Since this study investigates deposition close to the surface, the deposition flux is assumed constant. Therefore, the deposition velocity can be expressed as:

$$U^*_{dep} = \frac{F^*}{C^*} \tag{53}$$

Even though deposition velocity has been widely studied and measured, the values vary significantly across species even for the same particle diameter [74]. Saebo et al. [63] found the variation in the deposition velocity across 40 species to be up to 15 fold.

4.1.2 Plant Surface Characteristics

A leaf surface may be generally smooth, hairy, waxy or any combinations of these features. A smooth leaf has neither leaf hair nor wax on the surface and will be used as the base case for this study. Trichomes or leaf hairs are outgrowths protruding from the leaf surface either on the upper, lower or both.

Since there is no universally accepted terminology in leaf factor classification, the author follows the categories defined in Figure 17 by Voigt et al. [77]. Trichomes can be classified into glandular and non-glandular, and a leaf often contains a mixture of both types. For simplicity of the study, the trichomes modeled are non-glandular, non-branched, smooth, circular in shape, perpendicular to the leaf surface, and regularly dispersed. The hair is also uniform in diameter.

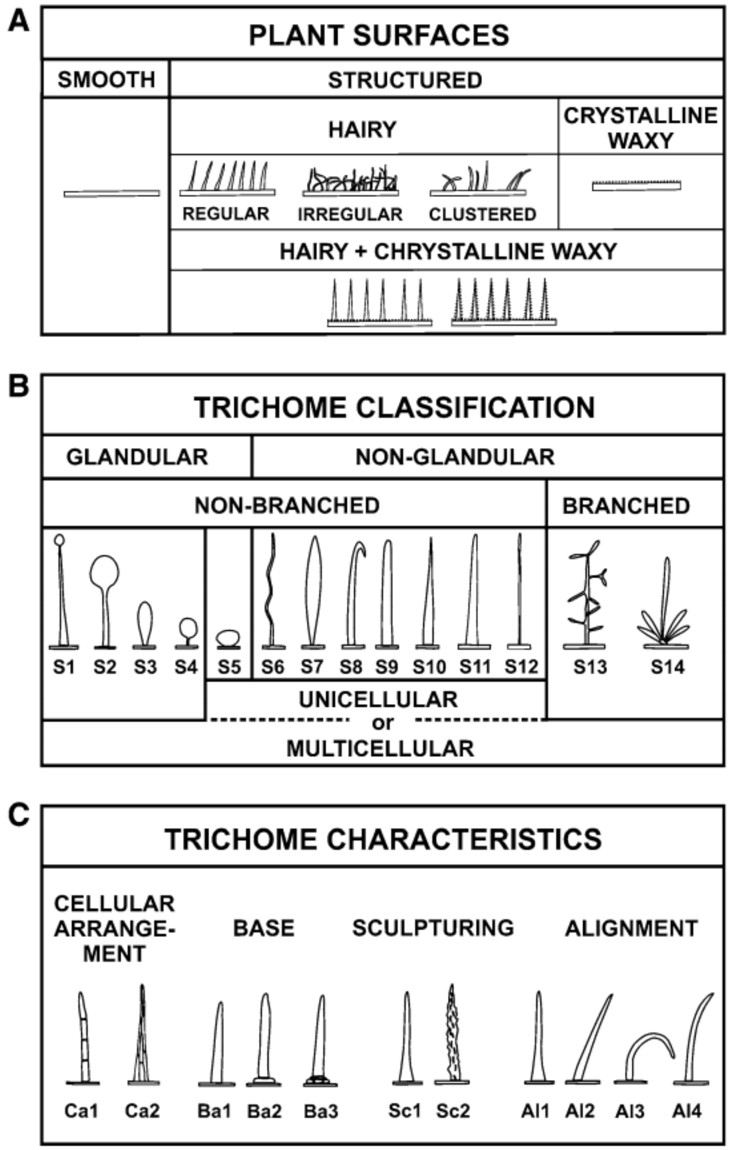

Figure 17 (A and B) Diagrams showing plant surfaces and trichome types found on the tested leaves based on the trichome arrangement, cellular arrangement in the single trichome and its shape. (C) Diagram of the trichome characteristics found on the tested leaf surfaces based on the trichome alignment, surface texture, base structure and cellular arrangement. [77]

To study the effects of leaf hair characteristics: trichome diameter (5 and 20 μm), height-to-diameter ratio (H/D = 20 and 30), and density (5 and 15 trichomes per mm^2) are chosen as physical parameters at a mean velocity of 1 m/s. A summary of investigated cases with different leaf hair characteristics is shown in Table 9. Measurements of Mediterranean gall oaks' acicular trichomes by Tschan and Denk [78] are used as guidelines in establishing the range of values for the leaf hair traits to ensure realistic geometry representations. Across the seven species investigated, an acicular trichome found ranges from 8 – 26 μm in diameter and 55 – 853 μm in height (corresponding height-to-diameter ratio between 6 and 47) [78]. The density is obtained from another study conducted by Moradi et al., [79] where the trichome density ranges from 7 – 18 trichomes per mm^2 of the upper leaf surface of three Mediterranean oak species.

Table 9 Summary of cases with different trichome characteristics. Particle diameter is 0.3 μm for all listed cases. The Reynolds number in respect to the leaf hair is defined as $\mathrm{Re_{hair}} = \rho^*_{air} U^*_\infty D^*_{hair} / \mu^*_{air}$.

Trichome diameter, D^*_{hair} (μm)	5			20			
$\mathrm{Re_{hair}}$ at $U^*_\infty = 1$ m/s	0.32			1.28			
Trichome height, H^*_{hair} (μm)	100		150	400		600	
Height to diameter ratio (H^*_{hair}/D^*_{hair})	20		30	20		30	
Trichome density (per mm^2)	5	15	15	5	15	5	15
Spacing to diameter ratio (S^*_{hair}/D^*_{hair})	89.44	51.64	51.64	22.36	12.91	22.36	12.91
Case Name	LH_d5_hd20_den5	LH_d5_hd20_den15	LH_d5_hd30_den15	LH_d20_hd20_den5	LH_d20_hd20_den15	LH_d20_hd30_den5	LH_d20_hd30_den15

Each case in Table 9 named according to the trichome diameter in μm "d", H/D ratio "hd", and the trichome density in mm^{-2} "den", each followed by the value. For example, the case, where the trichomes are 20 μm in diameter with the H/D ratio of 20 and the density of 5 trichomes per mm^2, is named "LH_d20_hd20_den5".

In order to investigate the effects of mean velocity and particle diameter on pollution removal, the geometry of the case "LH_d20_hd20_den5" is selected. As summarized in Table 10, in addition to 1 m/s, the wind speed of 3 m/s is studied. At the mean wind speed of 1 m/s, the effects of particle diameters (0.3 and 1 μm) are also examined. Finally, a base case with no leaf hairs is calculated using the same geometry (same domain size) to establish a reference state for particle deposition as well.

Table 10 Different flow conditions for LH_d20_hd20_den5 geometry.

<table>
<tr><th>Case Name</th><th>Particle diameter, D_p^* (μm)</th><th>Mean velocity, $\overline{V}^*$ (m/s)</th><th>Coresponding Re_{hair}</th></tr>
<tr><td>LH_d20_hd20_den5_u1_1um</td><td>1.0</td><td rowspan="3">1</td><td rowspan="3">1.28</td></tr>
<tr><td>LH_d20_hd20_den5_u1_plain</td><td rowspan="3">0.3</td></tr>
<tr><td>LH_d20_hd20_den5_u1</td></tr>
<tr><td>LH_d20_hd20_den5_u3</td><td>3</td><td>3.83</td></tr>
</table>

The Stokes' numbers corresponding to different particle diameters and wind speeds are given in Table 11. The Stokes' numbers at the different mean velocities and for the two particle diameters of interest are all lower than 5×10^{-3}, indicating that in the absence of any other mechanisms, the particle will tend to follow streamlines, or in other words, the particle time scale is much smaller than the fluid flow time scale. Moreover, at the maximum PM2.5 concentration of 500 μg/m^3, according to the US Environmental Protection Agency's air quality standard [80], the flow is still considered sparse and the effects of particles on the flow field are negligible. Therefore, one-way coupling is sufficient in this study.

Table 11 Investigated diameters of aerosol and their corresponding Stokes' numbers (as defined by Eqn. (29))

Particle diameter, D_p^* (μm)	0.3	0.3	1
Mean velocity, $\overline{V}^*$ (m/s)	1	3	1
Stk	4.21×10^{-4}	1.26×10^{-3}	4.67×10^{-3}

4.2 Computational Model

4.2.1 Computational Domain and Grid

The computations are performed under the fully-developed assumption in a channel with an infinite array of trichomes. This is achieved by assuming periodicity in the x- and y-directions. To conduct a parametric study of leaf hair traits, the leaf hairs or trichomes are assumed to be uniformly circular and equally distributed as illustrated in Figure 18. Each trichome is D_{hair} in diameter and H_{hair} in height. Four trichomes are included in the domain to ensure that fluid interactions are captured and not lost due to periodicity. The leaf hairs are S_{hair} apart from each other in both the streamwise and spanwise directions. The grid resolution goes from $\Delta x = 0.05$, $\Delta y = 0.05$, $\Delta z = 0.05$ near the leaf or trichome surface to $\Delta x = 5$, $\Delta y = 5$, $\Delta z = 3.75$ in the far field. The grids consist of 747,000 cells and 607,104 cells for the 5 μm and 20 μm trichomes, respectively.

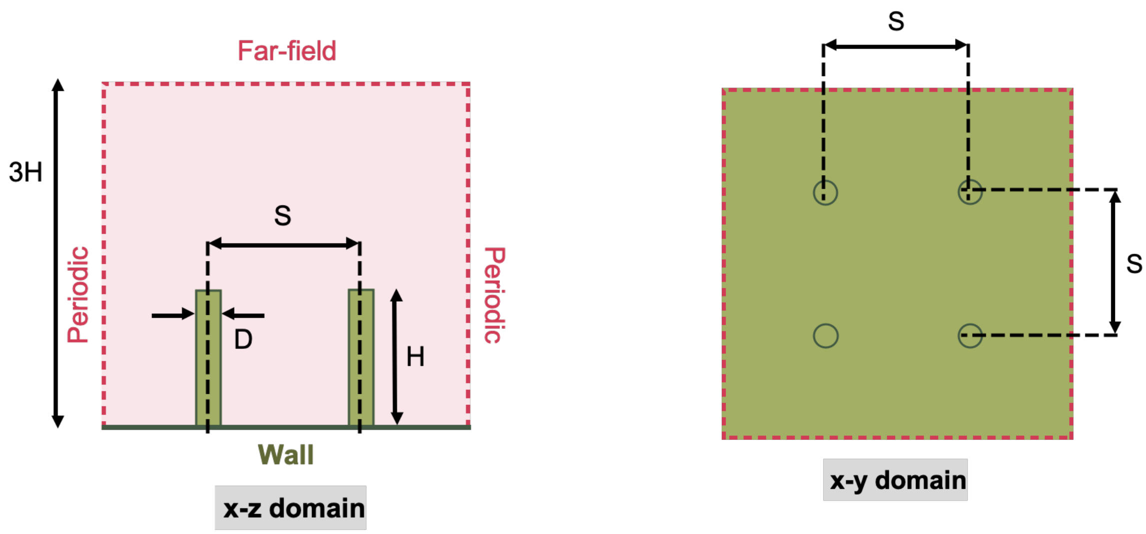

(a) (b)

Figure 18 Schematic diagrams of the computational domain: (a) front view with boundary conditions (x-z plane), and (b) top view (x-y plane). Drawings are not to-scale.

A mesh was generated for each geometrical arrangement with hairs of the same diameter having the same computational grid distribution. The domain height is three times the height of the hairs to ensure that there is a minimal influence of the boundary on the flow field and particle transport in the vicinity of the trichomes. Figure 19 and Figure 20 show the computational mesh of the 5 μm diameter trichomes. Unstructured block topology with structured non-orthogonal grids are used. The grid dimensions are summarized in Appendix C.

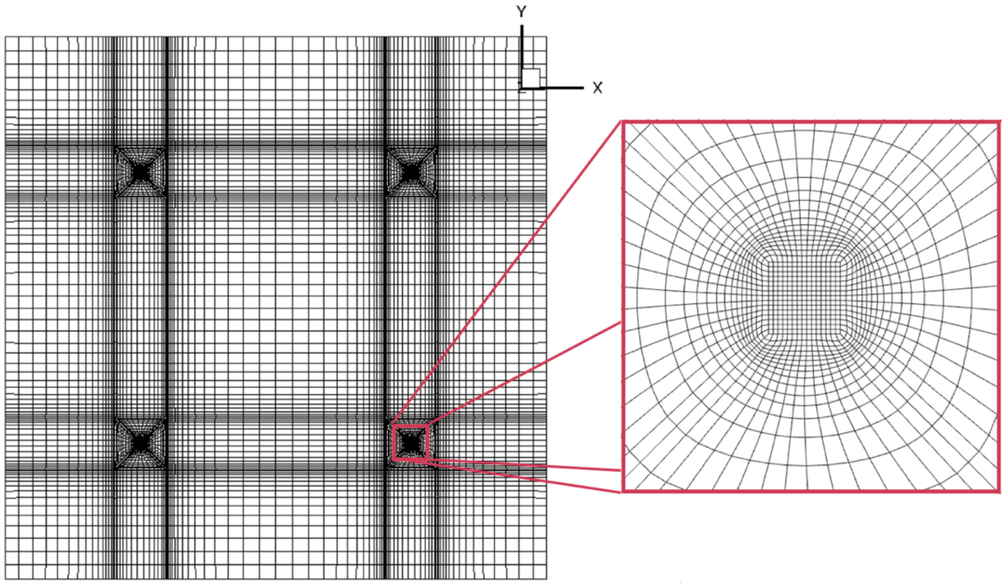

Figure 19 Top view (x-y) of the computational mesh for 5 μm diameter trichomes; the red square shows the enlarged view of cell distribution along the axis of the trichome.

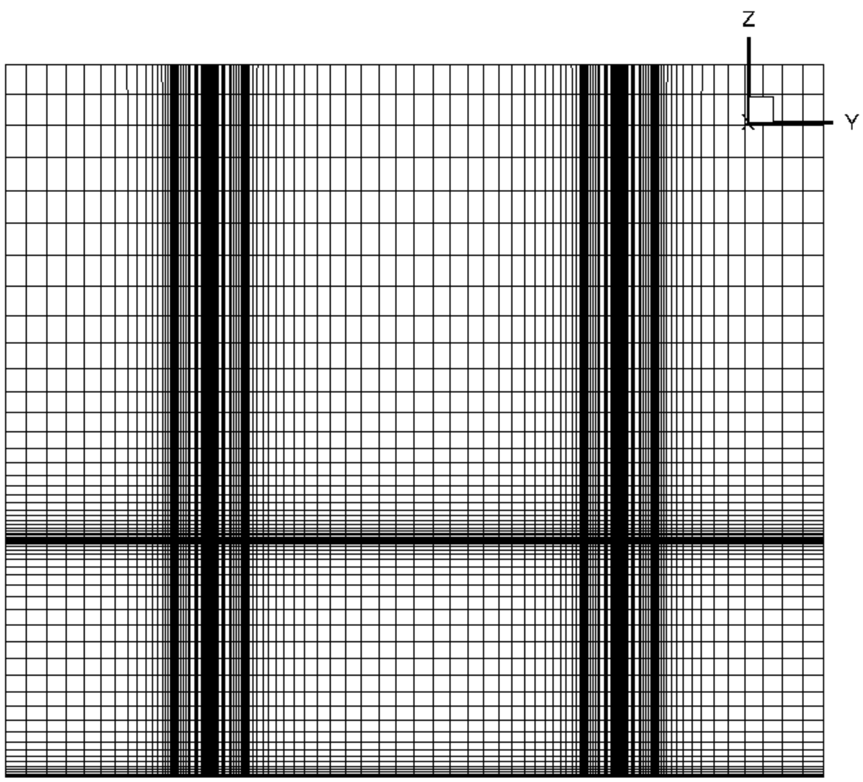

Figure 20 Front view (y-z) of the computational mesh for 5 μm diameter trichomes. The domain height is three times the trichome's height.

4.2.2 Boundary Conditions

Periodic boundary conditions are applied along the streamwise and spanwise directions with the flow going through the y-z planes in the x-direction as illustrated in Figure 21. More about the periodic boundary conditions can be found in Section 2.1.3. With the domain height of $3H_{hair}$, the boundary condition at the top boundary is given by $\left(w = 0; \frac{\partial u}{\partial z} = \frac{\partial v}{\partial z} = 0\right)$. The leaf surface and leaf hairs are considered as walls where no-penetration and no-slip conditions are applied.

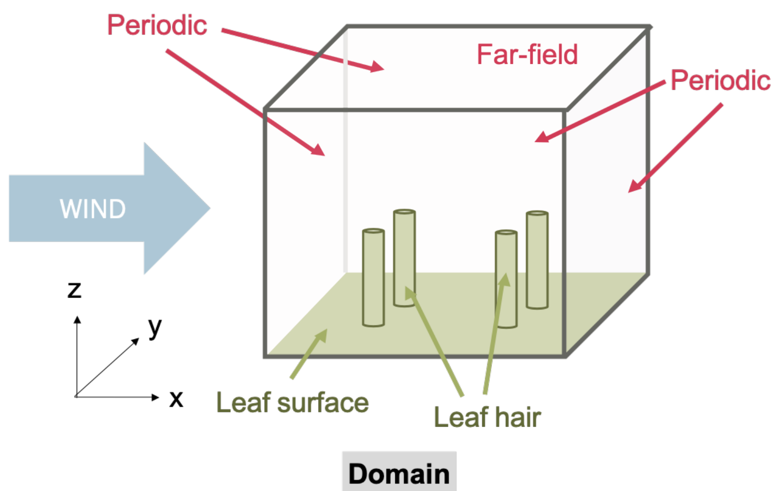

Figure 21 Schematic diagram of the computation domain with boundary conditions.

4.2.3 Calculation Procedure

Once a fully-developed flow is established (as discussed in Section 2.1.3), the flow computation is deactivated (since particles do not affect the velocity field), and particles are distributed in the domain with initial velocity equal to the fluid velocity at that location. The number of particles injected is selected so that the initial particle concentration of about 10,600 particles per mm^3 for all geometries. After the particles are injected, the particle field is allowed to develop and randomize the spatial distribution of particles. During this development period, particle-wall collisions are modeled using a fully-elastic hard sphere model by setting the coefficient of restitution (COR) to be unity.

Because of the small size of the particles and very low velocities, it is assumed that a particle in collision with a surface will not able to overcome the attractive van Der Waals adhesion forces, stick to the surface and will be considered as deposited. This is implemented by setting the COR = 0 after the initialization period. Once a particle sticks to the surface it is counted as a deposited particle and removed from the computation domain. The deposition simulations are run for 1 s which corresponds to between 1×10^7 to 2.25×10^8 simulation time steps (4,000 to 36,300 CPU hours). The reference properties of air and the aerosols used in these simulations are tabulated in Table 12. The hair diameter is used as the reference length, L^*_{ref} and the friction velocity, u^*_τ as the reference velocity. These values are given in Appendix C.

Table 12 Reference values (carrier phase properties) and aerosol properties

Pressure, P^*_{ref} (Pa)	101,000
Temperature, T^*_{ref} (K)	300
Density, ρ^*_{ref} (kg/m^3)	1.177
Dynamic viscosity, μ^*_{ref} (kg/ms)	1.846×10^{-5}
Molecular weight, M^*_{ref} (kg/kmol)	28.97
Particle density, ρ^*_p (kg/m^3)	1500
Numerical time step for $D^*_p = 0.3$ μm (-)	5.0×10^{-5}
Numerical time step for $D^*_p = 1.0$ μm (-)	1.5×10^{-4}

4.2.3 Method for Data Analysis

Unlike most experimental studies in the field and in wind tunnels that include a large computational domain, the present study focusses on a region very close to the leaf surface of the order of less than 2 mm in height. In spite of this difference, Eqn. (53) is adapted to the conditions of the current simulations. After the deposition for $t^* = 1$ s is complete, the deposition velocity for each case is calculated for analysis using Eqn. (53). The flux and concentration used in Eqn. (53) can be computed as follows

$$F^* = \frac{N_{dep} m_p^*}{A_{tot}^* t^*} \tag{54}$$

$$C^* = \frac{N_{tot} m_p^*}{V_{tot}^*} \tag{55}$$

, where: N_{dep} = number of particles deposited

A_{tot}^* = total area

N_{tot} = total number of particles in domain

V_{tot}^* = total volume

Because of the periodic boundary conditions in the flow direction, particles that exit the domain, reenter the domain again. Thus, the total area and volume traveled by the particles are estimated from the total distance traveled with the mean velocity during the simulated time $t^* = 1$ s.

4.3 Results and Analysis

The steady state flows and particle deposition under different trichome, flow, and particle properties will be presented and discussed in the following sections. The leaf pollution removal capacity will be given in terms of deposition velocity and compared to published works.

4.3.1 Fully-developed Flow

The fully-developed mean velocities, $\overline{V}^*$ is estimated from the flowrate and frontal area where the flow travels through, and the velocities in all cases are within 4.3% of the desired values. Since the particle dynamics is simulated using the one-way coupled model, in addition to the Brownian motion that primarily influences deposition, particle motions are highly sensitive to the flow field which could lead to deposition through impaction and inception [7]. This section will go over the fully developed flow fields and how they could influence pollution removal.

4.3.1.1 Primary flow

Shown in Figure 22 are contours of streamwise velocity over the leaf with 20 μm and 5 μm diameter trichomes of different height and density. Because of the low Reynolds number, in all cases, the trichomes are embedded in the viscous boundary layer that forms on the leaf surface. As the density increases from 5 mm^{-2} to 15 mm^{-2}, the flow has less access to space between trichomes. Thus, the velocity or mass flow defect inside the trichome array increases with trichome density. A similar observation can be made as H/D ratio increases from 20 to 30. Thus, high density tall and thin trichomes together will exhibit high resistance to flow within the trichome array and most of the mass flow will take place on the outside.

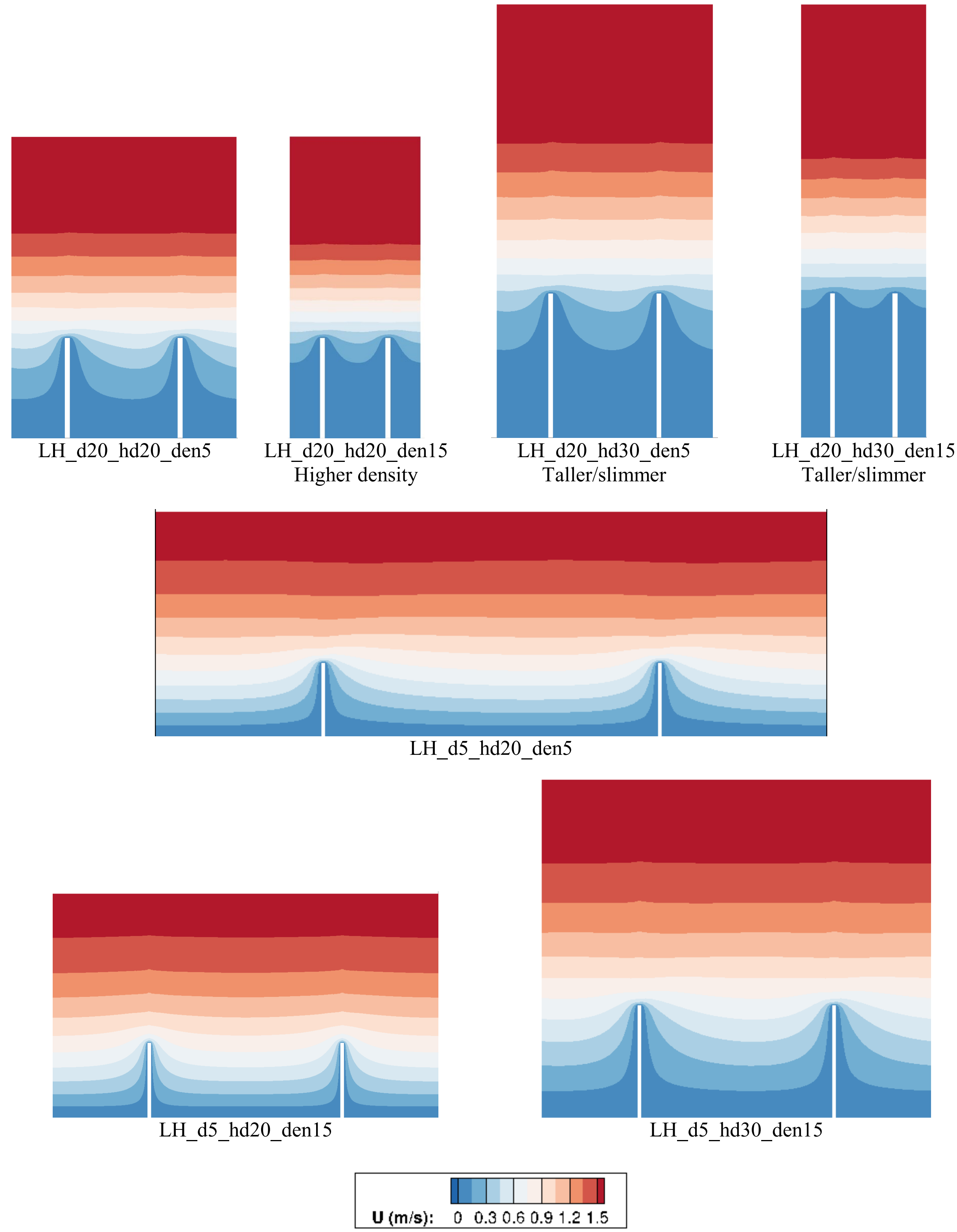

Figure 22 Velocity contour of the streamwise velocity

The velocity profiles in the wake of each trichome midway between two rows are shown in Figure 23, where the height of each trichome is at Z/H = 1. Both actual and normalized (by u_{max}) velocity profiles are shown in (a) and (b), respectively. As the trichome density and H/D increase the velocity defect in the trichome array increases and consequently the outer flow accelerates more to maintain a constant mean velocity of 1 m/s over the different cases. Between density and H/D, trichome density has a noticeably larger effect on the flow field. As the trichomes become smaller and sparser (represented by dashed lines), the u-velocity profile approaches that of the plain surface. Comparing the normalized velocity profiles at wind speeds of 1 and 3 m/s in Figure 24 confirm that the normalized profiles are almost identical for the same trichome geometry.

(a)

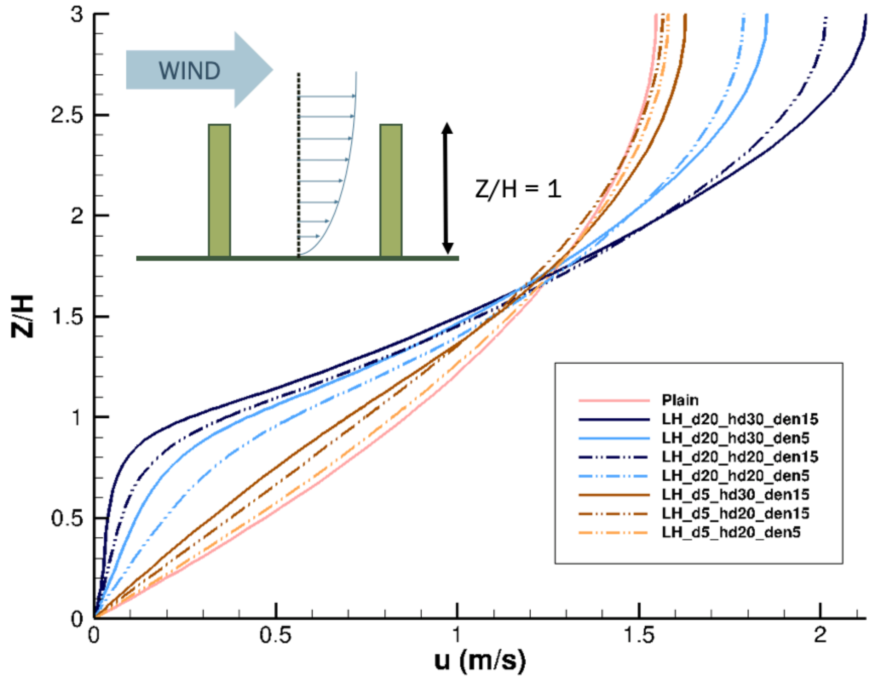

(b)

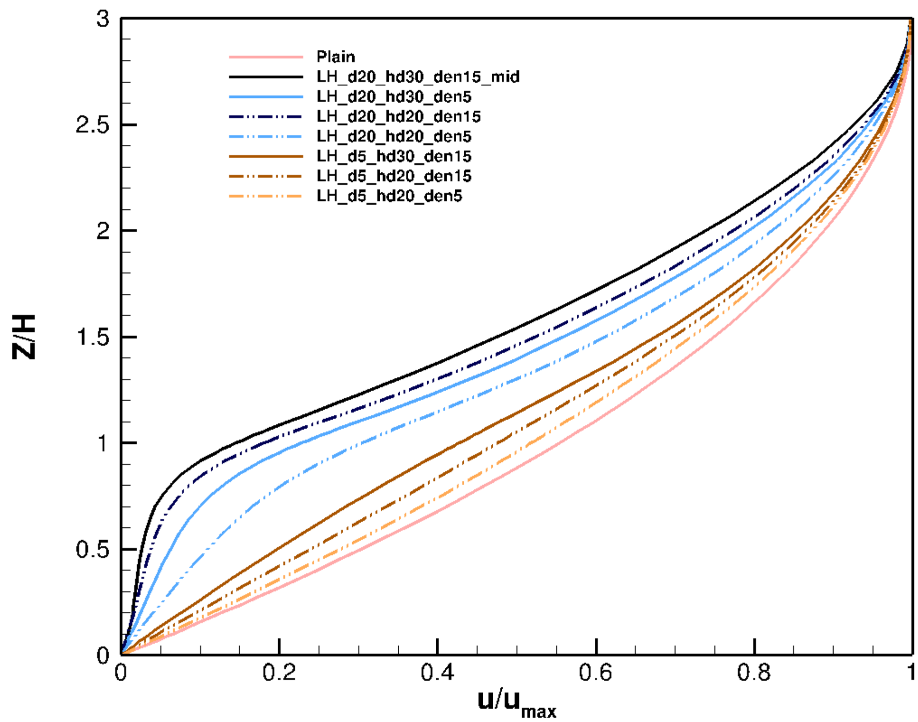

Figure 23 U-velocity profile in-line with and midway between trichomes for different geometries. (a) shows dimensional comparison and (b) shows normalized profiles.

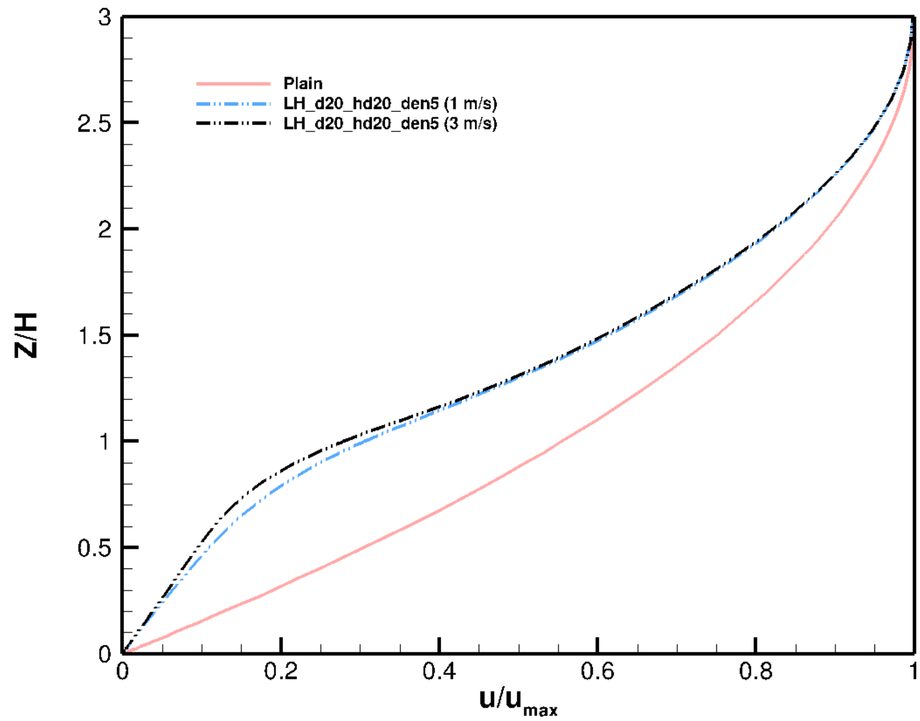

Figure 24 Normalized u-velocity profile between and in-line with trichomes for the mean velocity of 1 and 3 m/s and the smooth leaf cases.

Figure 25 shows the contours of v-velocity at different heights (z) and the associated planar streamline patterns. As the flow approaches the trichome it generates both y-directional and z-directional velocity components which are strongest at the tip of the hair. As the flow navigates around the trichome it is deflected to either side generating y- directional cross-stream velocities. Because of the highly viscous flow, the presence of the trichome is felt over the full pitch of the trichome. A vertical z-directional component of velocity is also generated by the presence of the trichome. The perturbation is strongest at the tip as the viscous fluid flows over it. While the perturbation in v-velocity is felt over the full length of the trichome, the z-component is mostly localized at the tip. Figure 26 offers further insight into the z-directional velocity for different trichome geometries. It is noted that the smaller the H/D ratio, the w-velocity generated at the tip is stronger. A similar observation is made for the trichome density –

a less dense trichome arrangement leads to larger w-velocity magnitudes. It is also observed that counter-velocities are set up in the array on the windward and leeward sides of the trichome in response to the perturbation at the tip.

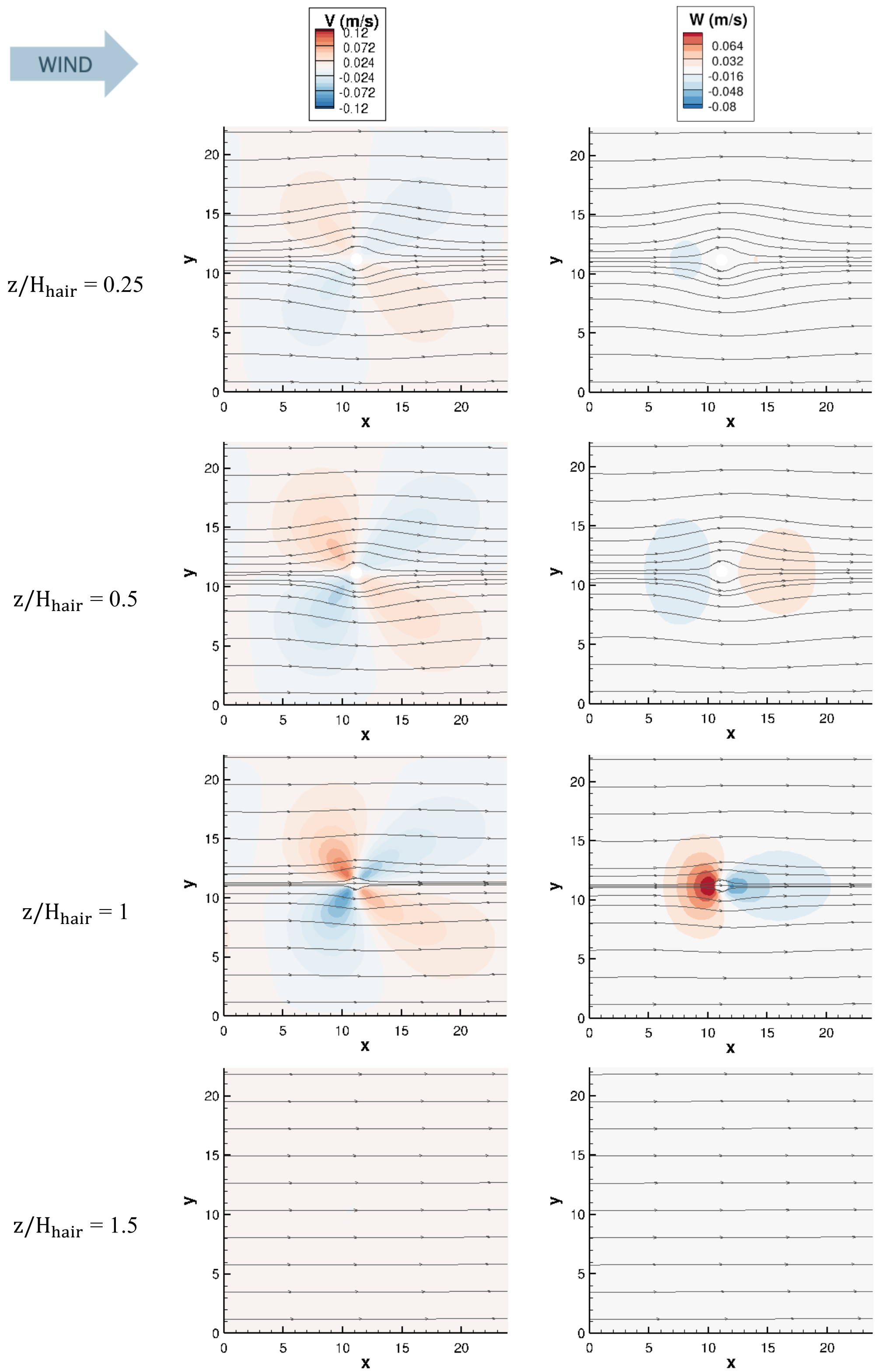

Figure 25 Contours of (left) v- and (right) w-velocities at different z/H_{hair} (LH_d20_hd20_den5 at 1 m/s). These plots show only a quarter of the entire computational domain or a single pitch in the stream and span surrounding a trichome.

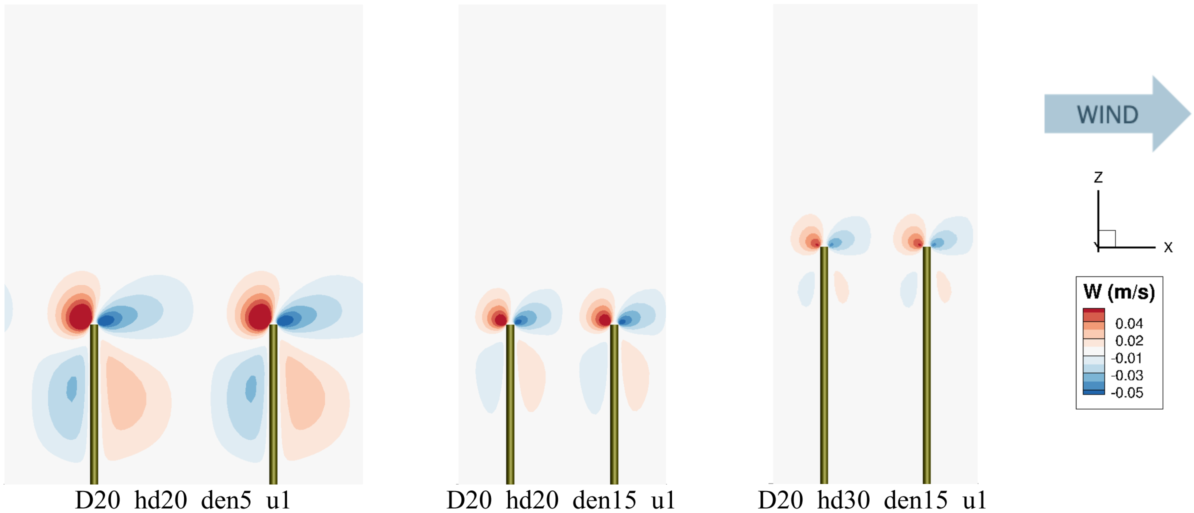

Figure 26 Contour of w-velocity

4.3.2 Particle Transport

The potentially important fluid forces acting on a particle that influence its trajectory are given in Appendix B. Typically, the relative importance of these forces depends on the flow conditions and the relative properties of particle and fluid. Instead of including all forces in the calculations, an initial study was conducted on the magnitudes of these forces for the relevant particle diameter of $D_p^* = 0.3$ μm at $\overline{V}^* = 1$ and 3 m/s and for the particle diameter of $D_p^* = 1$ μm at $\overline{V}^* = 1$ m/s. For the purpose of this analysis, all forces are shown in Equation (24) were calculated and included in the particle simulations for 10 non-dimensional time. The magnitudes of forces for all three cases are plotted as a function of non-dimensional time in Figure 27. For all particle diameters, Brownian and drag forces dominate, up to two orders of magnitude higher than other forces. Moreover, it is evident also that the Brownian force is the most dominant. From the above analysis it can be concluded that once particles are transported deep into the trichome layer, their deposition is mostly governed by near-surface Brownian diffusion [81].

Therefore, Equation (24) can be reduced to Equation (25), allowing a reduction in computational cost.

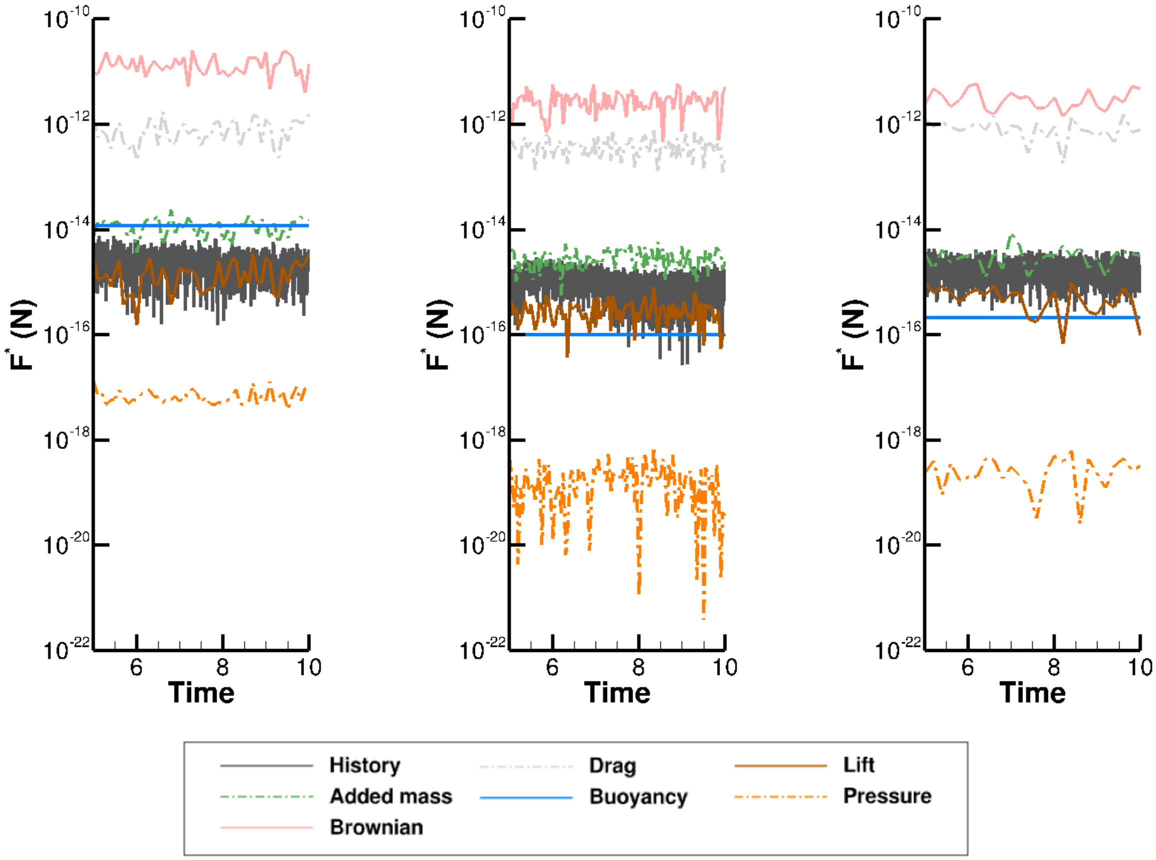

(a) 1 um; 1 m/s (b) 0.3 um; 1 m/s (c) 0.3 um; 3 m/s

Figure 27 The magnitude of different forces acting a (a) 1 μm and (b) 0.3 μm particle at the wind speed of 1 m/s (c) and of 3 m/s.

4.3.3 Deposition

Some representative deposition patterns for 20 μm diameter trichomes, H/D=20, packed at a density of 5 mm^{-2} are shown in Figure 28. There is no noticeable pattern in deposition formation on the leaf surface. On the other hand, most deposition occurring on the trichome is on the windward side. Along the height of the hairs, a significant number of particles deposit on the between z = 12-14 (Figure 28a), which corresponds to Z/H = 0.6-0.7. The deposition pattern is further elaborated on in Figure 29 by plotting the distribution histogram which shows maximum deposition between z/H_{hair} = 0.6 to 0.7 for the LH_d20_hd20_den5 case. However, as the trichome H/D increases from 20 to 30 and the density increases from 5 mm^{-2} to 15 mm^{-2} (LH_d20_hd30_den15) in Figure 29b, the deposition is more uniform over the full length of the trichome. This higher accumulation region between z/H_{hair} = 0.6 to 0.7 for the LH_d20_hd20_den5 case could be directly correlated to the w-velocity field. Figure 29c shows that the w-velocity reaches a maximum negative value followed by a rapid change in sign in this region. Whereas the w-velocity is more uniform and of much smaller magnitude for the LH_d20_hd30_den15 case, resulting in more the uniform deposition.

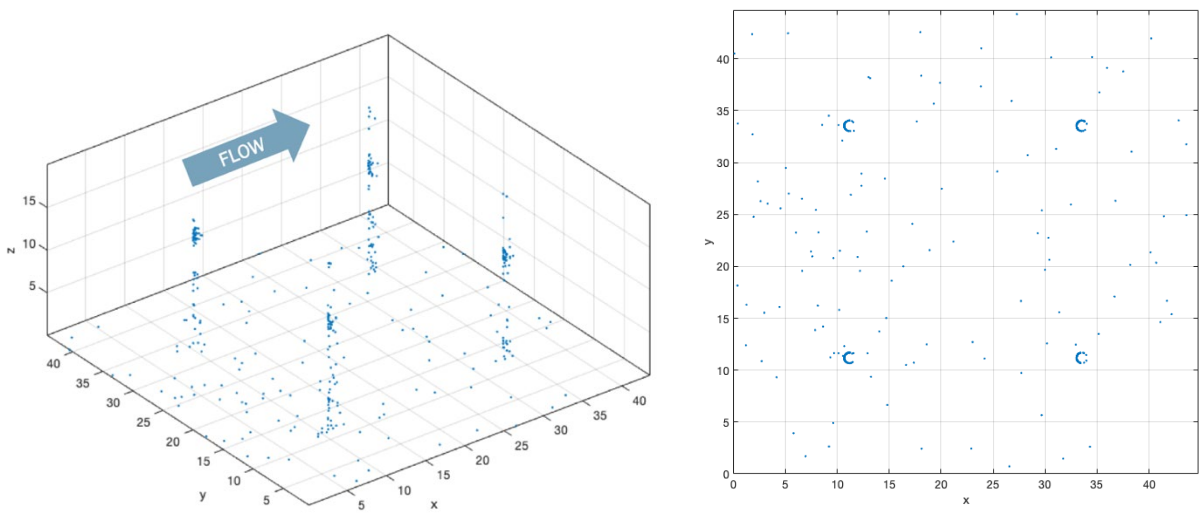

(a) (b)

Figure 28 Location of deposition for LH_d20_hd20_den5. (a) shows the xyz view and (b) shows top view.

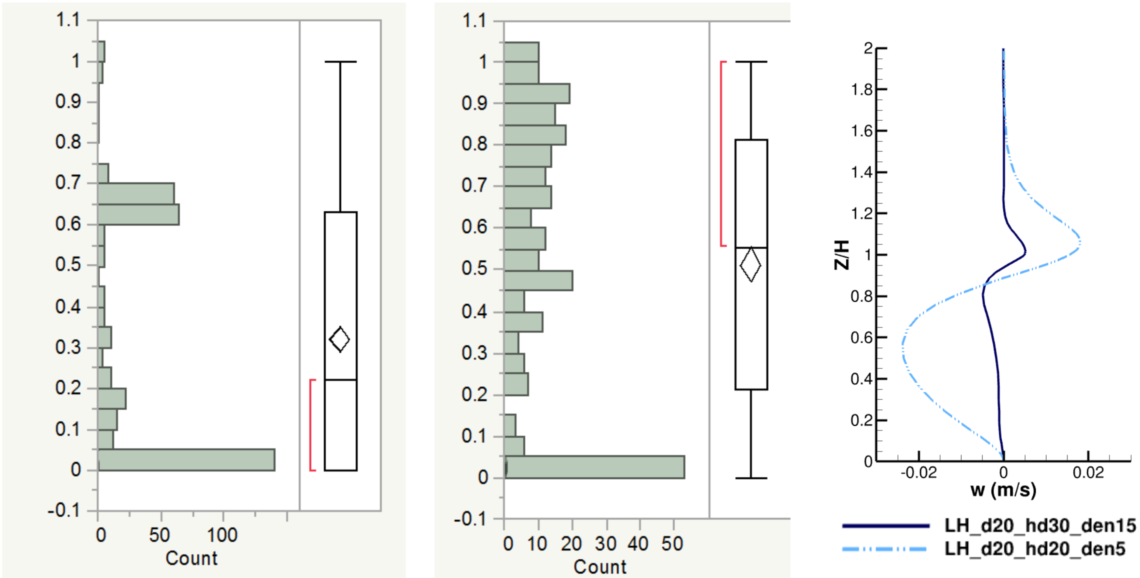

LH_d20_hd20_den5 (a) | LH_d20_hd30_den15 (b) | (c)

Figure 29 Deposition distribution along the height of trichomes for (a) LH_d20_hd20_den5 and (b) LH_d20_hd30_den15. (c) shows the in-line w-velocity profile at a distance of $5D_{hair}$ from the front of the trichome.

All calculated deposition velocities based on Eqn. (53) are tabulated in Table 13 along with percentage removal by trichomes. Deposition velocity is lowest for 5 μm diameter trichomes, H/D=20, packed at 5 mm^{-2}, whereas maximum deposition happens for 20 μm diameter trichomes, H/D = 20, packed at a density of 15 mm^{-2}. The trends are discussed in more detail in the following sections.

Table 13 Summary of deposition velocity for each case

Case Name	D_p^* (μm)	$\overline{V}^*$ (m/s)	V_{dep}^* (cm/h)	% deposition on Trichomes
LH_d5_hd20_den5	0.3	1	6.12	23%
LH_d5_hd20_den15			9.14	46%
LH_d5_hd30_den15			15.44	57%
LH_d20_hd20_den5			16.43	66.4%
LH_d20_hd20_den15			42.87	77.4%
LH_d20_hd30_den5			17.79	80.8%
LH_d20_hd30_den15			32.76	81.0%
Plain			10.83	N/A
LH_d20_hd20_den5_u3		3	19.53	63.9%
LH_d20_hd20_den5_dp1um_u1	1	1	12.23	86.1%

4.3.3.1 Effects of trichome morphology on PM0.3 deposition

The different trichome characteristics on the deposition of 0.3 μm particles at the $\overline{V}^* = 1$ m/s are studied. Figure 30 plots the effect of H/D for thin sparse trichomes (d5 den = 5) and on thicker sparse and dense configurations (d20 den = 5 & d20 den = 15). For both H/D = 20 and 30, the thin 5 μm diameter trichomes are the least effective whereas the thick 20 μm diameter trichomes are the most effective. There is about a 70% increase in deposition velocity when the height increases from H/D = 20 to 30 for the 5 μm dense trichomes (15 mm^{-2}) which is approximately proportional to the increase in the frontal area. At the lower trichome density of 5 mm^{-2}, there is a slight increase for the sparse 20 μm trichomes probably because the flow field is not influenced by a change in height due to the already sparse distribution. However, for the dense 20 mm trichomes, increasing H/D lowers deposition rate.

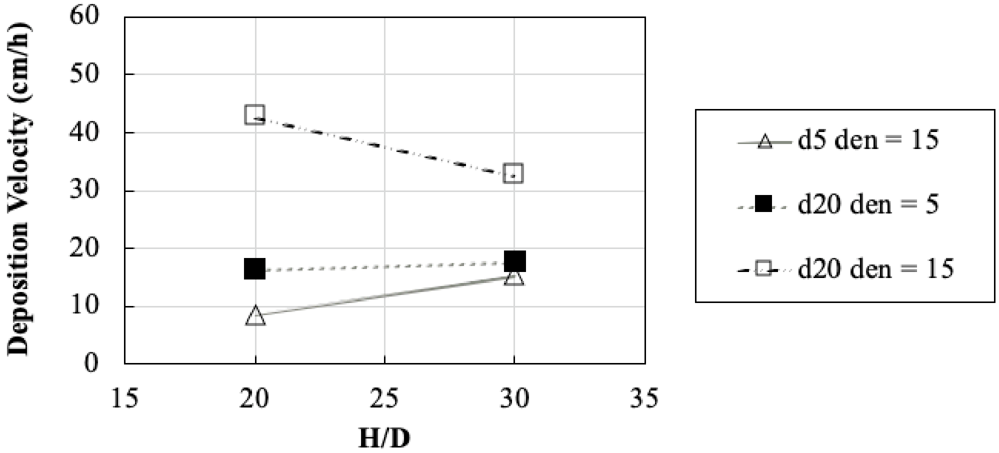

Figure 30 The effect of H/D ratio on PM0.3 deposition

Figure 31 plots the deposition velocity as a function of trichome density for different combinations of trichome diameter (5 and 20 μm) and H/D ratios. There is a uniform increase in deposition when the density increases from 5 to 15 mm^{-2} for all cases, similar to the findings of Moradi et al. [79]. As illustrated in Figure 31, the greatest improvement in particle removal when trichomes become denser is found for the thicker and shorter trichomes (LH_d20_hd20). As discussed earlier in Section 4.3.1.1, the near-surface u-velocity fields for the 20 μm trichomes decrease significantly at a higher density, whereas the flow fields for the LH_d5_hd20 cases are almost identical between densities of 5 mm^{-2} and 15 mm^{-2}.

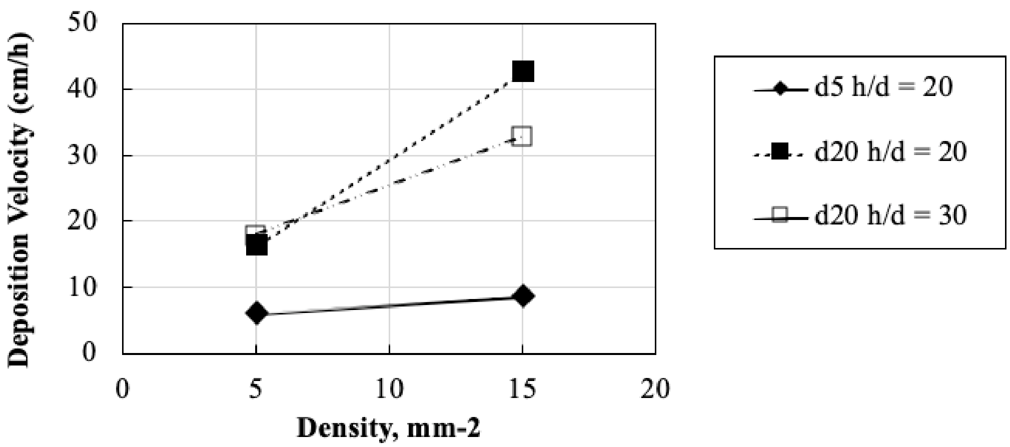

Figure 31 The effect of trichome density on PM0.3 deposition

The deposition velocity on the leaf with 20 µm diameter trichomes ranges from 16.4 – 43.9 cm/h, which is about 1.5 - 4 times higher than the smooth leaf (10.8 cm/h). Leonard et al. [82], also observed a similar trend where the presence of leaf hair promotes particle accumulation by three-fold compared to leaves with no hair. Similar findings were also observed by Little [83], Kardel et al.[71], Saebo et al.[63], and Speak et al. [66].

For the thinner trichomes, however, the deposition velocity ranges from 6.12 – 15.4 cm/h, with the H/D = 20 trichomes yielding lower deposition velocity than the smooth leaf. This could be related to the D^*_{hair}/D^*_p which will be discussed further in Section 4.3.3.2.

In addition to the overall deposition velocity, the deposition on leaf surface versus trichomes is also analyzed individually. Charts, where the deposition velocity is decomposed, are given in Figure 32 for the 5 µm trichomes. At the trichome diameter of 5 µm, increasing trichome density by a factor of three from 5 mm^{-2} to 15 mm^{-2} increases the deposition on trichomes three-fold. A similar trend is also observed for the 20 µm diameter trichomes, where the removal by trichomes increases by 2-3 times.

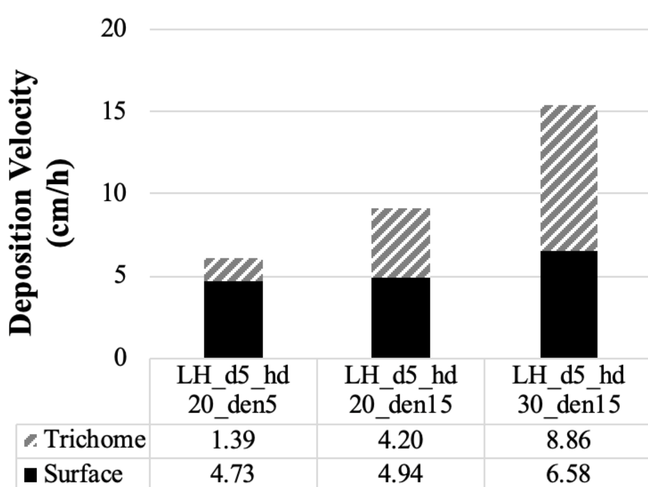

Figure 32 Deposition velocity on trichome and leaf surface for 5 µm trichomes

Figure 33 plots the breakdown of deposition between surface and trichome for the 20 μm trichomes. For the 20 μm trichomes, taller trichomes (H/D=30) show reduced surface deposition by 35-40%. Although the higher density elevates deposition on trichomes for the LH_d20_hd30 by 30%, it reduces deposition on the leaf surface, resulting in only a slight increase in the overall deposition velocity.

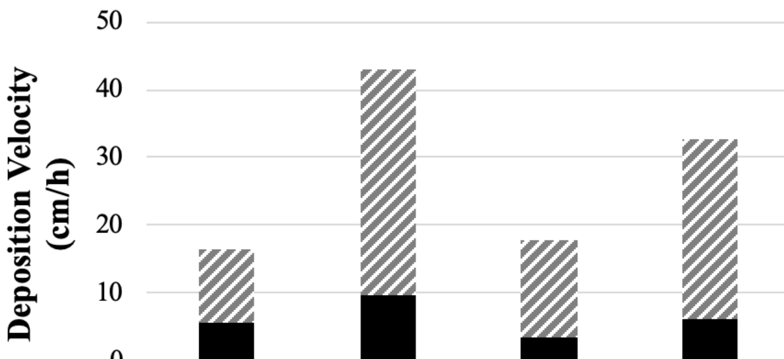

	LH_d20_hd20_den5	LH_d20_hd20_den15	LH_d20_hd30_den5	LH_d20_hd30_den15
Trichome	10.91	33.20	14.37	26.53
Surface	5.52	9.67	3.41	6.22

Figure 33 Deposition velocity on trichome and leaf surface for 20 μm trichomes

4.3.3.2 Effects of velocity on PM0.3 deposition

In general, deposition velocity is observed to increase from 16.43 to 19.53 cm/h as the mean velocity increases from 1 to 3 m/s in Figure 34. This positive relationship between wind speed was also observed by other researchers [67], [68], [84], [85] for the velocity in the range of 1-10 m/s. The trend is also uniform for deposition on both trichomes and leaf surface, and this relationship is in agreement with the similarity in the velocity profiles shown earlier in Figure 24.

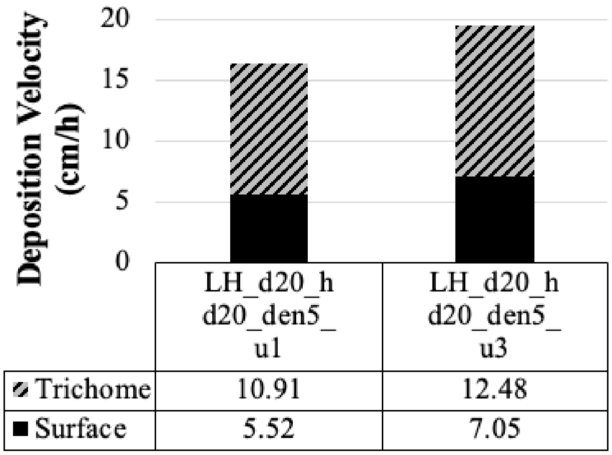

Figure 34 Deposition velocity for 0.3 μm particles at the wind speed of 1 and 3 m/s

4.3.3.3 Effects of particle size on PM1.0 deposition

At the mean velocity of 1 m/s, the deposition of PM0.3 and PM1.0 were studied. The deposition velocity was found to decrease by 20% from 16.43 to 12.23 cm/h in Figure 35 with the increase from PM0.3 to PM1.0. This relationship was observed by other researchers in the 3-180 μm particle diameter range [70]. Ottelé et al. [69] reported particles smaller than 10 μm to deposit more frequently than particles of larger size, however, they found no significant change in the accumulation between particles diameters < 0.5 μm and those between 0.5-1.0 μm in sizes. Belot and Gauthier [86] also observed that the deposition velocity was relatively insensitive for particles in the range 0.3 – 1.20 μm, compared to other size ranges.

To get a more comprehensive effect of particles size on the deposition, it might be necessary to consider other particle diameters. Nevertheless, the fact that drag forces increase in magnitude compared to Brownian forces and the reduction in D^*_{hair}/D^*_p from 66.7 to 20 could contribute to the decrease in the deposition.

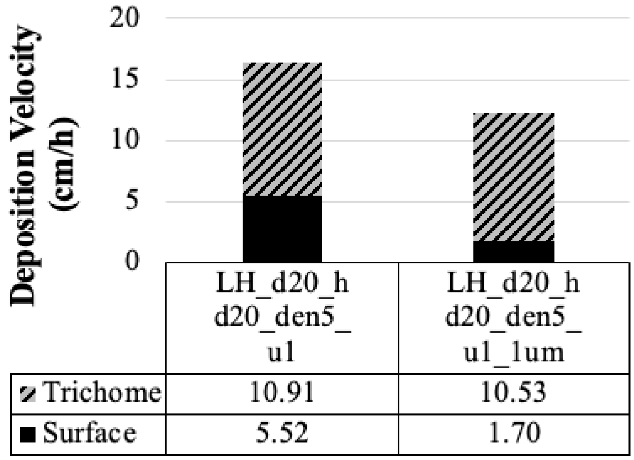

Figure 35 Deposition velocity for (left) 0.3 and (right) 1 μm particles

4.3.3.4 Correlations between deposition velocity and trichome and particle physical parameters

Mentioned earlier in Section 4.1.1, while the majority of researchers found a favorable result when leaf hairs are present, some cases in this study yield a lower deposition velocity than the plain leaf. Moreover, a negative correlation was also observed by Perini et al. [73] for stellate trichomes at a high density of about 20-44 mm^{-2} for moderately hairy leaves and for dense hairs at approximately 400 mm^{-2} (sizes were estimated by the author). Although the trichome geometry is very different from the ideal conditions in this study, the reduction in deposition velocity is possible if the presence of the trichomes while blocking access to the leaf surface, do not themselves capture enough particles to make up for the decrease. This will depend on many geometrical parameters defining the system.

In an attempt to consolidate the effect of different geometrical parameters, a multivariate linear correlation analysis is performed using a statistical software JMP Pro to provide a more comprehensive relationship between leaf morphology, particle diameters, and deposition velocity. The relevant statistics obtained from the software is given in Table 14. U^*_{dep} on trichomes shows a positive correlation with D^*_{hair} but a negative correlation on the leaf surface. A similar, but a weaker correlation is found with the ratio of trichome height to trichome diameter $\left(\frac{H^*_{hair}}{D^*_{hair}}\right)$ on the trichome surface with stronger negative correlation on the leaf surface. As expected, the deposition velocity correlates negatively with $\frac{S^*_{hair}}{D^*_{hair}}$ but shows a strong positive correlation with $\frac{H^*_{hair}}{S^*_{hair}}$. Combining $\frac{S^*_{hair}}{D^*_{hair}}$ and $\frac{H^*_{hair}}{D^*_{hair}}$ to form the group $\frac{(D^*_{hair})^2}{H^*_{hair}S^*_{hair}}$, which is a representation of the trichome area to cross-sectional flow area yields the highest linear correlation of 0.90 for overall deposition velocity. However, since this factor doesn't take into account the particle diameter, another ratio $\left(R_{hp} = \frac{D^*_{hair}}{D^*_p}\frac{(D^*_{hair})^2}{H^*_{hair}S^*_{hair}} = \frac{1}{D_p H_{hair} S_{hair}}\right)$ is proposed. This ratio is essentially a combination of the trichome surface area to flow cross-sectional area and the hair diameter to particle diameter ratio. This factor also yields a satisfactory linear correlation of 0.89. It should be noted, however, that this factor doesn't take into account the wind speed.

Table 14 Correlations analysis of different factors on Deposition velocity

	D^*_{hair} (μm)	$\frac{H^*_{hair}}{D^*_{hair}}$	$\frac{S^*_{hair}}{D^*_{hair}}$	$\frac{H^*_{hair}}{S^*_{hair}}$	$\frac{(D^*_{hair})^2}{H^*_{hair}S^*_{hair}}$	$\frac{D^*_{hair}H^*_{hair}}{(S^*_{hair})^2}$	$\frac{(H^*_{hair})^2}{D^*_{hair}S^*_{hair}}$	$\frac{D^*_{hair}}{D^*_p}\left(\frac{(D^*_{hair})^2}{H^*_{hair}S^*_{hair}}\right)$
U_{dep} (cm/h)	0.68	0.29	-0.54	0.82	0.90	0.87	0.68	0.89
U_{dep} on Trichomes (cm/h)	0.78	0.45	-0.46	0.87	0.90	0.90	0.74	0.90
U_{dep} on Leaf (cm/h)	-0.28	-0.66	-0.52	0.34	0.66	0.46	0.17	0.59

Deposition velocity for all the cases except the case at the wind speed of 3 m/s is plotted as a function of R_{hp} in Figure 36. This relationship predicts the deposition velocity well for R_{hp} up to 0.30, with some scatter from the linear trend. It should be noted also that more data points may yield a better description of the effects of trichome and particle characteristics beyond this range. For example, for short, thick trichomes that are tightly packed, R_{hp} will increase beyond the current range, but it is not clear if the removal of pollutants will also increase linearly.

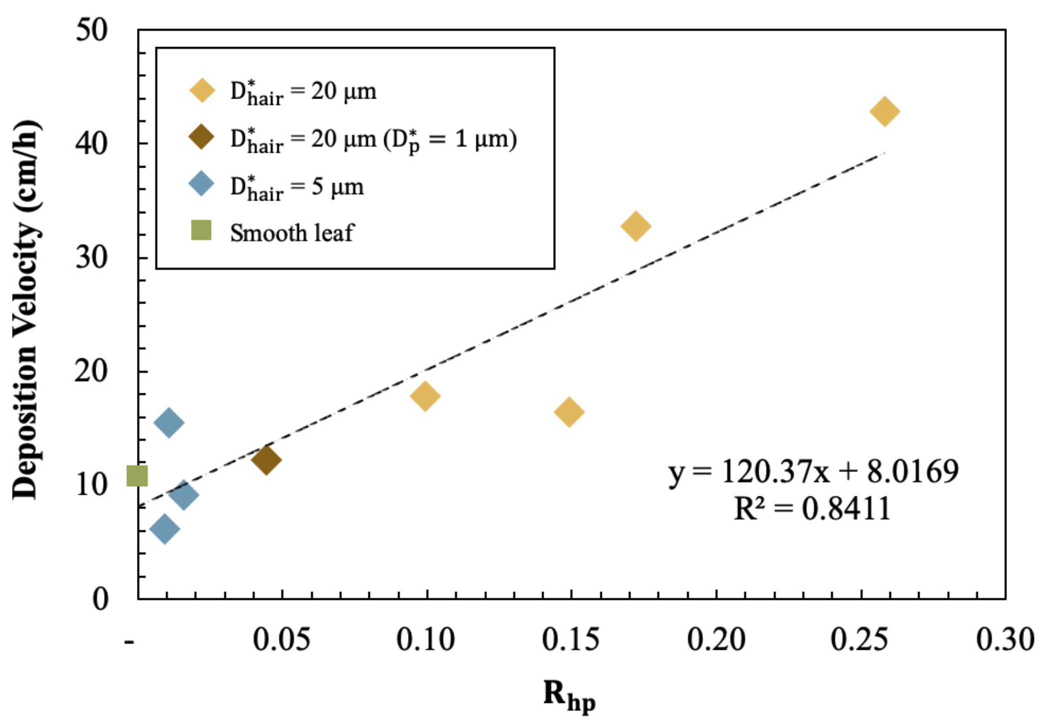

Figure 36 Deposition velocity as a function of the combination of leaf hair traits and particle sizes

4.3.3.5 Comparison to deposition velocity reported by other researchers

Although the relationships between the deposition velocity and different leaf traits as well as wind speed and particle size are in agreement with other studies as discussed earlier, the deposition velocities predicted in this study range from 0.002 to 0.012 cm/s, which are significantly lower than most values reported by other researchers (see Table 15). Nevertheless, the values in this range are not unprecedented. Studying deposition on oak leaves at different flow velocities, Reinap and Wiman [87] obtained the deposition velocity of 0.02 – 0.05 cm/s for a wind speed of 2 m/s which is also at the low end when compared to other published data. Another reported deposition velocity that is relatively close to this study is 0.004 cm/s which was observed by Klepper and Craig [88] and Vaughan [89] in the investigation of the deposition of 0.8 μm particles on bean leaves under low-speed flows (0.2 – 20 cm/s). Belot and Gautheir [86] also measured the deposition velocity ranging from 0.007 – 0.01 cm/s for Norway spruce canopies at the wind speed of 1 m/s.

Additionally, it is widely known that the deposition of fine particles is highly influenced by atmospheric instability [90]–[93] and finer scale turbulent instabilities that could be caused by the size and shape of the leaves. According to Weerakkody et al. [94], small leaves (1.7 cm^2) have almost 5 times greater deposition than large leaves (59.6 cm^2) of the same shape. With larger perimeter to surface area ratio (small: large = 27:7), the edge effect could be more significant, resulting in increased turbulence intensity in the boundary layer and increased deposition via impaction. Moreover, palmately-lobed leaves were also observed in the same study [94] to be more efficient in removing $PM_{1.0}$ due to their more complex morphology, which again produces high turbulence in the boundary layer. Elevated deposition on leaf edges and tips was also observed in the same study. Leaves with broader bases were also reported to flutter less and produce less drag than narrow leaves, thus increasing deposition probability [95]. Leonard et al. [82] have also found morphological factors such as leaf area, shape, and petiole length which affect leaf movement to significantly impact PM deposition on the leaf surface, and the observed mean accumulation across different species varies from < 1 mg/cm^2 to 12 mg/cm^2.

Table 15 Summary of published deposition velocities for different particle diameters, wind speeds on different leaf surfaces/species. * represents lab measurements, and ** represents field measurements.

Authors (Year)	Species or surface types	D_p^* (μm)	U_∞^* (m/s)	u_τ^* (cm/s)	U_{dep}^* (cm/s)
Bunzl et al. (1989)** [105]	Picea abies (spruce)	Various (134, 137 Cs and 106 Ru)	Various		0.55
White and Turner (1970)** [106]	Fraxinus excelsior	0.1–20	2		6.8
	Quercus petraea				3.2
	Betula pubescens				6.4
	Corylus avellana				20
Peters and Eiden (1992) [107]	Picea abies (spruce)	1	0.5		0.02 (Modeled)
Beckett et al. (2000c)* [68]	Populus nigra × Cupressocyparis leylandii	0.8	0.7		0.02–0.12
	Acer campestre				
	Populus deltoides × trichocarpa				
	As above and Sorbus intermedia	1.28	1, 3, 8 and 10		0.03–28.05
Freer-Smith et al. (2005)* [85]	Quercus petraea	0.8	3–9		0.8–3.1
	Alnus glutinosa				0.1–0.8
	Fraxinus excelsior				0.2–0.7
	Acer pseudo platanus				0.04–0.3
QUARG (1996)** [108]	Grassland	0.01–12	–		0.02–10
Gallagher et al. (1997)** [109]	Pseudotsuga menchizii (Douglas fir)	0.01–10	Various		0.1–10
Chamberlain (1967)* [110]	Grass	0.1			0.03
		1			
		2			0.1
		5			0.8
Klepper and Craig (1975)* [88]	Bean leaves	AMAD 0.8	0.0042		0.0035
Vaughan (1976)* [89]	Bean leaves	0.8 (Au colloid)	0.002 – 0.2		0.004
	Field	0.05 - 0.1		5.5 - 20	0.1 - 1.1
Little (1977)* [83]	Nettle	2.75	2.5		0.5
	Beech				0.04
	White Poplar				0.3
Chamberlain (1953)** [111]	Grass	16	1.1		0.5
			3.2		1.1
			9.2		2.1
Clough (1975)** [84]	Grass	3-4		37	0.74 - 1.1
		0.5	1	18	0.0125
			3	30	0.025
			4.5	80	0.04
Belot and Gauthier (1975)* [86]	Norway spruce	0.6 (Uranine)	1		0.007-0.01
Little and Wiffen (1977)* [112] (Pb auto exhaust)	Whole leaves	Aggregated (recirculation 0.1-0.25 μm)	2.5		0.008-0.039
	Leaf discs				0.007 - 0.025
	Oak leaves	< 1			0.003 – 0.006
Reinap and Wiman (2009)* [87]	Oak leaves	AMAD 1.2	2		0.01 ± 0.002
Present	Modeled leaf surface	0.3	1	2.6 – 5.6	0.0017 – 0.0119
			3	6.2	0.0054
		1	1	3.5	0.0034

It is noted that in the present study no edge effects are included and only the region very close to the leaf surface (~1 mm) is investigated. Therefore, transport by atmospheric turbulence, and turbulence generated by flow separation at leading edges produced by the leaf macro-morphology in the wind tunnel and field measurements, and other non-canonical hydrodynamic effects are not included. As a result, the deposition velocities presented in this study will be much lower than the measurements.

Moreover, comparing to the field or wind tunnel measurements, the friction velocity in this study ranges between 2.6 to 6 cm/s which is lower than the friction velocities reported by other studies (see Table 15). It is observed by different researchers that there is a positive correlation between the friction velocity and deposition velocity [89], [92], [96]. Figure 37 and Figure 38 show comparisons between different experiments and models for predicting deposition velocities as a function of particle aerodynamic diameter for plant and smooth surfaces, respectively. The "plant" here refers to a synthetic tree in a wind tunnel. As shown in Figure 37, there is a wide range of deposition velocities on the plant surface even at the same particle diameter. However, due to less variety in surface characteristics of the smooth surface, there is less variation between measurements and predictions. The deposition velocity of 0.003 cm/s obtained for the smooth leaf in the present study for 0.3 μm aerosols at the friction velocity of 0.0350 m/s, showing agreement with the models and measurements shown in Figure 38.

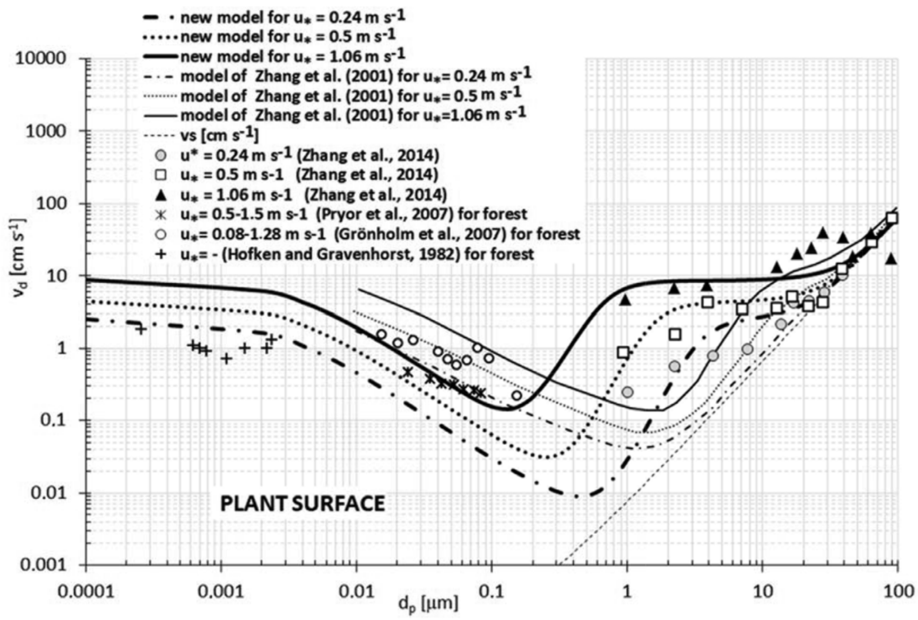

Figure 37 A comparison between deposition velocity measurements by Zhang et al. [97], Pryor et al. [98], Grönholm et al. [99], and Hofken and Gravenhorst [100] and predictions by Zhang et al. [75] and Giardina and Buffa [101] for plant covered surface (Source: Giardina and Buffa [101]).

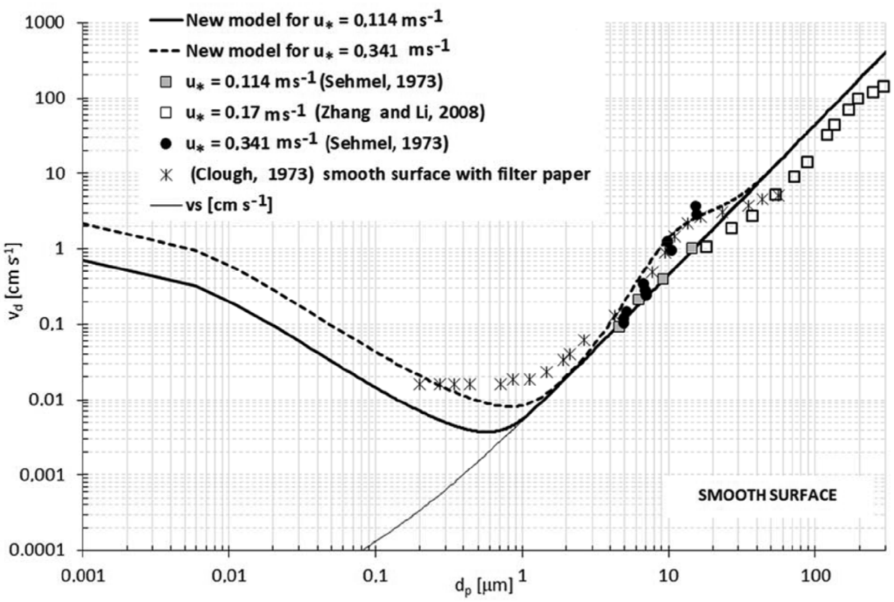

Figure 38 A comparison between deposition velocity measurements by Sehmel [102], Zhang and Li [103] and Clough [104] and predictions by Giardina and Buffa [101] for smooth surface (Source: Giardina and Buffa [101]).

Additionally, since this is the first study that aims to parameterize leaf micro-morphology, the leaf surface as well as trichomes are idealized and do not replicate the full complexity of natural vegetation. As briefly discussed in Section 4.1.2, trichomes come in different arrangements and shapes. For example, the trichomes found on the upper surface of oak leaves (sp. *Quercus canariensis*) studied by Tschan and Denk [78] were identified as acicular, stellate, and capitate. Different types and density of trichomes were also observed on the lower surface for different species. Stellate and fasciculate trichomes were found to retain more dust [79]. Therefore, these factors could result in higher deposition velocity than the idealized trichomes modeled in this study.

Regardless, the results produced by this study offer a better understanding of the contributions of trichome general traits in isolation from other leaf characteristics. Future work on this topic could introduce more realistic modeling where the leaf is modeled as a finite surface with other traits. More work on different traits as well as the macro-characteristics of leaf surface could also yield a more comprehensive description of different factors affecting particle deposition and aid planners in selecting vegetation to combat pollution.

4.4 Conclusion and Future Work

Street vegetation has received much attention from urban planners as a tool to mitigate urban pollution crisis due to its ability to remove pollution through the chemical and physical process through wet and dry deposition. While a dry deposition is the main focus of this study, aerosol accumulation on vegetation surface is affected by many factors such as atmospheric turbulence level, aerosol properties as well as the biophysical characteristics of plants [7]. Although the impact of aerosol size and leaf morphology has been studied by other researchers [63]–[67], the complexity of these factors results in a wide range of deposition velocity across different plant species and poses challenges in parameterization. Therefore, this study aims to identify the effects of trichome traits (i.e. diameter, diameter to height ratio, and density), particle size, and wind speed on the deposition of fine PM on the leaf surface.

To develop a fundamental understanding of this process, the leaf surface is modeled as an infinitely large plane with cylindrical trichomes of uniform diameter and equal spacing. One-way coupling was used to model fluid-particle interactions which are dominated by Brownian and drag forces, with the additional assumption that all particles that impinge on a surface will deposit.

Trichomes that are 20 μm in diameter are observed to be more effective in capturing 0.3 μm aerosols than the 5 μm diameter trichomes. Moreover, the deposition velocity on leaf hairs increases by 2-3 times as the trichome density rises from 5 to 15 mm^{-2} for both trichome diameters. Although taller trichomes do not show a clear impact on the overall deposition, more deposition on the leaf surface is observed for the 20 μm diameter trichomes. As the mean wind speed rises from 1 to 3 m/s, a positive relationship is also observed. At larger particle diameter (D_p^* = 1 μm), the deposition velocity was found to decrease by 20% from 16.43 to 12.23 cm/h.

To obtain a more comprehensive relationship between these factors, statistical software was used to evaluate the linear correlation between different combinations of trichome characteristics. The ratio $R_{hp} = \frac{D_{hair}^*}{D_p^*} \frac{(D_{hair}^*)^2}{H_{hair}^* S_{hair}^*}$ was found to best correlate with deposition velocity, yielding a satisfactory Pearson linear correlation strength of 0.89 for $R_{hp} < 0.3$ at the mean speed of 1 m/s.

Although deposition velocity exhibits a wide range across different plant species, the deposition velocities predicted in this study are between 0.002 and 0.012 cm/s, which are at the lower end of most values reported by other researchers in large scale field and wind tunnel experiments. This discrepancy could be a result of the idealized nature of the leaf modeled in this investigation which does not take into an account the leaf shape, size ,and edge effects, all of which are observed to increase particle deposition by other researchers. Nevertheless, the results produced here provide a clearer understanding of general trichome characteristics in isolation from other traits.

Future work in parameterizing leaf characteristics should consider a larger range of R_{hp} at different wind speeds. Investigating a more complex trichome morphology, wax and groves on the leaf surface, as well as leaf shape and size, may also give a more quantitative understanding of how these factors affect particle deposition. Moreover, complementary experimental studies should also be considered to provide a more realistic understanding of aerosol removal by vegetation and better aid planners in selecting vegetation to combat the rising pollution crisis in urban areas.

REFERENCES

[1] O. US EPA, "Urban Air Toxics."

[2] "68% of the world population projected to live in urban areas by 2050, says UN | UN DESA | United Nations Department of Economic and Social Affairs." [Online]. Available: https://www.un.org/development/desa/en/news/population/2018-revision-of-world-urbanization-prospects.html. [Accessed: 03-Oct-2018].

[3] A. Martos, R. Pacheco-Torres, J. Ordóñez, and E. Jadraque-Gago, "Towards successful environmental performance of sustainable cities: Intervening sectors. A review," *Renew. Sustain. Energy Rev.*, vol. 57, pp. 479–495, May 2016.

[4] A. P. R. Jeanjean, R. Buccolieri, J. Eddy, P. S. Monks, and R. J. Leigh, "Air quality affected by trees in real street canyons: The case of Marylebone neighbourhood in central London," *Urban For. Urban Green.*, vol. 22, pp. 41–53, Mar. 2017.

[5] Y. Toparlar, B. Blocken, B. Maiheu, and G. J. F. van Heijst, "A review on the CFD analysis of urban microclimate," *Renew. Sustain. Energy Rev.*, vol. 80, pp. 1613–1640, Dec. 2017.

[6] "Ambient air pollution: Pollutants," 2017. [Online]. Available: https://www.who.int/airpollution/ambient/pollutants/en/. [Accessed: 10-Jan-2019].

[7] J. H. Seinfeld and S. N. Pandis, Atmospheric chemistry and physics : from air pollution to climate change. Wiley, 2016.

[8] "Ambient (outdoor) air quality and health," *World Health Organization*. 2018.

[9] D. K. Tafti, “GenIDLEST - A scalable parallel computational tool for simulating complex turbulent flows,” in *ASME-PUBLICATIONS-FED 256*, 2001, vol. 256, pp. 347–356.

[10] J. SMAGORINSKY, “GENERAL CIRCULATION EXPERIMENTS WITH THE PRIMITIVE EQUATIONS,” *Mon. Weather Rev.*, 1963.

[11] F. M. Najjar and D. K. Tafti, “Study of discrete test filters and finite difference approximations for the dynamic subgrid-scale stress model,” *Phys. Fluids*, 1996.

[12] F. White and I. Corfield, *Viscous fluid flow*. 1991.

[13] L. W. Zhang, D. K. Tafti, F. M. Najjar, and S. Balachandar, “Computations of flow and heat transfer in parallel-plate fin heat exchangers on the CM-5: effects of flow unsteadiness and three-dimensionality,” *Int. J. Heat Mass Transf.*, vol. 40, no. 6, pp. 1325–1341, Apr. 1997.

[14] C. R. Wilke, “A Viscosity Equation for Gas Mixtures,” *J. Chem. Phys.*, vol. 18, no. 4, pp. 517–519, Apr. 1950.

[15] S. Chapman, D. Burnett, and T. G. Cowling, The mathematical theory of non-uniform gases / Sydney Chapman and T.G. Cowling. - Version details - Trove, 3rd ed. Cambridge: Cambridge University Press, 1970.

[16] D. K. Tafti, “Time-accurate techniques for turbulent heat transfer analysis in complex geometries,” in *WIT Transactions on State-of-the-art in Science and Engineering*, vol. 41, WIT Press, 2010, pp. 217–264.

[17] C. Gromke and B. Ruck, “CODASC (Concentration Data of Street Canyons).” [Online]. Available: www.codasc.de.

[18] B. Blocken, “50 years of Computational Wind Engineering: Past, present and future,” *J. Wind Eng. Ind. Aerodyn.*, vol. 129, pp. 69–102, Jun. 2014.

[19] B. Blocken, "Computational Fluid Dynamics for urban physics: Importance, scales, possibilities, limitations and ten tips and tricks towards accurate and reliable simulations," *Build. Environ.*, vol. 91, pp. 219–245, Sep. 2015.

[20] C. J. Baker, "Wind engineering—Past, present and future," *J. Wind Eng. Ind. Aerodyn.*, vol. 95, no. 9–11, pp. 843–870, Oct. 2007.

[21] B. Blocken, T. Stathopoulos, and J. P. A. J. van Beeck, "Pedestrian-level wind conditions around buildings: Review of wind-tunnel and CFD techniques and their accuracy for wind comfort assessment," *Build. Environ.*, vol. 100, pp. 50–81, May 2016.

[22] K. Hanjalic, "Will RANS Survive LES? A View of Perspectives," *J. Fluids Eng.*, vol. 127, no. 5, p. 831, Sep. 2005.

[23] R. Yoshie *et al.*, "Cooperative project for CFD prediction of pedestrian wind environment in the Architectural Institute of Japan," *J. Wind Eng. Ind. Aerodyn.*, vol. 95, no. 9–11, pp. 1551–1578, Oct. 2007.

[24] S. Murakami, A. Mochida, Y. Hayashi, and S. Sakamoto, "Numerical study on velocity-pressure field and wind forces for bluff bodies by κ-ϵ, ASM and LES," *J. Wind Eng. Ind. Aerodyn.*, vol. 44, no. 1–3, pp. 2841–2852, Oct. 1992.

[25] S. Murakami, A. Mochida, and K. Hibi, "Three-dimensional numerical simulation of air flow around a cubic model by means of large eddy simulation," *J. Wind Eng. Ind. Aerodyn.*, vol. 25, no. 3, pp. 291–305, Jan. 1987.

[26] Y. Tominaga and T. Stathopoulos, "Numerical simulation of dispersion around an isolated cubic building: Model evaluation of RANS and LES," *Build. Environ.*, vol. 45, no. 10, pp. 2231–2239, Oct. 2010.

[27] T. van Hooff, B. Blocken, P. Gousseau, and G. J. F. van Heijst, “Counter-gradient diffusion in a slot-ventilated enclosure assessed by LES and RANS,” *Comput. Fluids*, vol. 96, pp. 63–75, Jun. 2014.

[28] S. Murakami, “Numerical simulation of turbulent flowfield around cubic model current status and applications of k−ϵ model and LES,” *J. Wind Eng. Ind. Aerodyn.*, vol. 33, no. 1–2, pp. 139–152, Mar. 1990.

[29] C. Gromke, R. Buccolieri, S. Di Sabatino, and B. Ruck, “Dispersion study in a street canyon with tree planting by means of wind tunnel and numerical investigations - Evaluation of CFD data with experimental data,” *Atmos. Environ.*, 2008.

[30] S. M. Salim, R. Buccolieri, A. Chan, and S. Di Sabatino, “Numerical simulation of atmospheric pollutant dispersion in an urban street canyon: Comparison between RANS and LES,” *J. Wind Eng. Ind. Aerodyn.*, 2011.

[31] S. Vranckx, P. Vos, B. Maiheu, and S. Janssen, “Impact of trees on pollutant dispersion in street canyons: A numerical study of the annual average effects in Antwerp, Belgium,” *Sci. Total Environ.*, vol. 532, pp. 474–483, Nov. 2015.

[32] L. Merlier, J. Jacob, and P. Sagaut, “Lattice-Boltzmann Large-Eddy Simulation of pollutant dispersion in street canyons including tree planting effects,” *Atmos. Environ.*, vol. 195, pp. 89–103, Dec. 2018.

[33] S. M. Salim, R. Buccolieri, A. Chan, S. Di Sabatino, and S. C. Cheah, “Large eddy simulation of the aerodynamic effects of trees on pollutant concentrations in street canyons,” *Procedia Environ. Sci.*, vol. 4, pp. 17–24, Jan. 2011.

[34] J. Gallagher and C. Lago, “How parked cars affect pollutant dispersion at street level in an urban street canyon? A CFD modelling exercise assessing geometrical detailing and pollutant decay rates,” *Sci. Total Environ.*, vol. 651, pp. 2410–2418, Feb. 2019.

[35] M. Balczó, C. Gromke, and B. Ruck, “Numerical modeling of flow and pollutant dispersion in street canyons with tree planting,” in *Meteorologische Zeitschrift*, 2009, vol. 18, no. 2, pp. 197–206.

[36] A. P. R. Jeanjean, G. Hinchliffe, W. A. McMullan, P. S. Monks, and R. J. Leigh, “A CFD study on the effectiveness of trees to disperse road traffic emissions at a city scale,” *Atmos. Environ.*, vol. 120, pp. 1–14, Nov. 2015.

[37] G. Kang, J.-J. Kim, D.-J. Kim, W. Choi, and S.-J. Park, “Development of a computational fluid dynamics model with tree drag parameterizations: Application to pedestrian wind comfort in an urban area,” *Build. Environ.*, vol. 124, pp. 209–218, Nov. 2017.

[38] C. Yuan, R. Shan, A. S. Adelia, A. Tablada, S. K. Lau, and S. S.-Y. Lau, “Effects of vertical farming on natural ventilation of residential buildings,” *Energy Build.*, vol. 185, pp. 316–325, Feb. 2019.

[39] S. M. Salim, S. C. Cheah, and A. Chan, “Numerical simulation of dispersion in urban street canyons with avenue-like tree plantings: Comparison between RANS and LES,” *Build. Environ.*, vol. 46, no. 9, pp. 1735–1746, Sep. 2011.

[40] P. Moonen, C. Gromke, and V. Dorer, “Performance assessment of Large Eddy Simulation (LES) for modeling dispersion in an urban street canyon with tree planting,” *Atmos. Environ.*, vol. 75, pp. 66–76, Aug. 2013.

[41] G. Kang, J.-J. Kim, D.-J. Kim, W. Choi, and S.-J. Park, “Development of a computational fluid dynamics model with tree drag parameterizations: Application to pedestrian wind comfort in an urban area,” *Build. Environ.*, vol. 124, pp. 209–218, Nov. 2017.

[42] R. Buccolieri *et al.*, “Analysis of local scale tree–atmosphere interaction on pollutant concentration in idealized street canyons and application to a real urban junction,” *Atmos. Environ.*, vol. 45, no. 9, pp. 1702–1713, Mar. 2011.

[43] R. Buccolieri, C. Gromke, S. Di Sabatino, and B. Ruck, “Aerodynamic effects of trees on pollutant concentration in street canyons,” *Sci. Total Environ.*, vol. 407, no. 19, pp. 5247–5256, Sep. 2009.

[44] K. V. Abhijith and S. Gokhale, “Passive control potentials of trees and on-street parked cars in reduction of air pollution exposure in urban street canyons,” *Environ. Pollut.*, vol. 204, pp. 99–108, Sep. 2015.

[45] F. Xue and X. Li, “The impact of roadside trees on traffic released PM10 in urban street canyon: Aerodynamic and deposition effects,” *Sustain. Cities Soc.*, vol. 30, pp. 195–204, Apr. 2017.

[46] X. Xie, C.-H. Liu, and D. Y. C. Leung, “Impact of building facades and ground heating on wind flow and pollutant transport in street canyons,” *Atmos. Environ.*, vol. 41, no. 39, pp. 9030–9049, Dec. 2007.

[47] X.-X. Li *et al.*, “Large-Eddy Simulation of Flow and Pollutant Transport in Urban Street Canyons with Ground Heating,” *Boundary-Layer Meteorol.*, vol. 137, no. 2, pp. 187–204, Nov. 2010.

[48] K.-H. Kwak *et al.*, "Computational Fluid Dynamics Modelling of the Diurnal Variation of Flow in a Street Canyon," vol. 141, pp. 77–92, 2011.

[49] A. De Lieto Vollaro *et al.*, "Numerical Study of Urban Canyon Microclimate Related to Geometrical Parameters," *Sustainability*, vol. 6, no. 11, pp. 7894–7905, Nov. 2014.

[50] S. Bottillo, A. De Lieto Vollaro, G. Galli, and A. Vallati, "Fluid dynamic and heat transfer parameters in an urban canyon," *Sol. Energy*, vol. 99, pp. 1–10, Jan. 2014.

[51] S. Bottillo, A. De Lieto Vollaro, G. Galli, and A. Vallati, "CFD modeling of the impact of solar radiation in a tridimensional urban canyon at different wind conditions," *Sol. Energy*, vol. 102, pp. 212–222, Apr. 2014.

[52] C. Gromke and B. Ruck, "On the Impact of Trees on Dispersion Processes of Traffic Emissions in Street Canyons," *Boundary-Layer Meteorol.*, vol. 131, no. 1, pp. 19–34, Apr. 2009.

[53] M. G. Balczó and B. Ruck, "Numerical modeling of flow and pollutant dispersion in street canyons with tree planting," *Meteorol. Zeitschrift*, vol. 18, no. 2, pp. 197–206, May 2009.

[54] J. J. Franke, A. Hellsten, H. Schlünzen, and B. Carissimo, Best practice guideline for the CFD simulation of flows in the urban environment. 2007.

[55] H. Worth, W. Nüsse, and J. Piiper, "Determination of binary diffusion coefficients of various gas species used in respiratory physiology," *Respir. Physiol.*, vol. 32, no. 1, pp. 15–26, 1978.

[56] J.-F. Sini, S. Anquetin, and P. G. Mestayer, "Pollutant dispersion and thermal effects in urban street canyons," *Atmos. Environ.*, vol. 30, no. 15, pp. 2659–2677, Aug. 1996.

[57] N. Center for Health Statistics, Vital and Health Statistics, Series 3, Number 39, (08/2016). 2011.

[58] J. C. Chang and S. R. Hanna, “Air quality model performance evaluation,” *Meteorol Atmos Phys*, vol. 87, pp. 167–196, 2004.

[59] S. Hanna and J. Chang, “Acceptance criteria for urban dispersion model evaluation,” *Meteorol. Atmos. Phys.*, vol. 116, no. 3–4, pp. 133–146, May 2012.

[60] T. Fisher, “Frederick Law Olmsted and the Campaign for Public Health,” *Places J.*, no. 2010, Nov. 2010.

[61] J. A. Businger, “Evaluation of the Accuracy with Which Dry Deposition Can Be Measured with Current Micrometeorological Techniques,” *J. Clim. Appl. Meteorol.*, 1986.

[62] S. C. Pryor *et al.*, “A review of measurement and modelling results of particle atmosphere-surface exchange,” *Tellus, Series B: Chemical and Physical Meteorology*. 2008.

[63] A. Sæbø, R. Popek, B. Nawrot, H. M. Hanslin, H. Gawronska, and S. W. Gawronski, “Plant species differences in particulate matter accumulation on leaf surfaces,” *Sci. Total Environ.*, 2012.

[64] A. Tiwary *et al.*, “An integrated tool to assess the role of new planting in PM10 capture and the human health benefits: A case study in London,” *Environ. Pollut.*, 2009.

[65] C. Gromke and B. Ruck, “Aerodynamic modelling of trees for small-scale wind tunnel studies,” *Forestry*, 2008.

[66] A. F. Speak, J. J. Rothwell, S. J. Lindley, and C. L. Smith, “Urban particulate pollution reduction by four species of green roof vegetation in a UK city,” *Atmos. Environ.*, 2012.

[67] P. H. Freer-Smith, A. A. El-Khatib, and G. Taylor, “Capture of particulate pollution by trees: A comparison of species typical of semi-arid areas (Ficus nitida and Eucalyptus globulus) with European and North American species,” *Water. Air. Soil Pollut.*, 2004.

[68] K. P. Beckett, P. H. Freer-Smith, and G. Taylor, "Particulate pollution capture by urban trees: effect of species and windspeed," *Glob. Chang. Biol.*, vol. 6, no. 8, pp. 995–1003, Dec. 2000.

[69] M. Ottelé, H. D. van Bohemen, and A. L. A. Fraaij, "Quantifying the deposition of particulate matter on climber vegetation on living walls," *Ecol. Eng.*, vol. 36, no. 2, pp. 154–162, Feb. 2010.

[70] F. Weber, I. Kowarik, and I. Säumel, "Herbaceous plants as filters: Immobilization of particulates along urban street corridors," *Environ. Pollut.*, vol. 186, pp. 234–240, Mar. 2014.

[71] F. Kardel, K. Wuyts, B. A. Maher, R. Hansard, and R. Samson, "Leaf saturation isothermal remanent magnetization (SIRM) as a proxy for particulate matter monitoring: Inter-species differences and in-season variation," *Atmos. Environ.*, vol. 45, no. 29, pp. 5164–5171, Sep. 2011.

[72] R. Mitchell, B. A. A. Maher, and R. Kinnersley, "Rates of particulate pollution deposition onto leaf surfaces: Temporal and inter-species magnetic analyses," *Environ. Pollut.*, vol. 158, no. 5, pp. 1472–1478, May 2010.

[73] K. Perini, M. Ottelé, S. Giulini, A. Magliocco, and E. Roccotiello, "Quantification of fine dust deposition on different plant species in a vertical greening system," *Ecol. Eng.*, 2017.

[74] S. Janhäll, "Review on urban vegetation and particle air pollution - Deposition and dispersion," *Atmospheric Environment*, vol. 105. pp. 130–137, 2015.

[75] L. Zhang, S. Gong, J. Padro, and L. Barrie, "A size-segregated particle dry deposition scheme for an atmospheric aerosol module," *Atmos. Environ.*, vol. 35, no. 3, pp. 549–560, Jan. 2001.

[76] Y. L. Wu, C. I. Davidson, D. A. Dolske, and S. I. Sherwood, “Dry deposition of atmospheric contaminants: The relative importance of aerodynamic, boundary layer and, surface resistances,” *Aerosol Sci. Technol.*, 1992.

[77] D. Voigt, E. Gorb, and S. Gorb, “Plant surface–bug interactions: Dicyphus errans stalking along trichomes,” *Arthropod. Plant. Interact.*, 2007.

[78] G. F. Tschan and T. Denk, “Trichome types, foliar indumentum and epicuticular wax in the Mediterranean gall oaks, Quercus subsection Galliferae (Fagaceae): implications for taxonomy, ecology and evolution,” *Bot. J. Linn. Soc.*, vol. 169, no. 4, pp. 611–644, Aug. 2012.

[79] A. Moradi, K. Taheri Abkenar, M. Afshar Mohammadian, and N. Shabanian, “Effects of dust on forest tree health in Zagros oak forests,” *Environ. Monit. Assess.*, vol. 189, no. 11, p. 549, Nov. 2017.

[80] “United States Environmental Protection Agency.” [Online]. Available: https://www.epa.gov/. [Accessed: 24-Apr-2019].

[81] D. A. Grantz, J. H. B. Garner, and D. W. Johnson, “Ecological effects of particulate matter,” *Environment International*. 2003.

[82] R. J. Leonard, C. McArthur, and D. F. Hochuli, “Particulate matter deposition on roadside plants and the importance of leaf trait combinations,” *Urban For. Urban Green.*, vol. 20, pp. 249–253, Dec. 2016.

[83] P. Little, “Deposition of 2.75, 5.0 and 8.5 μm particles to plant and soil surfaces,” *Environ. Pollut.*, vol. 12, no. 4, pp. 293–305, Apr. 1977.

[84] W. S. Clough, “The deposition of particles on moss and grass surfaces,” *Atmos. Environ.*, vol. 9, no. 12, pp. 1113–1119, Jan. 1975.

[85] P. H. Freer-Smith, K. P. Beckett, and G. Taylor, “Deposition velocities to Sorbus aria, Acer campestre, Populus deltoides × trichocarpa ‘Beaupré’, Pinus nigra and × Cupressocyparis leylandii for coarse, fine and ultra-fine particles in the urban environment,” *Environ. Pollut.*, vol. 133, no. 1, pp. 157–167, Jan. 2005.

[86] Y. Belot and D. Gauthier, “Transport of micronic particles from atmosphere to foliar surfaces,” 1975.

[87] A. Reinap, B. L. B. Wiman, B. Svenningsson, and S. Gunnarsson, “Oak leaves as aerosol collectors: relationships with wind velocity and particle size distribution. Experimental results and their implications.”

[88] B. Klepper and D. K. Craig, “Deposition of Airborne Particulates onto Plant Leaves1,” *J. Environ. Qual.*, vol. 4, no. 4, p. 495, 1975.

[89] B. Vaughan, “Suspended particle interactions and uptake in terrestrial plants,” 1976.

[90] M. L. Wesely, D. R. Cook, R. L. Hart, and R. E. Speer, “Measurements and parameterization of particulate sulfur dry deposition over grass,” *J. Geophys. Res. Atmos.*, vol. 90, no. D1, pp. 2131–2143, Feb. 1985.

[91] E. Lamaud, Y. Brunet, A. Labatut, A. Lopez, J. Fontan, and A. Druilhet, “The Landes experiment: Biosphere-atmosphere exchanges of above a pine forest ozone and aerosol particles,” 1994.

[92] W. G. . Slinn, “Predictions for particle deposition to vegetative canopies,” *Atmos. Environ.*, vol. 16, no. 7, pp. 1785–1794, Jan. 1982.

[93] A. Petroff, A. Mailliat, M. Amielh, and F. Anselmet, “Aerosol dry deposition on vegetative canopies. Part I: Review of present knowledge,” *Atmos. Environ.*, vol. 42, no. 16, pp. 3625–3653, May 2008.

[94] U. Weerakkody, J. W. Dover, P. Mitchell, and K. Reiling, “Evaluating the impact of individual leaf traits on atmospheric particulate matter accumulation using natural and synthetic leaves,” *Urban For. Urban Green.*, vol. 30, pp. 98–107, Mar. 2018.

[95] S. VOGEL, “Drag and Reconfiguration of Broad Leaves in High Winds,” *J. Exp. Bot.*, vol. 40, no. 8, pp. 941–948, Aug. 1989.

[96] G. A. Sehmel, “Particle and gas dry deposition: A review,” *Atmos. Environ.*, vol. 14, no. 9, pp. 983–1011, Jan. 1980.

[97] J. Zhang and Y. Shao, “A new parameterization of dust dry deposition over rough surfaces,” *Atmos. Chem. Phys. Discuss.*, vol. 14, no. 6, pp. 8063–8094, Mar. 2014.

[98] S. C. Pryor *et al.*, “Particle fluxes over forests: Analyses of flux methods and functional dependencies,” *J. Geophys. Res.*, vol. 112, no. D7, p. D07205, Apr. 2007.

[99] T. Grönholm *et al.*, “Measurements of aerosol particle dry deposition velocity using the relaxed eddy accumulation technique,” *Tellus B Chem. Phys. Meteorol.*, vol. 59, no. 3, pp. 381–386, Jan. 2007.

[100] K. D. Höfken and G. Gravenhorst, “Deposition of Atmospheric Aerosol Particles to Beech- and Spruce Forest,” in *Deposition of Atmospheric Pollutants*, Dordrecht: Springer Netherlands, 1982, pp. 191–194.

[101] M. Giardina and P. Buffa, “A new approach for modeling dry deposition velocity of particles,” *Atmos. Environ.*, vol. 180, pp. 11–22, May 2018.

[102] G. A. Sehmel, “Particle eddy diffusivities and deposition velocities for isothermal flow and smooth surfaces,” *J. Aerosol Sci.*, vol. 4, no. 2, pp. 125–138, Mar. 1973.

[103] J. Zhang and A. Li, “CFD simulation of particle deposition in a horizontal turbulent duct flow,” *Chem. Eng. Res. Des.*, vol. 86, no. 1, pp. 95–106, Jan. 2008.

[104] W. S. Clough, “Transport of particles to surfaces,” *J. Aerosol Sci.*, vol. 4, no. 3, pp. 227–234, May 1973.

[105] K. Bunzl, W. Schimmack, K. Kreutzer, and R. Schierl, “Interception and retention of chernobyl-derived 134Cs, 137Cs and 106Ru in a spruce stand,” *Sci. Total Environ.*, vol. 78, pp. 77–87, Jan. 1989.

[106] E. J. White and F. Turner, “A Method of Estimating Income of Nutrients in a Catch of Airborne Particles by a Woodland Canopy,” *J. Appl. Ecol.*, vol. 7, no. 3, p. 441, Dec. 1970.

[107] K. Peters and R. Eiden, “Modelling the dry deposition velocity of aerosol particles to a spruce forest,” *Atmos. Environ. Part A. Gen. Top.*, vol. 26, no. 14, pp. 2555–2564, Oct. 1992.

[108] Quality of Urban Air Review Group (QUARG), “Third Report to the Department of the Environment. Airborne Particulate Matter in the United Kingdom,” HMSO, London, 1996.

[109] M. W. Gallagher, K. M. Beswick, J. Duyzer, H. Westrate, T. W. Choularton, and P. Hummelshøj, “Measurements of aerosol fluxes to speulder forest using a micrometeorological technique,” *Atmos. Environ.*, vol. 31, no. 3, pp. 359–373, Feb. 1997.

[110] A. C. Chamberlain, “Transport of Lycopodium spores and other small particles to rough surfaces,” *Proc. R. Soc. London. Ser. A. Math. Phys. Sci.*, vol. 296, no. 1444, pp. 45–70, Jan. 1967.

[111] Chamberlain and A.C., “ASPECTS OF TRAVEL AND DEPOSITION OF AEROSOL AND VAPOUR CLOUDS.” 17-Sep-1953.

[112] P. Little and R. D. Wiffen, “Emission and deposition of petrol engine exhaust Pb—I. Deposition of exhaust pb to plant and soil surfaces,” *Atmos. Environ.*, vol. 11, no. 5, pp. 437–447, Jan. 1977.

[113] A. J. Dorgan and E. Loth, “Efficient calculation of the history force at finite Reynolds numbers,” *Int. J. Multiph. Flow*, vol. 33, no. 8, pp. 833–848, Aug. 2007.

[114] H. A. Elghannay and D. K. Tafti, “Development and validation of a reduced order history force model,” *Int. J. Multiph. Flow*, vol. 85, pp. 284–297, Oct. 2016.

APPENDIX A: W/H = 2 CANYON

For the street canyon of W/H = 2, fewer studies were performed regardless of readily available data (see Table 1 and Table 2). Out of the five studies conducted between 2009-2017, RANS was employed in four studies [42]–[45].

A.1 Geometry and Boundary Conditions

The computational domain used is similar that used in the W/H = 1 study, with the domain length extends longer ($x \times y \times z = 42H \times 8H \times H/190$). The cell distribution inside the canyon is the same as W/H = 1 except there are twice as many cells in the W/H = 2 canyon as the W/H = 1 canyon. The W/H = 2 grid consists 2,432,000 computational cells.

Boundary conditions for W/H = 2 are almost identical to those used in the W/H = 1 configuration, exception the location of the jets where each pair of point sources 0.73H and 0.85H away from the walls of the building.

A.2 Initialization and Simulation Criterion

For the W/H = 2 canyon, the mean flow quantities are averaged after about three flow-throughs, and the turbulence calculation was started in the next half flow-through and run for approximately one flow-through, since it is more expensive to run simulations for this configuration, i.e. one flow-through could take up to 9,000 CPU hours). Figure 39 plots transient concentration profiles compiled at 3 different locations close to each canyon wall, showing that the period of two flow-throughs is not yet sufficient for time-averaging and turbulent quantity calculations. Information on the number of flow-throughs and simulated time for both canyon ratios is tabulated in Table 16.

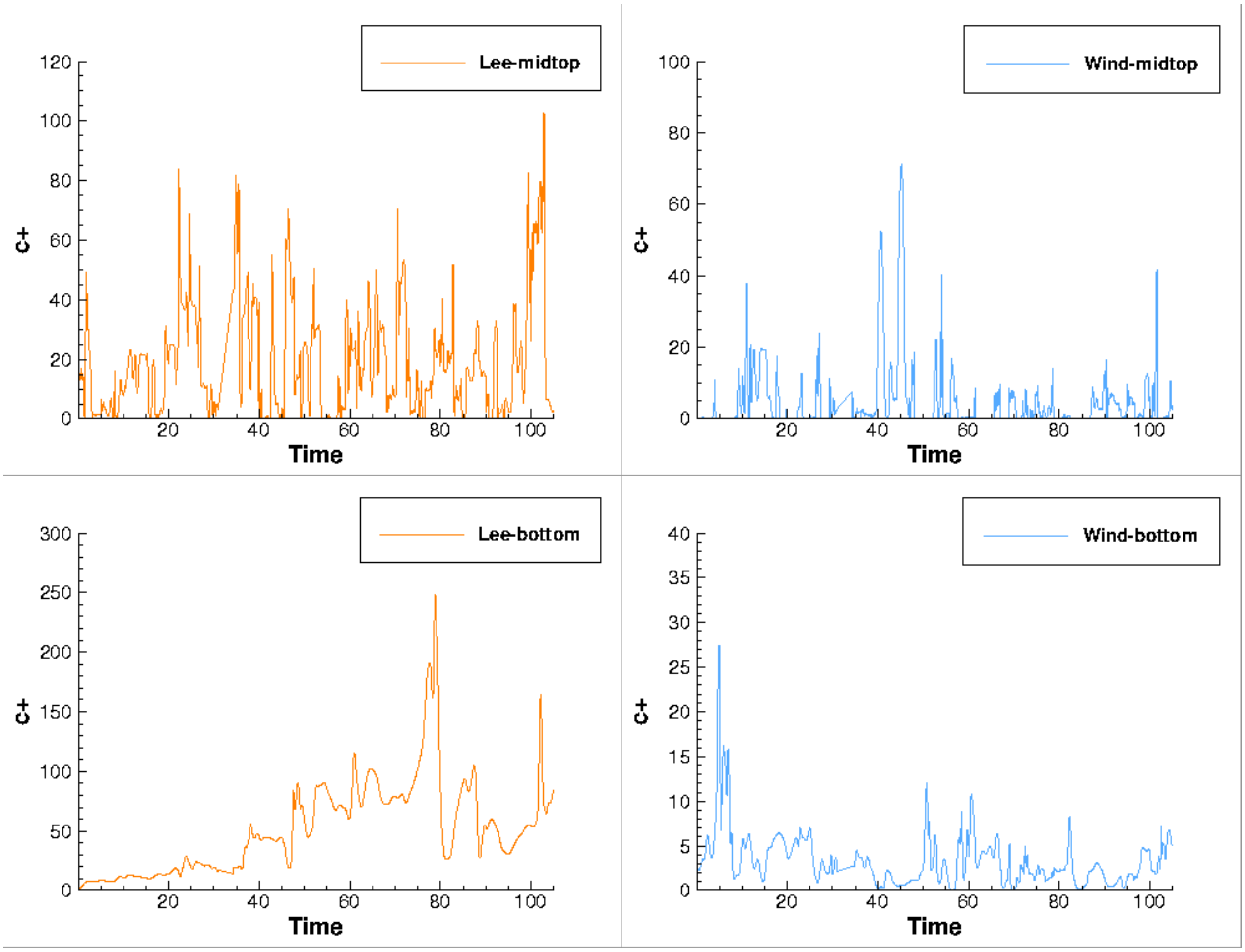

Figure 39 Normalized concentration as a function of non-dimensional time for W/H = 2 canyon (42 non-dimensional time corresponds to one flow-through).

Table 16 Summary of simulation time for W/H = 1 and W/H = 2 canyons.

Canyon	CPU hours for one flow-through	Time	Flow establishment period	Mean flow averaging period	Mean turbulence averaging period
W/H = 1	3,000	Flow-throughs	10.0	5.0	4.0
		Simulated time, s	10.6	5.29	4.23
W/H = 2	11,000	Flow-through	0.5	1	2
		Simulated time, s	0.54	2.17	1.08

A.3 Results and Analysis

The street canyon of W/H = 2 is in the wake interference flow regime. In this regime, the primary vortex extends longer and will eventually break into two co-rotative vortices as the W/H ratio becomes larger than 5, as outlined in Figure 10. Therefore, one primary circulation is expected in this study for the W/H = 2 street canyon also.

A.3.1 Mean flow

Figure 40 shows the contour of the mean streamwise velocity with stream tracers at the Z/H = 0 plane for W/H = 2. The velocities are non-dimensionalized by U^*_{ref}. The typical features of the flow over a canyon in a skimming flow regime is also observed in this geometry. Inside the W/H = 2 canyon, there is one primary clockwise circulation with some counter-clockwise eddies in the bottom corners, as predicted. The corner vortex near the windward wall is larger in the W/H = 2 than in the W/H = 1. The primary vortex of the W/H = 2 canyon also extends wider, with its center located closer to the downstream building. These features are also expected of the flow in the wake interference flow regime at lower W/H ratios.

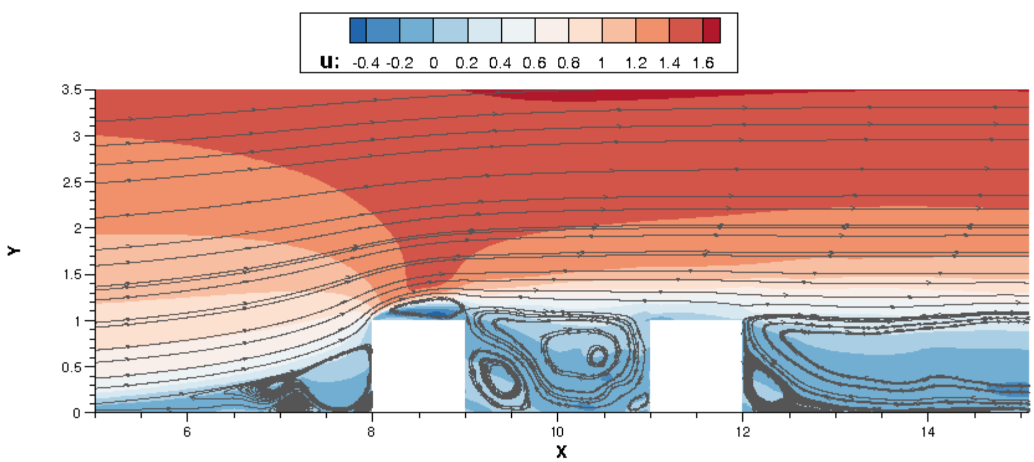

Figure 40 Interpolated values at Z/H = 0 of mean dimensionless streamwise velocity contour with stream tracers of the W/H = 2 canyons (entire domain not shown)

As shown in Figure 41 where u- and v-velocity profiles are plotted at selected y and x locations, the maximum u-velocity inside the W/H = 2 canyon at x/H = 1 is larger, and its peak is closer to the ground than the W/H = 1 canyon. Thus, the W/H = 2 canyon potentially convects the pollution more efficiently. While the v-velocity profiles are similar in shape, the larger downward v-velocity near the leeward wall at y/H = 0.1 also shows that the left corner eddy extends taller and stronger than the one in the W/H = 1 canyon.

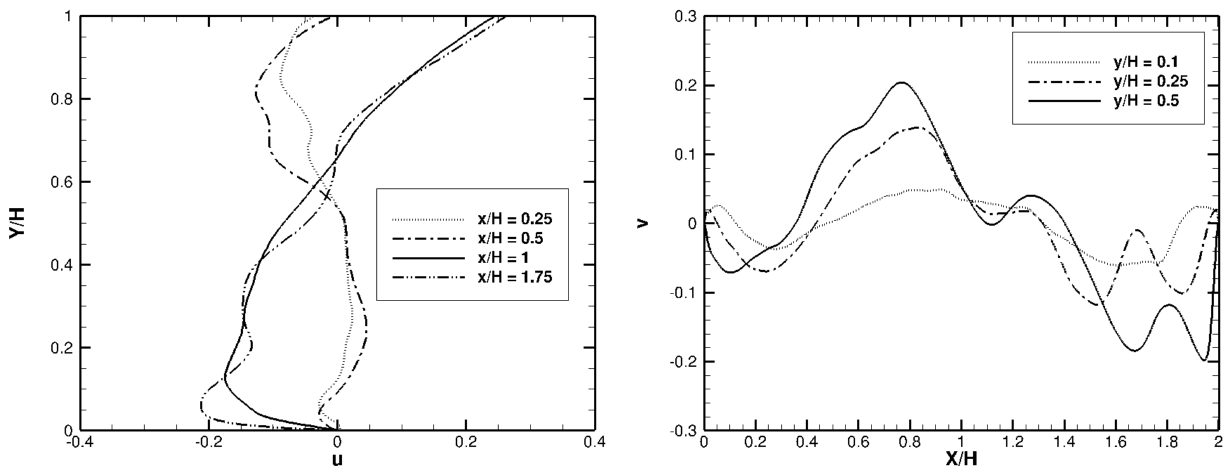

Figure 41 u- and v-velocity profile inside the W/H = 2 canyons. u(y) is plotted at different x-locations, and v(x) is plotted at different y-locations.

These primary and corner vortices play significant roles in dispersing the pollution inside the canyon. As illustrated in Figure 42, the primary circulation carries the pollution clockwise towards the leeward wall. The counter-rotating corner eddy near the leeward side can either act as a pollutant trap if the pollutant gets entrained in the weak recirculation of the corner eddy, or on the other hand, a sufficiently strong corner eddy together with the primary eddy can facilitate the transport of pollutant upward and out of the canyon. Comparing the u-velocity distribution at x/H = 0.1 in Figure 13 and Figure 42, between W/H = 1 and W/H = 2, it is clear that the footprint of the corner eddy is much more favorable for pollutant dispersion when W/H = 2. This effect can be seen in Figure 42, where the concentration of pollutant is much smaller in the W/H = 2 canyon.

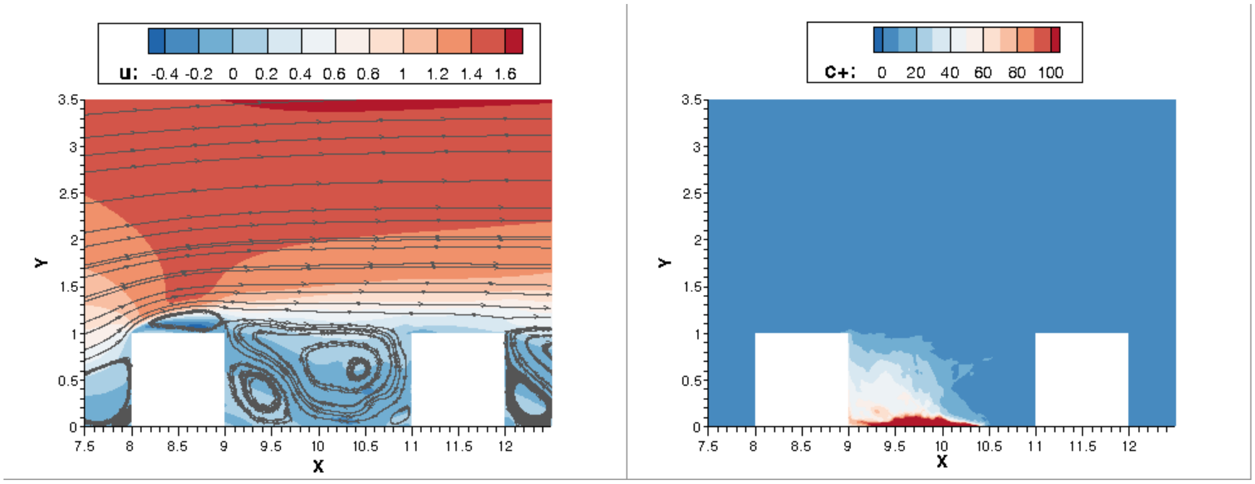

Figure 42 Contour at Z/H = 0 of (left) mean non-dimensional streamwise velocity with 3D velocity stream tracers; and (right) mean c^+ for the street canyon ratios of W/H = 2.

Similar to the W/H = 1 canyon, maximum Reynolds shear stress is observed near the tailing edge and the leading edge of the upstream and downstream buildings, respectively (see Figure 43). Inside the canyon, the turbulence Reynolds shear stress is highest in the lower right corner, where the main circulation region.

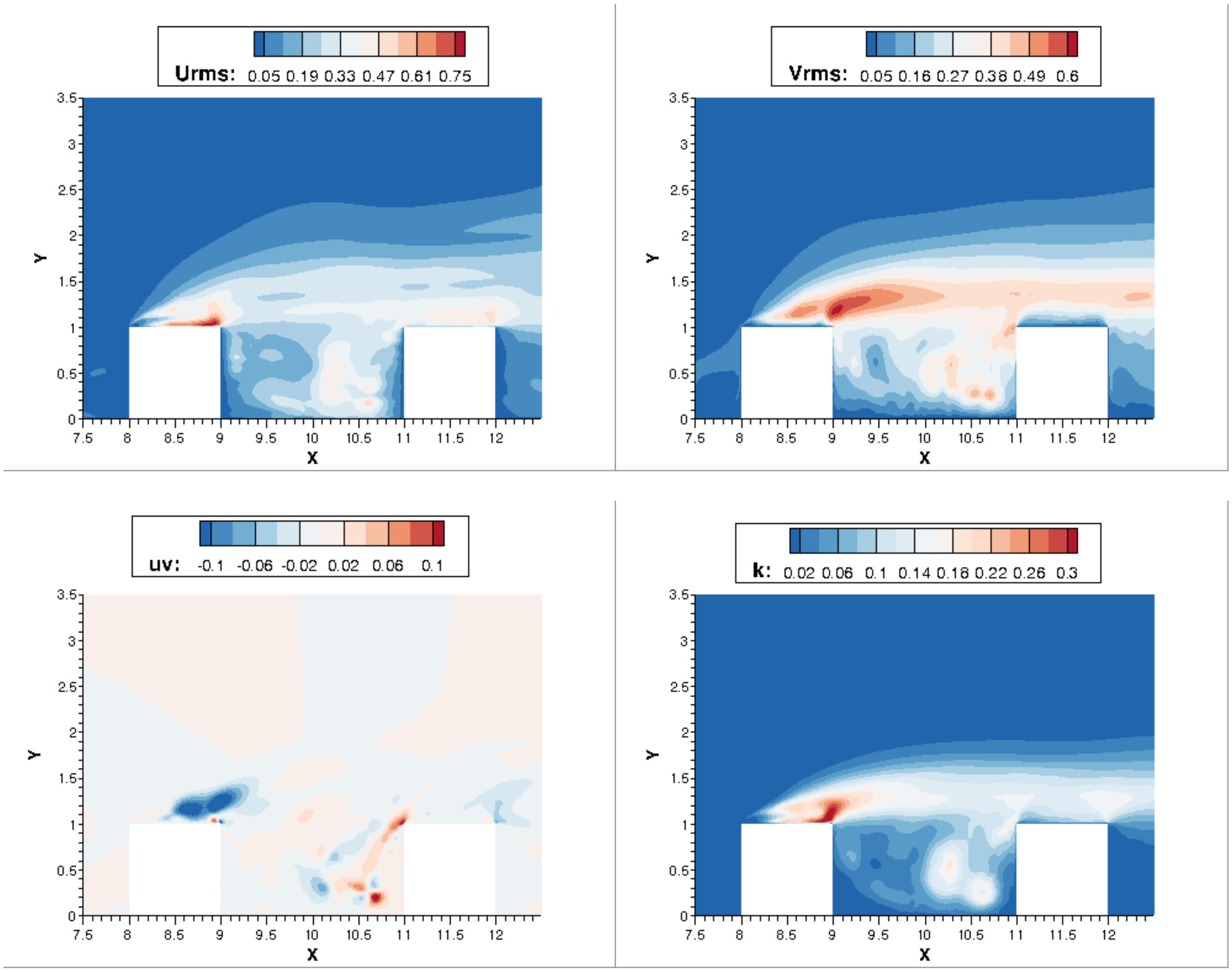

Figure 43 Contour of mean U_{rms}, V_{rms}, mean $U'V'$ and turbulent kinetic energy k inside the W/H = 2 canyon.

A.3.2 Pollution Concentration

The SF_6 concentration profiles at Z/H = 0 are normalized according to the procedure discussed in Section 3.5. The contour taken at the mid-span plane (Z/H = 0) is shown previously in Figure 43.

Figure 44 shows mean concentration profiles near the windward and leeward sides of the canyon, and the horizontal bars show the root-mean-squared fluctuations in concentration.

Overall, there is a relatively good agreement between the simulations and measurements on the leeward side. There is an overall underprediction near the windward wall.

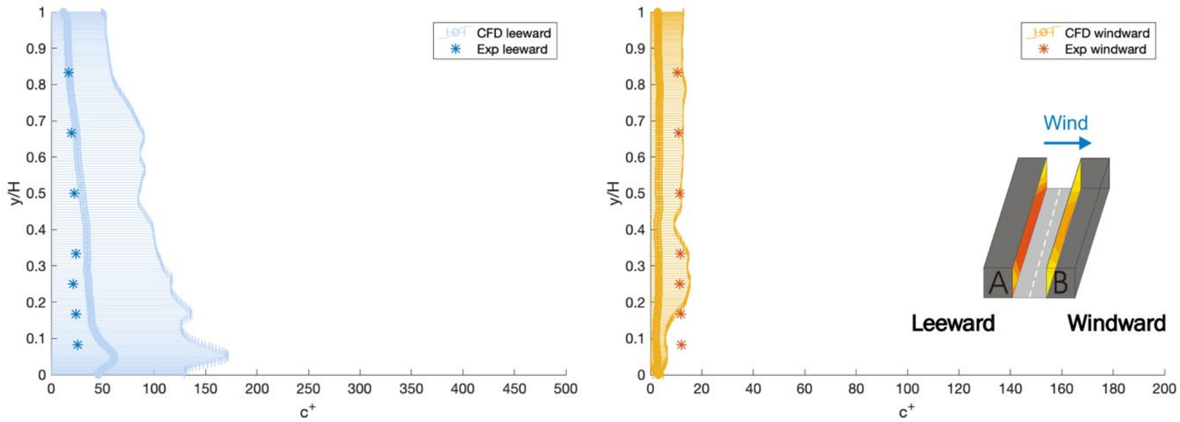

Figure 44 Profiles of computed normalized mass concentration of SF_6, c^+ at Z/H = 0 and X/H = 0.042 away from (right) the windward wall and (left) the leeward wall in comparison to the experimental data from CODASC in W/H = 2 canyon [17]. Horizontal lines indicate root-mean-squared concentration fluctuations in the plot and the inset.

In terms of pollution fluctuation, the concentration in the near ground region could rise as high as 4 times the mean values on the windward side and 2 times as high on the leeward side. This fluctuation is less than that observed in the W/H = 1 canyon.

Nevertheless, the height at which the fluctuation reaches the maximum is at y = 0.06 and 0.26 on the leeward and the windward sides, respectively. Note that the peak on the windward wall is above the average height of an American adult population (y < 0.1) [57]. This implies that the wider canyon could be better for pedestrian's health than the W/H = 1 canyon. The shift in fluctuation peak could be a result of the larger u-velocity and larger primary circulation which allows pollution to be carried out of the canyon more effectively.

A.3.3 Model Performance

Overall, there is a closer agreement between the predictions and measurements in the W/H = 2 canyon on the leeward wall, with all of the simulated concentration within a factor of 2 of the measurement (Table 17). The geometric mean bias and variance indicated by MG and VG are also off the recommended range on the windward wall, and the pairwise coefficients also show a low linear correlation between the predicted and observed concentration profiles (R = -0.68). Similar to the W/H = 1 canyon, the statistical measures show that the windward prediction performs worse than the leeward side.

Table 17 Statistic measures for model performance evaluation

W/H	Wall	FAC2	FB	RNMSE	MG	VG	R
2	Windward	0.00	1.16	1.43	3.78	6.07	-0.68
2	Leeward	1.00	-0.41	0.50	0.69	1.20	0.79
Recommended by Hanna & Chang [59]		≳ 0.30	[-0.67, 0.67]	≲ 2.4	[0.7,1.3]	≲ 4	≳ 0.8
Aim		1	0	0	1	1	1

A.3.3 Conclusion

Similar to the W/H = 1 canyon, the solver performs better in prediction the pollution concentration near the leeward wall. The model may yield better predictions if the period for flow stabilization and averaging was longer.

APPENDIX B: PARTICLE FORCES

The forces acting on a particle (per unit mass) included in Eqn. (24) are defined in this Appendix. The relative magnitude of these forces was evaluated, and only drag and Brownian forces were found to be important in Section 4.3.2.

B.1 Lift Force

Lift force arises from the gradient in the velocity field and is calculated using:

$$\left(\vec{f}_{lift}\right)_i = C_L \vec{w}_j S_{ij} \tag{56}$$

, where $\vec{w} = \vec{u}_f - \vec{u}_p$, C_L is the lift coefficient and S_{ij} are the strain rates. The lift coefficient is defined as:

$$C_L = \frac{5.2}{\sqrt{Re}} \frac{\rho_f^*}{\rho_p^*} \frac{1}{D_p} \frac{1}{(S_{kl}S_{kl})^{1/4}} \tag{57}$$

, where $(S_{kl}S_{kl})^{1/2}$ is the magnitude of the strain rates. The strain rate is defined as

$$S_{ij} = \frac{1}{2}\left(\frac{\partial u_{f_i}}{\partial x_j} + \frac{\partial u_{f_j}}{\partial x_i}\right) \tag{58}$$

Since calculating strain rates at all particle location is very computational expensive, the cell centered values are used instead.

B.2 Buoyancy Force

In the case of steady flow (negligible continuous-phase acceleration), fluid stress is reduced to the buoyancy force, $\vec{f}_{buoy}$, which is essentially the hydro-static pressure gradient integrated over the particle volume acting in the direction opposite to gravity. The term includes the weight of the particle acting in the direction of gravity:

$$\vec{f}_{buoy} = \frac{1}{Fr}\left(1 - \frac{\rho_f^*}{\rho_p^*}\right) = \vec{g}\left(1 - \frac{\rho_f^*}{\rho_p^*}\right) \tag{59}$$

, where Fr is the Froude number (or the inverse of non-dimensionalized gravity) defined by:

$$Fr = \frac{1}{\vec{g}} = \frac{(U_{ref}^*)^2}{\vec{g}^* L_{ref}^*} \tag{60}$$

For a heavy particle ($\rho_f^*/\rho_p^* \rightarrow 0$), the buoyancy force is typically weak comparing to the gravity.

B.3 Added-mass Force

This force arises when the particle acceleration is different from that of the continuous-phase field ($d\vec{w}/dt \neq 0$) and related to the displaced fluid mass as follows

$$\vec{f}_{add} = \frac{1}{2}\frac{\rho_f^*}{\rho_p^*}\frac{d\vec{w}}{dt} \tag{61}$$

B.4 History Force (Basset Force)

The history force is the temporally unsteady portion of the drag force. For creeping flows, the history force can be calculated as done by Basset as follows:

$$\vec{f}_{hist} = -\frac{18\pi\nu_f\rho_f}{D_p^2\rho_p}\left[\int_0^t K(t-\tau)\frac{d\vec{w}}{d\tau}d\tau\right] \tag{62}$$

, where K is the flow integration kernel which is formulated by Basset as

$$K_{Basset}(t-\tau) = \left[\frac{4\pi(t-\tau)}{\tau_d}\right]^{1/2} \tag{63}$$

, where τ_d is the diffusive time scale [113] of the particle defined by

$$\tau_d = \frac{D_p^2}{\nu_f} \tag{64}$$

GENIDLEST approximates History force as proposed by Elghannay and Tafti [114] which is valid for dilute mixture:

$$\vec{f}_{hist} \approx g(n) C_B \frac{\vec{w}}{\sqrt{\tau_D}} \tag{65}$$

, where C_B is defined as

$$C_B = \frac{-18\rho_f}{\rho_p\sqrt{4\pi\tau_d}} \tag{66}$$

, and g(n) is the decay function for $10{,}000 < n < \infty$ time steps which can be represented by

$$g(n) \approx g_1(n) = 2n^{-0.5} \tag{67}$$

B.5 Pressure Force

Pressure force is the force acting on a particle due to spatial gradients in pressure and viscous stresses.

$$\vec{f}_{press} = \frac{\rho_f^*}{\rho_p^*}\frac{d\vec{u}_f}{dt} \tag{68}$$

APPENDIX C: LEAF HAIR CONFIGURATIONS

Table 18 Summary of computational domain used for different cases

<table>
<tr><th></th><th>Name / Units</th><th>LH_d5_hd20_den5</th><th>LH_d5_hd20_den15</th><th>LH_d5_hd30_den15</th><th>LH_d20_hd20_den5</th><th>LH_d20_hd20_den15</th><th>LH_d20_hd30_den5</th><th>LH_d20_hd30_den15</th></tr>
<tr><td>Trichome diameter, D^*_{hair}</td><td>μm</td><td colspan="3">5</td><td colspan="4">20</td></tr>
<tr><td>Trichome height, H^*_{hair}</td><td>μm</td><td colspan="2">100</td><td>150</td><td colspan="2">400</td><td colspan="2">600</td></tr>
<tr><td>Height to diameter ratio; Dimensionless height ($H_{hair} = H^*_{hair}/D^*_{hair}$)</td><td>-</td><td colspan="2">20</td><td>30</td><td colspan="2">20</td><td colspan="2">30</td></tr>
<tr><td>Trichome density</td><td>#/mm^2</td><td>5</td><td>15</td><td>15</td><td>5</td><td>15</td><td>5</td><td>15</td></tr>
<tr><td>Spacing (S^*_{hair})</td><td>μm</td><td>447</td><td>258</td><td>258</td><td>447</td><td>258</td><td>447</td><td>258</td></tr>
<tr><td>Spacing to height ratio (S^*_{hair}/D^*_{hair})</td><td>-</td><td>89.44</td><td>51.64</td><td>51.64</td><td>22.36</td><td>12.91</td><td>22.36</td><td>12.91</td></tr>
<tr><td>Domain height ($3H_{hair}$)</td><td>-</td><td>60</td><td>60</td><td>90</td><td>60</td><td>60</td><td>90</td><td>90</td></tr>
<tr><td>Domain width ($2S^*_{hair}/D^*_{hair}$)</td><td>-</td><td>178.89</td><td>103.28</td><td>103.28</td><td>44.72</td><td>25.82</td><td>44.72</td><td>25.82</td></tr>
<tr><td>Frontal Area (y-z plane)</td><td>-</td><td>10733.13</td><td>6196.77</td><td>9295.16</td><td>2683.28</td><td>1549.19</td><td>4024.92</td><td>2323.79</td></tr>
<tr><td>Domain Volume</td><td>-</td><td>1,920,000</td><td>640,000</td><td>960,000</td><td>120,000</td><td>40,000</td><td>180,000</td><td>60,000</td></tr>
<tr><td>Particle density</td><td>#/mm^3</td><td>10,667</td><td>10,925</td><td>10,667</td><td>10,600</td><td>10,613</td><td>10,675</td><td>10,633</td></tr>
<tr><td>Cell numbers</td><td>-</td><td colspan="3">747,000</td><td colspan="4">607,104</td></tr>
<tr><td>Minimum resolution</td><td>$\Delta x, \Delta y, \Delta z$</td><td colspan="3">0.05, 0.05, 0.1</td><td colspan="4">0.05, 0.05, 0.15</td></tr>
<tr><td>Maximum resolution</td><td>$\Delta x, \Delta y, \Delta z$</td><td colspan="3">5, 5, 3.75</td><td colspan="4">2, 1.25, 3.75</td></tr>
</table>